

Faculty of Science
University of Copenhagen



Towards Continuous Cavity- Enhanced Spectroscopy on Cold Atoms

Mathias Bouchacourt



Towards Continuous Cavity-Enhanced Spectroscopy on Cold Atoms

M.Sc Thesis

Author:
Mathias Bouchacourt



KØBENHAVNS
UNIVERSITET

Supervisors:
Jan Westenkær Thomsen
Stefan Alaric Schäffer

Quantum Optics and Ultracold Atoms Group
Niels Bohr Institute, Copenhagen University
Denmark
06/08/2018

Acknowledgments

I would like to thank Jan Westenkær Thomsen for accepting me into the group, for his expertise and passion which has helped create an environment favorable to a healthy scientific development and learning process. I would also like to thank the Ph.D students present in the group before my arrival;

Stefan Alaric Schäffer, Martin Romme Henriksen and Asbjørn Arvad Jørgensen for their patience and understanding of my slow development and for their passion and lust for knowledge which has greatly improved my understanding of physics and scientific research in general. A special thanks to

Axel Boisen for his time, support and positive attitude towards me. His expertise and work on a large part of the electronics constructed during this project is not to be overlooked. Finally, I would like to thank the different members contemporary to me in the Ultra Cold Atoms group for creating a viable and stimulating working environment.

Abstract

The great precision and accuracy of narrow spectral linewidth lasers are important as precision measurement tools and atomic clocks in many fields of science and technology such as gravitational interferometry, world wide digital data networks and the GPS to name a few [1]. Current state-of-the art clock lasers are pre-stabilized to an empty cavity, ultimately setting a lower limit on the achievable clock precision due to Brownian noise in the cavity mirrors. [5]

This thesis presents progress towards the realization of a narrow linewidth laser through direct cavity-enhanced spectroscopy on an ultra-narrow optical transition on cold atoms based on the work of the authors of [37]. This scheme relaxes some of the requirement on the pre-stabilization cavity. A beamline capable of realizing such narrow linewidth laser was build by the author of [26]. When finalized, the clock laser should reach fractional frequency instabilities of the order of current state-of-the-art clocks.

In this work, The experimental realization of the cooling light generators and the implementation of the temperature stabilization of their mounts is presented. Furthermore, a Monte Carlo simulation was developed in order to give insights into the application of the optical molasses on the atomic beam in the current beamline. A comparison of the efficiency of the microchannel array present in the current setup with the exhaust hole of the previous setup is also presented.

Contents

1	Introduction	1
1.1	The atomic clock	2
1.2	Cavity-Enhanced Spectroscopy on Cold Atoms	4
1.3	Thesis Outline	5
2	Light-Matter Interactions	6
2.1	Atomic Strontium	6
2.2	Light Generation	8
2.2.1	ECDL	8
2.2.2	The Fabry-Perot Cavity	9
2.3	Laser Cooling	11
2.3.1	Optical Molasses	12
2.4	Zeeman Cooling	14
3	Experimental Development	15
3.1	Strontium oven	15
3.2	Cooling Light Generation	18
3.2.1	Diode Characterization	18
3.2.2	ECDL	22
3.2.3	Injection	23
3.2.4	Experimental Setup	25
3.3	Temperature Stabilization	27
3.3.1	Optimal Stabilization Temperature	28
3.3.2	Sensing	29
3.3.3	Control	31
3.3.4	Actuating	35
3.3.5	Performance	36
4	Cold Strontium Beam	40
4.1	Oven and effusion	41
4.1.1	Cosine Law Sampling	42
4.1.2	Results	43
4.2	Simulated Optical Molasses	47
4.3	Oven Efficiency Comparison	53
5	Conclusion	57
A	Temperature Controller Circuitry	58

B	Arduino	65
B.1	Arduino Layout	65
B.2	Arduino Communication	66
B.3	Arduino Script	68
C	Technical Drawings	76
	Bibliography	79

List of Figures

1.1	Illustration of the meaning of precision and accuracy.	2
1.2	Basic Local Oscillator Scheme.	3
1.3	Illustration of the beamline.	4
2.1	Energy levels of ^{88}Sr	7
2.2	Qualitative sketch of the relevant frequency discriminators in the ECDL.	9
2.3	Schematic of a Fabry-Perot cavity.	10
2.4	Sketch of the force on an atom with velocity v due to optical molasses.	13
3.1	Spectral profile of atoms initially effusing from an oven at 480°C fitted to a Voigt profile.	17
3.2	Gaussian HWHM as function of oven temperature as obtained from fitting to a Voigt profile.	18
3.3	Laser diode output power as a function of input current.	19
3.4	Laser diode output spectra for currents above and below threshold current.	19
3.5	Laser diode spectrum for different input currents at $T = 40^\circ\text{C}$	20
3.6	Laser diode Spectrum at different temperatures for a fixed input current above threshold.	20
3.7	Laser diode threshold current as function of temperature.	21
3.8	Maximum laser diode input current as function of laser diode temperature and thermistor resistance.	22
3.9	Schematic drawing of the ECDL mount.	22
3.10	Maximum laser diode input current with external cavity and frequency filter as function of temperature and thermistor resistance as read by the THORLABS controller.	23
3.11	Lasing wavelength of the injected ECDL.	24
3.12	Schematic of a feedback loop with a reference oven.	25
3.13	Schematic of experimental setup.	26
3.14	Simplified block diagram of mount temperature controller mechanism.	27
3.15	ECDL and Slave mount maximum heating and cooling rates.	28
3.16	Schematic of the sensing part of the mount temperature controller.	29
3.17	Wheatstone bridge circuit.	30
3.18	ECDL and Slave Wheatstone bridge output voltage as function of thermistor resistance and temperature.	30
3.19	Schematic block diagram illustrating the signal flow through the different elements of a simplified feedback system.	31
3.20	Schematic block diagram of the control part of the temperature controller.	33
3.21	Step response of the ECDL and Slave laser systems.	33
3.22	ECDL mount temperature for different gains.	35
3.23	Schematic block diagram of the different elements composing the actuator part of the temperature controller.	35

3.24	Simultaneous control of the ECDL and Slave laser mount temperature.	36
3.25	Slave laser mount temperature on external voltage supply.	37
3.26	Comparison of the temperature of the stabilized and non-stabilized ECDL mount.	37
3.27	Power spectral density of the measured stabilized ECDL mount temperature.	38
4.1	Schematic of 3 parts of the beamline through which the atomic propagation is simulated.	40
4.2	3D Maxwell-Boltzmann speed distribution of ^{88}Sr at $T = 530^\circ\text{C}$ (803 K).	41
4.3	Atomic velocity distributions at the input and output of the microchannel array.	44
4.4	Theoretical and simulated angular distribution of the atoms effusing from a microchannel of the relevant dimensions.	46
4.5	Simulated and theoretical transmission probabilities for cylindrical tubes of different length to diameter ratios.	46
4.6	Schematic of the geometry of the optical molasses zone and the microchannel array.	47
4.7	Transmission probability of the optical molasses zone for laser beams with uniform intensity profile as function of the power and detuning.	48
4.8	Transverse velocity distribution of the atomic beam at the selection-tube entrance with and without optical molasses.	49
4.9	Transmission probability of the optical molasses zone of an atomic beam subjected to Gaussian and elliptic laser beam intensity profiles.	51
4.10	Comparison of the transverse velocity distribution of the atomic beam at the selection-tube entrance when subjected to different optical molasses laser beam intensity profiles.	52
4.11	Effect of the use of an exhaust hole and a microchannel array on the transverse velocity profile of an atomic beam.	54
4.12	Atomic v_z velocity distribution of slow atoms effusing out of the microchannel array and exhaust hole.	56
A.1	Technical drawing of Wheatstonebridge circuit.	59
A.2	Schematic drawing of Wheatstonebridge circuit.	60
A.3	Technical drawing of the breadboard circuitry.	61
A.4	Voltage supply circuitry on breadboard.	62
A.5	Actuator circuitry on breadboard.	63
A.6	Schematic drawing of the breadboard.	64
B.1	Layout and wiring of the Arduino.	65
C.1	Technical drawing of the ECDL copper block.	77
C.2	Technical drawing of the aluminum box containing the ECDL.	78

List of Tables

2.1	Wavelengths and Linewidths for ^{88}Sr	7
2.2	Selection Rules for electric dipole transitions in the LS-coupling scheme	8
4.1	Optimal parameters for optical molasses beams.	53
B.1	Arduino communication command list.	66

List of Abbreviations

ADC	Analogue to Digital Converter.
AOM	Acousto-Optic Modulator.
CDF	Cumulative distribution function.
ECDL	External Cavity Diode Laser.
EH	Exhaust hole (Oven effusion medium).
FSR	Free Spectral Range.
FWHM	Full Width Half Maximum .
HWHM	Half Width Half Maximum.
IDE	Integrated Development Environment (software).
LDC	Laser Diode Controller.
LED	Light Emitting Diode.
MA	Microchannel array (Oven effusion medium).
MTC	Mount Temperature Controller.
MOT	Magneto-Optical Trap.
OI	Optical Isolator.
PBS	Polarizing Beam Splitter.
PID	Proportional-Integrator-Derivative.
PM	Polarization Maintaining
PWM	Pulse Width Modulation.
QPN	Quantum Projection Noise.
SNR	Signal to Noise Ratio.
TTC	Thermoelectric Temperature Controller.

1 Introduction

The contribution of precise time keeping devices in human development can hardly be overstated. Its applications ranges broadly from global trade, traffic, satellite positioning and worldwide digital data network operations to most sub-fields of science and engineering. More recently, improvements on the precision and accuracy of clocks would provide a gateway to tests of General Relativity, measurements of Gravitational waves, the search for dark matter and future quantum networks amongst many others [11]. Furthermore, numerous physical quantities and constants rely on the accuracy of time measurement. The most prominent of which being *length*. Today, large distances are measured to a very high degree of accuracy by measuring the time interval a pulse of electromagnetic waves takes to travel this distance. In other words, the availability of stable and reliable frequency sources is a prerequisite to the functioning of the world as we know it and has played a big role in many technological advancements.

The field of time keeping is in constant development and advances rapidly as ever more stringent requirements on the accurate knowledge of time and frequency are required. In order to be able to compare different frequency measurements from different fields of science, locations or times, devices producing stable and well known frequencies are necessary. The first accepted frequency standard can be traced back to the early 20th century with the Riefler mechanical pendulum clock oscillating at 1 Hz and drifting about 10 ms per day. These clocks quickly became obsolete when the use for time keeping below the Hz scale became needed. Furthermore, due to the pendulum's low oscillation frequency, long time scales are required to accurately measure its stability. Frequency standards such as quartz oscillators, oscillating between $10^3 - 10^8$ Hz and drifting about 1 ms a day, were then developed and are still widely used today. As science developed, the construction of clocks based on the oscillation frequency of electro-magnetic waves became possible. By keeping a microwave laser on resonance with an atomic transition, frequency standards oscillating between $10^8 - 10^{10}$ Hz were developed. As atomic properties are the same everywhere in the universe, clocks based on a specific atomic transition allow for an ultimate and universal frequency measurement and are today used worldwide as frequency standards. In fact, since 1967, the second has been defined as [2]:

"The second is the duration of 9192631770 periods of the radiation corresponding to the transition between two hyperfine levels of the ground state of the caesium 133 atom." Now a days, the best clocks are based on the oscillation frequency of optical lasers, reaching frequencies of 10^{15} Hz [1].

Now a days, the best clocks are based on the oscillation frequency of optical lasers, reaching frequencies of 10^{15} Hz [1].

1.1 The atomic clock

The performance of any clock can be described by its precision, describing the reproducibility of a measurement and thus the clock stability, and its accuracy, characterizing how far away the clock frequency is from a true value. Figure 1.1 illustrates the meaning of precision and accuracy when regarding frequency measurements around some true value ν_0 .

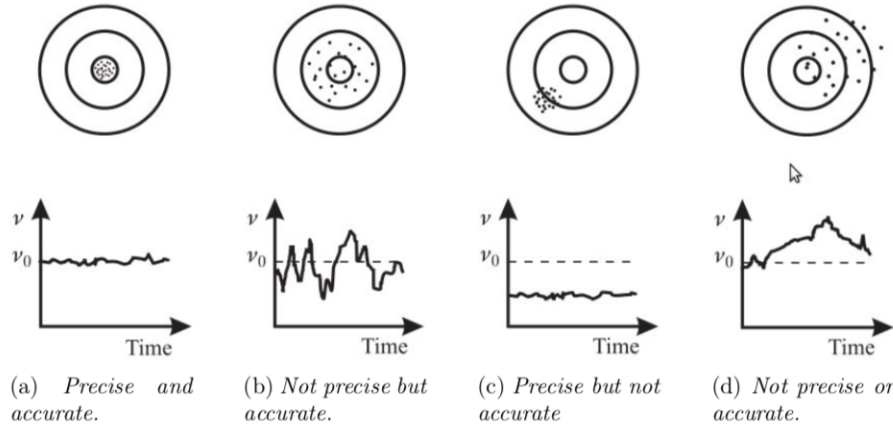


Figure 1.1: Illustration of the meaning of precision and accuracy. a) presents an example of a precise and accurate measurement, showing high reproducibility and values close to some true value ν_0 . Ideally, the measured frequency ν is exactly ν_0 all the time, hitting the center of the shooting mark at all times. b) presents an example of accurate measurements, all close to some true value ν_0 but not very precise or having, in other words, low reproducibility. c) exemplifies a precise measurement, fluctuating little from data point to data point, but having low accuracy, being far from some true value ν_0 . d) exemplifies measurements which are not accurate, meaning far from some true value ν_0 and not precise, thus having low reproducibility. Illustration adapted from [1].

Ideally, a measurement is exactly reproducible, showing no instability, and is perfectly accurate as the measured signal is exactly the desired true value. This means that each frequency measurement are located dead-center on the shooting mark of figure 1.1 at all times. Atomic clocks provide both high precision and accuracies on the frequency of the laser light produced, serving as local oscillator. Standard atomic clocks are composed of two different parts, accounting for the precision and accuracy of the output laser respectively. An illustration of a basic atomic clock scheme is presented in figure 1.2. High precision is achieved through stabilization to an empty high finesse Fabry-Perot cavity, acting as a frequency discriminator for the laser light and assuring low drift in the laser frequency by accounting for the large but predictable drift in cavity length due to aging effects. A servo system ensures that the laser stays on resonance with the cavity. The laser light is subsequently used to interrogate a narrow atomic transition, mimicking its well known resonance frequency, to achieve a high accuracy. In order to take full advantage of the narrow atomic linewidth, the atoms must be extremely well controlled through several cooling and trapping stages to reduce broadening effects. The quantum mechanical nature of atomic transitions provide an unambiguous frequency standard lim-

ited only by the Quantum Projection Noise (QPN), setting a lower limit on the short-term attainable precision of all clocks. A servo system once again ensures that the cavity pre-stabilized laser light stays on resonance with the atomic transition.

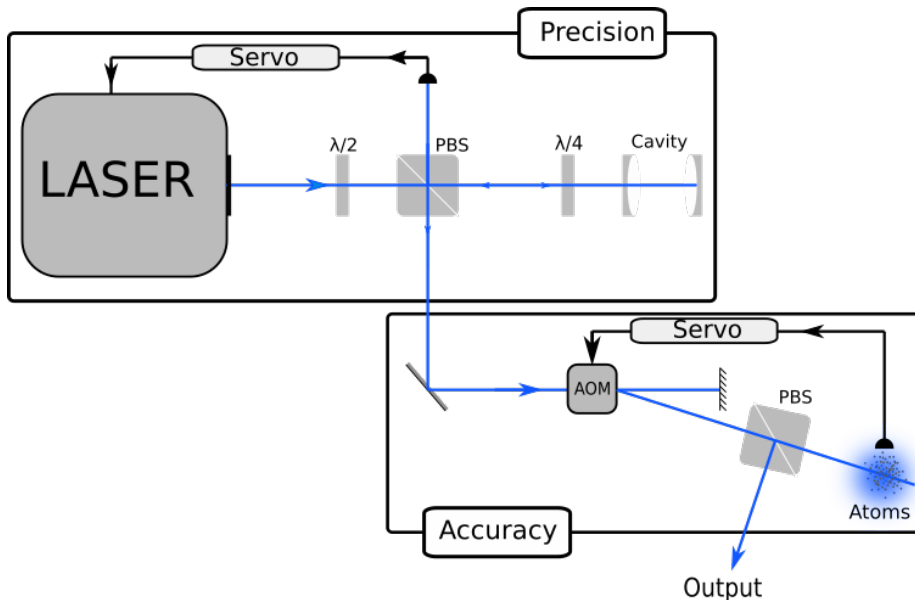


Figure 1.2: Basic local oscillator scheme of an atomic clock. The output of the clock is used as local oscillator, which can in turn yield an extremely precise time measurement by measuring the oscillation frequency of the electric field.

The fractional frequency instability of any QPN-limited oscillator stabilized to a reference with quality factor $Q = \nu/\delta\nu$ can be given by the Allan deviation as, [1]

$$\sigma_y(\tau) \propto \frac{1}{Q} \frac{1}{SNR} \sqrt{\frac{T_c}{\tau}} \quad (1.1)$$

where SNR is the signal to noise ratio and the ratio $\frac{\tau}{T_c}$ is the fraction of the total cycle time T_c where the atoms are interrogated. We have that $SNR \propto \sqrt{N}$, where N is the number of atoms interrogated [6]. Ideally, the Allan deviation is small over some integration time τ , due to large Q factors and signal to noise ratios.

The primary standard set by state-of-the art Cesium based clocks, working on microwave transitions, have reached fractional frequency instabilities of $10^{-14}/\sqrt{\tau}$ [7]. This corresponds to a clock losing one second every $\sim 10^7$ years if averaging over 1s. Current work is focused on utilizing optical transitions with frequencies $\sim 10^{15}$, increasing the Q -factor by approximately five orders of magnitude in comparison with older microwave based clocks.

The fundamental limit to the short-time instability of oscillators in the stabilization scheme presented above is mostly due to Brownian thermo-mechanical

noise in the pre-stabilization cavity mirrors [4]. Many efforts have been conducted to reduce this effect through various techniques and advanced cryogenic and isolating equipment [3, 5].

New stabilization schemes circumventing the limitation caused by Brownian noise in the pre-stabilization cavity mirrors are currently being investigated. One proposed alternative is through cavity-enhanced direct stabilization on an ultra-narrow optical transition [3, 37].

1.2 Cavity-Enhanced Spectroscopy on Cold Atoms

This thesis presents work towards the realization of a clock that utilizes a stabilization scheme based on the work of [37], creating a clock laser through continuous cavity-enhanced spectroscopy on an ultra narrow transition. We hope to achieve both precision and accuracy by directly stabilizing the laser to atoms within an interrogation cavity. This will relax some requirements on the empty pre-stabilization and circumvent the thermal noise floor due to Brownian motion as the atomic linewidth will dominate the system. The interrogation cavity is used to effectively enhance the atomic sample size and create a sensitive error signal for the interrogation cavity servo system.

A beamline capable of realizing continuous cavity-enhanced spectroscopy on an ultra narrow transition was constructed by S.A. Schäffer and a detailed description of the different elements composing it can be found in his thesis [26]. An illustration of the beamline is shown in figure 1.3.

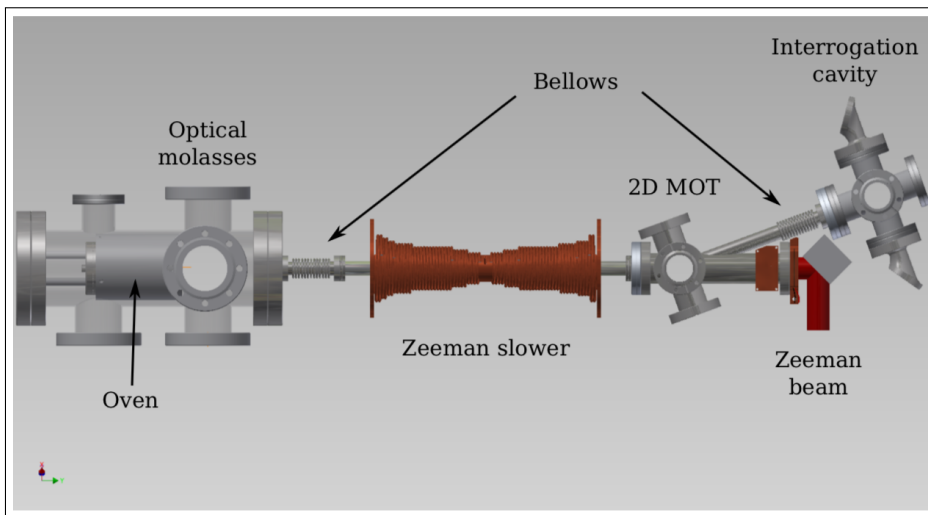


Figure 1.3: Illustration of the beamline. Illustration from [26].

In this experiment, ^{88}Sr atoms are used. Their broad $^1S_0 - ^1P_1$ transition is suitable for laser cooling and their ultra-narrow doubly forbidden $^1S_0 - ^3P_1$ transition is ideal for narrow spectroscopy within the interrogation cavity. The atoms are placed in an oven out of which they will effuse when heated up. Several cooling stages are required in order to increase the amount of atoms and prepare

them for spectroscopy within the interrogation cavity. Right out of the oven, 2D optical molasses are applied in order to collimate the atomic beam. Afterwards, a Zeeman slower is used to cool the atoms in their propagation direction. Finally, a 2D Magneto-Optical Trap (MOT) is used to further collimate and direct the atomic beam onto the interrogation cavity where spectroscopy is performed.

1.3 Thesis Outline

This thesis is an endeavor towards the realization of an error signal through continuous cavity-enhanced spectroscopy on the ultra-narrow intercombination line of cold ^{88}Sr based on the work of M.J Martin, D.Meiser, J.W. Thomsen, Jun Ye and M.J. Holland [37] via the beamline constructed by S.A Schäffer [26].

The thesis is organized as follows. Section 2 presents a characterization of the ^{88}Sr atoms, the External Cavity Diode Laser (ECDL) scheme used as cooling light generator and reviews the theory of laser cooling with special focus on the optical molasses technique.

In the beginning of this project, the oven containing the ^{88}Sr atoms was replaced in order to hopefully increase atomic beam collimation. The new oven contains a microchannel array, a densely packed array of long and thin channels, as opposed to the old oven containing a simple exhaust hole through which the atoms could effuse. Measurements and analysis of the properties of the atoms effusing from the old oven are presented in section 3 for latter comparison with the new oven. As the experiment is only in its initial stage, most experimental work effectuated during this thesis was focused on the generation of the cooling light used throughout the beamline to prepare the atoms for spectroscopy within the interrogation cavity. The experimental work on the cooling light generators, their mount temperature stabilization, and experimental setup are presented in section 3.

Finally, in section 4, a Monte-Carlo simulation was developed in order to offer insights into the optimal application of the 2D optical molasses right after the newly replaced oven. Here, the efficiency of the old oven is also compared with the new oven.

2 *Light-Matter Interactions*

An understanding of the light-matter interactions is essential to the study presented here as they provide a framework for all operations we wish to perform such as manipulating the atomic velocities through laser cooling. In this section, the atomic structure of the strontium atoms and a presentation of the External Cavity Diode Laser (ECDL) scheme used as cooling light generator in this setup are presented. The 2D optical molasses and Zeeman cooling schemes used in the beamline are then presented. Special focus is placed on the optical molasses technique as it is used in the Monte-Carlo simulation presented in section 4.

2.1 Atomic Strontium

The properties of the atom-light interactions are set by the electronic structure of the atom. For the current study, strontium atoms are a prime choice as its electronic structure is convenient for both cooling and probing narrow transitions at optical wavelengths. In this section, a characterization of the relevant energy levels of the strontium atoms and their use in the final experiment is presented.

We choose to use the ^{88}Sr isotope as it has, with 83% abundance, the largest abundance of all the strontium isotopes. ^{88}Sr has two valence electrons which both occupy the 5s shell with spin $S = 0$ in the ground state. When excited, their spins can either be parallel or anti-parallel, resulting in a total spin of either $S = 0$ or $S = 1$. For atoms with weak spin-orbit coupling like ^{88}Sr , the energy levels can be characterized by the Russel-Saunders notation, $^{2S+1}L_J$, allowing us to describe the state of the atom by the orbital angular momenta L and spin momenta S separately [32]. The quantum number $J = L + S$ indicates the atom's total angular momentum. The spin orbit coupling is treated as a perturbation, altering the allowed transition by coupling of the energy levels. The relevant orbital angular momentums $L = 0, 1, 2$ are written with letters as S, P and D , respectively. Figure 2.1 shows the relevant energy levels of ^{88}Sr . The $^1S_0 \leftrightarrow ^1P_1$ transition (1) at $\lambda = 461$ nm has a broad linewidth of $\gamma = 32$ MHz [33] yielding very short decay times of the excited state. This allows for large excitation rates and in turn a more efficient cooling as investigated in section 2.3. The narrow intercombination line $^1S_0 \leftrightarrow ^3P_1$ at $\lambda = 689$ nm is used as probe transition due to its narrow linewidth of $\gamma = 7.5$ kHz [36].

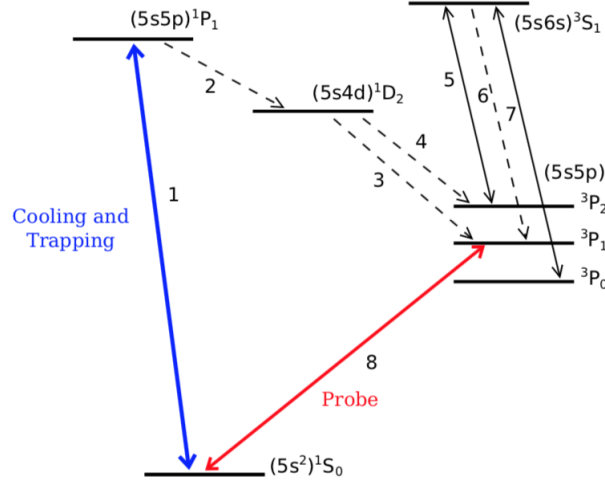


Figure 2.1: Energy levels of ^{88}Sr . Arrows mark the relevant transitions. The linewidths and wavelengths of the relevant transitions are shown in table 2.1. The blue line (1) denotes the cooling transition while the red line (2) denotes the narrow probing transition. Transition 5 and 7 are used for re-pumping whereas dotted lines are simply decay channels. Illustration adapted from [26].

No. —	Wavelength (λ)	Linewidth ($\gamma = \Gamma/2\pi$)
1	460.7nm	32 MHz
2	$6.5\mu\text{m}$	64 Hz
3	$1.8\mu\text{m}$	21 Hz
4	$1.9\mu\text{m}$	11 Hz
5	707.0nm	6.4 MHz
6	688.0nm	4.5 MHz
7	679.1nm	1.4 MHz
8	689.2nm	7.5 kHz

Table 2.1: Wavelength and linewidths for the ^{88}Sr transitions of figure 2.1. [12]

The electric dipole selection rules for LS-coupling are shown in table 2.2. A violation of these rules is only possible in the limit where L and S no longer are good quantum numbers. When the spin-orbit coupling becomes large, the jj -coupling scheme should be used instead. It is clear from the selection rules that the $^1S_0 \leftrightarrow ^3P_0$ and $^1S_0 \leftrightarrow ^3P_2$ are doubly forbidden, infringing rule 1 and 6, while $^1S_0 \leftrightarrow ^3P_1$ only infringes rule 1. The spin-orbit coupling breaks down the spin symmetry, allowing transitions other than $\Delta S = 0$ and rendering the interrogation of transition (8) possible.

The decay from the 1P_1 to the 1D_2 state poses a problem, as atoms in turn can end up in the metastable states 3P_0 and 3P_2 , leading to a loss in cooled and probed atoms. Re-pumping lasers are thus needed on the $^3P_0 \leftrightarrow ^3S_1$ and $^3P_2 \leftrightarrow ^3S_1$ transition to ensure that the atoms always return to the 1S_0 state through 3P_1 when probed.

2.2 Light Generation

1	$\Delta J = 0, \pm 1$	$(J = 0 \not\leftrightarrow J' = 0)$
2	$\Delta M_J = 0, \pm 1$	$(M_J = 0 \not\leftrightarrow M_{J'} = 0 \text{ if } \Delta J = 0)$
3	$(-1)^{l_e} = \pi_p (-1)^{l_g}$	No parity Changes
4	$\Delta l = 0, \pm 1$	
5	$\Delta L = 0, \pm 1$	$(L = 0 \not\leftrightarrow L' = 0)$
6	$\Delta S = 0$	

Table 2.2: Selection Rules for electric dipole transitions in the LS -coupling scheme [24]. Here, e and g refer to the excited and ground states, respectively. Rule 3 puts a restriction on the parity of the absorbed and emitted photon π_p .

2.2 Light Generation

In order to interact with the strontium atoms, it is necessary to have lasers operating at the frequency of the relevant transitions presented in the previous section. Control over the properties of these lasers will allow us to manipulate the atoms in various ways. In our experiment, we use a laser diode placed within an external cavity, thus forming an External Cavity Diode Laser (ECDL), as generator for the cooling light, interrogating the $^1S_0 \leftrightarrow ^1P_1$ transition. Such a design allows for fine tuning of the laser output properties. In the following sections, a description of the ECDL scheme used is presented as well as a description of the electric-field within its external cavity.

2.2.1 ECDL

In order to probe the $^1S_0 \leftrightarrow ^1P_1$ cooling transition of ^{88}Sr , a light generator lasing at the desired wavelength $\lambda = 460$ nm is required. Laser diodes that naturally containing this wavelength within their gain spectrum are commercially available. Laser diodes are composed of a semiconductor with reflecting surfaces, thus forming an internal cavity. They produce light when a current is sent through them by electron-hole recombination. Above some threshold current I_t , stimulated emission of photons dominates inside the laser diode gain medium and lasing occurs. The addition of a cavity to the semiconductor, on top of enhancing the light-matter interactions, imposes some requirements on the resonant modes inside the laser diode cavity given by,

$$\lambda_m = \frac{2Ln}{m} \quad (2.1)$$

where n is the refractive index of the intra-cavity material, λ_m is the vacuum wavelength of the m 'th longitudinal cavity mode and L is the cavity length. The spacing between the allowed modes is given by the Free Spectral Range,

$$FSR = \frac{c}{2nL} \quad (2.2)$$

The spectral width of the cavity resonances $\delta\nu$ is given by,

$$\delta\nu = \frac{FSR}{F} \quad (2.3)$$

where $F \approx \frac{\pi\sqrt{R_1R_2}}{1-R_1R_2}$ is the cavity finesse which depends solely on the intensity reflectance coefficient $R_{1,2}$ of the two cavity mirrors [1]. The intensity reflectance

2.2 Light Generation

coefficient R is defined as the fraction of the incident light being reflected from a surface. The addition of the internal cavity to the semiconductor thus narrows its originally broad gain spectrum.

By adjusting the temperature of the laser diode, the effective length of the laser diode cavity changes through material expansion, allowing some control over the frequency position of the cavity modes. Changes in the diode current result in changes in the gain profile. Due to the poor reflectivity of the laser diode cavity mirror, its spectrum is generally still too broad for efficient atomic interrogation. In order to further reduce the spectral width of the laser, an additional mirror can be placed outside the laser diode, thus forming an External Cavity Diode Laser (ECDL). In the current ECDL configuration, the length and alignment of the external cavity can be fine-tuned through the presence of a piezoelectric element located on the back of the external mirror. A frequency filter is placed inside the ECDL to further discriminate the lasing frequency. Depending on its orientation, the latter suppresses light of a specific wavelength through destructive interference within the filter itself. The filter orientation can thus be optimized to obtain the desired lasing frequency. The external cavity, being longer than the internal laser diode cavity, poses some more stringent requirements on the allowed modes and results in a smaller spacing between the modes as can be inferred from equation 2.1 and 2.2. The lasing spectrum of the ECDL is a result of the convolution of the different frequency discriminators composing it. The different spectra are shown in figure 2.2.

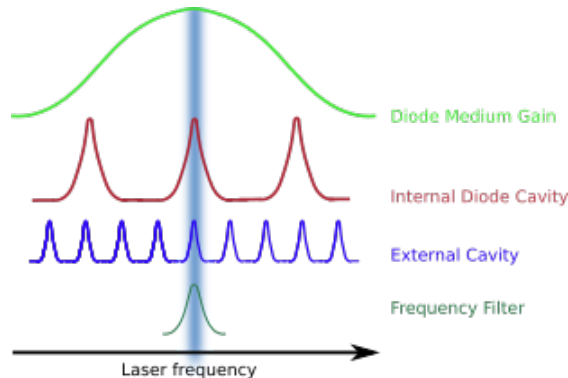


Figure 2.2: Qualitative sketch of the relevant frequency discriminators in the ECDL (not to scale). Large laser diode gain spectrum, internal and external cavity resonances and mode selection via the frequency filter. The ECDL's output lasing signal is given by the overlap of these resonances and gain spectra.

2.2.2 The Fabry-Perot Cavity

We can describe the external cavity of the ECDL as a Fabry-Perot cavity, formed by the back of the diode and the external mirror as illustrated in figure 2.3. In the following description, the cavity mirrors have reflectance r_1, r_2 and are assumed to be flat and parallel. A frequency filter with transmittance t_f was added to our description of the Fabry-Perot ECDL cavity. The electric field emitted by the laser diode is denoted E_0 . Each round trip, the E-field acquires

2.2 Light Generation

a phase shift of $e^{-2in\omega L/c}$ where L is the cavity length, c is the speed of light in vacuum, n is the intra-cavity material and ω is the angular oscillation frequency of the field. Upon reflection on a mirror, the electric field acquires a phase-shift of $e^{-i\pi} = -1$ that can be omitted.

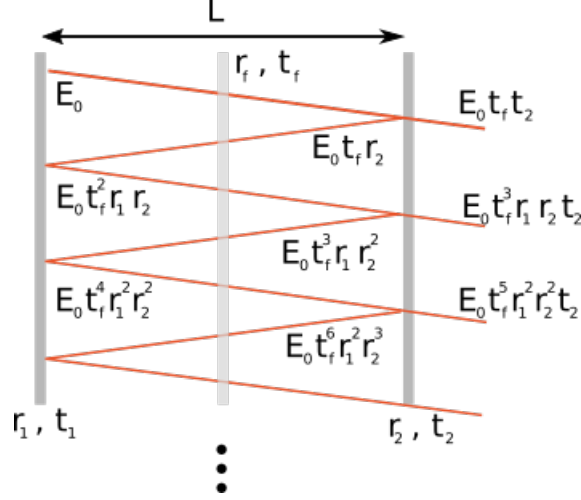


Figure 2.3: Schematic of a Fabry-Perot cavity. Starting from the left side of the cavity, the field propagates and is reflected and transmitted at each interface. The electric field inside the cavity is amplified through the multiple reflections on the external mirrors. A frequency filter with reflectance r_f and transmittance t_f has been added inside the cavity. Here, the phase component of the field have been omitted and only the magnitude of the E -field is represented. In this schematic, the electric field is drawn spatially separated for clarity but are in reality all spatially overlapping as they are plane waves.

The total electric field circulating within the cavity is given by the sum of the electric field components transmitted through the filter and reflected at the mirrors as is illustrated in figure 2.3. After the each interface, the electric field attenuates and the total field inside the cavity can be written as,

$$E_{circ} = E_0 + E_0 t_f^2 r_1 r_2 e^{-2i\phi} + E_0 t_f^4 r_1^2 r_2^2 e^{-4i\phi} + \dots \quad (2.4)$$

where the t_f is the fraction of the electric field transmitted through the filter located within the cavity. Re-writing the above expression as a sum we get,

$$E_{circ} = E_0 \sum_{j=0}^{\infty} (t_f^2 r_1 r_2 e^{-2i\phi})^j \quad (2.5)$$

Recognizing the above expression as a converging power series given by,

$$\sum_{j=0}^{\infty} x^j = \frac{1}{1-x} \quad (2.6)$$

we can re-write the electric field inside the cavity as,

$$E_{circ} = \frac{E_0}{1 - T_f \sqrt{R_1 R_2} e^{-2i\phi}} \quad (2.7)$$

2.3 Laser Cooling

where the intensity transmission and reflection coefficients are related to their electric field analogue through $T_f = t_f^2$, $R_1 = r_1^2$ and $R_2 = r_2^2$. Computing the intensity $I = \frac{cn\epsilon_0}{2}|E|^2$ and inserting into $P = \int I da$ to find the power inside the cavity we have,

$$P = \frac{P_0}{1 - 2T_f\sqrt{R_1R_2}\cos(2\phi) + T_f^2R_1R_2} \quad (2.8)$$

The above expression will be used in section 3.2.2 in order to calculate the maximum power allowed inside the laser diode when placed within an external cavity.

2.3 Laser Cooling

Broadening mechanisms such as Doppler broadening, arising due to the high velocity of the atoms effusing from the oven, prevents us to take full advantage of the narrow probing atomic transition. Furthermore, as the path from start to end of the beamline is long, atomic beam collimation is important in order to propagate as many atoms as possible into each component of the beamline. Control over the atomic velocities and positions is thus necessary. This can be achieved by subjecting the atoms to laser beams in different configurations depending on the control required. We refer to this technique as laser cooling due to the direct relation between the average velocity and temperature of a thermal beam of atoms. The temperature of such thermal beam can be increased or decreased through the emission of absorbed laser photons, hence the term laser cooling. In this section, we review the physics of laser cooling and its use within the beamline. Special focus is placed on the optical molasses cooling technique which is used in the Monte-Carlo simulation presented in section 4.

The physics of laser cooling can be understood as a momentum transfer from photons to atoms. Regarding the atom as a quantum mechanical two level system, there is a certain probability that a photon will be absorbed by the atom, resulting in a momentum change in the latter of $\Delta p = \hbar k$. $p = \hbar k$ corresponds to the momentum carried by the photon where $k = \frac{2\pi}{\lambda}$ is the wavenumber and $\hbar = \frac{h}{2\pi}$ where h is Planck's constant. Upon absorption, the momentum of the photon is transferred to the atom and the latter is excited from its ground state to a state of higher energy. Eventually, the state of the atom will decay back to the ground state by spontaneously emitting a photon in a random direction, causing another momentum change in the direction of emission. However, as the momentum change induced by the emission or absorption of one photon is minuscule in comparison with the momentum of a heavy ^{88}Sr atom, we require a large number of absorption/emission cycles for efficient cooling. Therefore, the large transition decay rate $\gamma = 32$ MHz of the $^1S_0 \leftrightarrow ^1P_1$ cooling transition is vital as it will allow for fast emission rates and thus faster re-absorption. Over many absorption/emission cycles, the total momentum change caused by the photon emission averages to zero due to their random emission direction. If an absorbed photon is emitted through stimulated emission, the net change in atomic momentum is 0 as the stimulated photon has the same properties as the previously absorbed photon. By controlling the absorption direction, thus consistently inducing the momentum kick in the same direction, only the sum of

the total momentum transfer of the absorbed photons will remain. An atomic beam can thus be slowed in its propagation direction by being subjected to a counter-propagating laser beam.

The magnitude of the force with which the atoms scatter photons is given by the rate at which the light field transfers momentum to the atoms as,

$$F_{scatt} = p_{photon} R_{scatt} \quad (2.9)$$

The scattering rate $R_{scatt} = \Gamma \rho_{ee}$, where ρ_{ee} is the steady-state population of the upper energy level [24],

$$\rho_{ee} = \frac{\Omega^2/4}{\delta^2 + \Omega^2/2 + \Gamma^2/4} \quad (2.10)$$

Here, Γ is the linewidth of the transition in angular frequency and δ is the detuning of the angular laser frequency ω from resonance ω_0 . Compared with an atom at rest, the resonance frequency of a moving atom will shift due to the different effective photon wavelength seen by the atom due to its motion. Taking into account this Doppler shift, the detuning is given by $\delta = \omega - \omega_0 + kv$. In equation 2.10 the Rabi frequency Ω can be written as,

$$\Omega^2 = \frac{\Gamma^2 I}{2I_{sat}} \quad (2.11)$$

where I is the light field intensity and I_{sat} is the saturation intensity of the transition given by,

$$I_{sat} = \frac{\pi \hbar c}{3\lambda^3} \Gamma \quad (2.12)$$

where \hbar is Planck's constant, λ is the wavelength of the atomic transition and c is the speed of light in vacuum. Combining equations 2.9, 2.10 and 2.12, the total force on an atom due to laser light of intensity I and wave-vector k is given by [24],

$$F_{scatt} = \hbar k \Gamma \rho_{ee} = \hbar k \frac{\Gamma}{2} \frac{s_0}{1 + s_0 + 4\delta^2/\Gamma^2} \quad (2.13)$$

where $s_0 = \frac{I}{I_{sat}}$. Γ , ω and ω_0 are here expressed in angular frequency. The scattering force exhibits a Lorentzian shape with Half Width at Half Maximum $HWHM \propto \Gamma s_0$ and location parameter proportional to the detuning δ .

2.3.1 Optical Molasses

Cooling of an atomic beam in 1,2 or 3 dimensions is often achieved by a configuration of orthogonal pairs of counter-propagating laser beams through a technique called optical molasses. When subjecting a moving atom to two counter-propagating beams an imbalance in the resulting force from each beam will arise, due to the Doppler shift, causing one beam to exert a larger force on the atom than the other. By detuning the laser light below the atomic resonance frequency, the Doppler shift arising from the atomic motion will effectively increase the frequency of the laser beam propagating in the direction opposite to

2.3 Laser Cooling

the atom's velocity. This brings the light closer to resonance with the atom, increasing the absorption rate from this beam. Restricting ourselves to one dimension, the resulting force from a pair of counter-propagating beams on an atom is given by the sum of the forces from the two individual beams as, [24]

$$F_{Molasses} = F_{scatt}(\omega - \omega_0 - kv) - F_{scatt}(\omega - \omega_0 + kv) \quad (2.14)$$

For low velocities, $kv \ll \Gamma$, $F_{Molasses}$ can be rewritten as a frictional force, or damping, exerted by the light on the atoms. It then takes the form

$$F_{Molasses} = -\alpha v \quad (2.15)$$

with damping coefficient α given by $\alpha = 4\hbar k^2 s_0 \frac{-2\Delta/\Gamma}{[1+(2\Delta/\Gamma)^2]^2}$. Here, $\Delta = \omega - \omega_0$ is the Doppler free detuning, independent of the atomic velocities. As a result, within the low velocity approximation, the force on the atom is a linear function of its velocity v . Damping requires a positive α and thus a red detuned laser $\Delta < 0$. The force from equation 2.15 is zero for $\Delta = 0$ or for stationary atoms with $v = 0$. A sketch of the magnitude of the resulting force $F_{Molasses}$ on an atom with velocity v due to two counter propagating beams is shown in figure 2.4. The blue curves represent the force on the atom arising from each beam separately while the red curve represents the total force on the atom $F_{Molasses}$, the resultant from the two blue curves. For small velocities, the linear behavior of the force is clearly shown.

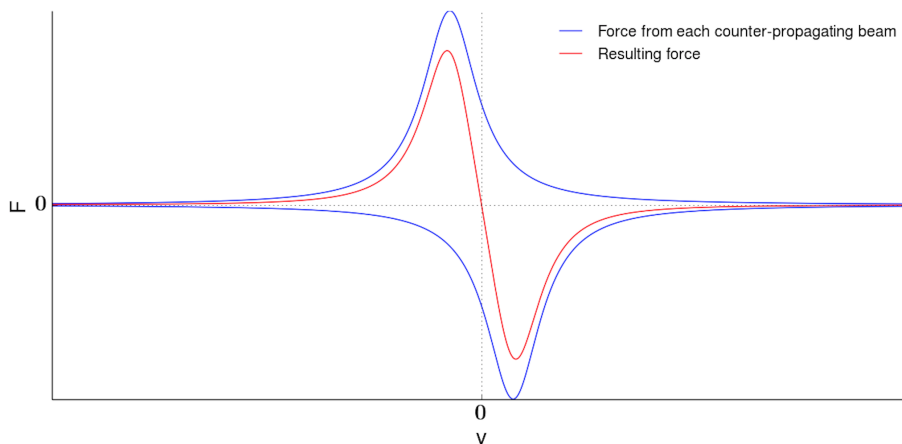


Figure 2.4: Sketch of the resulting force from the optical molasses beams on an atom with velocity v . The blue curves show the force on the atom from each individual laser beam while and the red curve represents the resulting force $F_{Molasses}$ from the two counter-propagating beams.

Within the damping force approximation, the capture range is approximately given by $v_c \sim \pm\Gamma/k$. In our laboratory, the velocity capture range of the atoms effusing from the new oven is $v_c \sim \pm 15$ m/s. In practice, the optimal value of parameters I and Δ will largely depend on the atomic transition interrogated, the atomic velocity distribution and laser beam shape.

2.4 Zeeman Cooling

It is desired to reduce the propagation velocity of the atomic beam in order to increase the light-matter interaction time within the interrogation cavity in the final experiment. This can be done by subjecting the atomic beam to a counter-propagating beam as investigated earlier. However, as the atomic velocities are reduced, the effective laser frequency seen by the atoms decreases and so does the cooling force. The effective transition frequency of the atoms will thus continually shift as their velocity decreases. In order to account for this effect, the Zeeman effect can be used to correct for the shift in effective atomic resonance frequency.

In the presence of a weak magnetic field B , the atomic energy levels E will shift according to,

$$\Delta E = g_j \mu_B B M_j \quad (2.16)$$

where, g_j is the Landé g-factor, M_j is the magnetic quantum number μ_B is the Bohr magneton. In order to keep the atomic resonance frequency ω_a on resonance with the laser frequency ω_l , we must have that the Zeeman shift in the atomic energy levels induced by the magnetic field equals the Doppler shift kv resulting from the atomic deceleration [24],

$$\frac{\mu_B B}{\hbar} = kv \quad (2.17)$$

Assuming constant deceleration of the atomic velocities, we can satisfy equation 2.17 by applying a spatially varying magnetic profile $B(z)$. This cooling method is used in a Zeeman slower in the beamline depicted in figure 1.3 with solenoids through which current flows to produce the magnetic field. Using this technique, atomic velocities can be reduced to

3 *Experimental Development*

This section presents a description of the experimental work performed during this project. In the beginning of this project, the oven containing the strontium atoms was replaced with an oven containing a microchannel array, a densely packed array of thin channels, in hope of increasing the atomic beam collimation. We start this section by performing measurements on the atomic transverse velocities after the Zeeman slower, as the atoms effused from the old oven. This will allow for future comparison with the transverse velocities of the atoms effusing from the new oven. Then, a description of the ECDL and its performance is presented along with the future prospects of its use in the scope of the final experiment. Finally, a description of the mount temperature controller, stabilizing the temperature of the ECDL mount and its performance is presented.

3.1 Strontium oven

The collimation of the atomic beam as it effuses out of the oven plays a big role in the efficiency of the final experiment as it greatly increase the amount of atoms propagating further down the beamline. In the beginning of this project, the oven present in an early version of the experiment, containing an exhaust hole, was replaced with an oven containing a microchannel array, a densely packed array of channels with a large length to diameter ratio, in hope of increasing beam collimation. Due to the smaller dimensions of the microchannels of the new oven in comparison with the exhaust hole of the old oven, the atoms are expected to effuse more collimated. In this section, we present results from transverse velocity measurements of atoms as produced by the old oven, allowing for future comparison with the new oven.

By subjecting an atomic beam to an orthogonal laser beam, we can infer the transverse velocities of the atoms since the atomic absorption spectrum is velocity dependent as investigated in section 2.3. Inferring atomic velocities from the observed emission spectrum requires knowledge of the multiple spectra composing the observed spectrum as we will investigate now.

Absorbed photons are spontaneously emitted with an energy equal to the energy difference between the excited and ground state to which the atom decays to upon emission. However, due to the Heisenberg uncertainty principle $\Delta E \Delta t \approx \hbar$, the atomic energy levels are not perfectly well-defined. An emitted photon therefore has a range of possible frequencies. The spectral profile due to the uncertainty principle is called the natural broadening and has the Lorentzian line-shape given by, [29]

$$D_{Lorentz}(\nu) = \frac{\gamma}{\pi} \frac{1}{(\nu - \nu_0)^2 + \gamma^2} \quad (3.1)$$

3.1 Strontium oven

where ν is the frequency, ν_0 is the center-line frequency and $\gamma = \Gamma/2\pi$ is the Half Width at Half Maximum (HWHM) of the distribution.

When orthogonally subjecting an atomic beam to a pair of counter-propagating laser beams, the frequency of the light perceived by the atoms is velocity dependent as investigated in section 2.3.1. The change in frequency $\Delta\nu = \nu - \nu_0$ between the resonance frequency ν_0 of the interrogated transition and the effective resonance frequency due to atomic motion ν is given by,

$$\Delta\nu = \frac{\Delta v}{c}\nu_0 \quad (3.2)$$

where $\Delta v = v_r - v_s$ is the difference between the velocity of the receiver v_r and the source v_s and c is the speed of light. We can assume $\Delta v = v_r$ as the light source is at rest in the laboratory and $\Delta\nu = \nu$ by setting $\nu_0 = 0$ as we know the exact resonance frequency of the atoms at rest. Restricting ourselves to 1-dimension, as we are only interested in the atomic velocities transverse to the atomic beam propagation, and assuming an ideal gas, the probability of finding an atom with velocity v is given by the 1-dimensional Maxwell-Boltzmann distribution,

$$f(v) = \sqrt{\frac{m}{2\pi k_B T}} e^{-\frac{mv^2}{2k_B T}} \quad (3.3)$$

where k_B is the Boltzmann constant, m is the atomic mass and T is the temperature. Combining equation 3.2 and 3.3, we obtain the Gaussian-shaped broadening of the atomic emission spectrum due to atomic velocities, namely, the Doppler broadening, [29] [24]

$$D_{Doppler}(\nu) = \frac{\nu_0}{c} \frac{1}{\sqrt{\pi}} \frac{\sqrt{\ln 2}}{\alpha_D} e^{-\frac{\nu^2 \ln(2)}{\alpha_D^2}} \quad (3.4)$$

where

$$\alpha_D = \frac{\nu_0}{c} \sqrt{\frac{2K_B T \ln 2}{m}} \quad (3.5)$$

is the Half Width at Half Maximum (HWHM). The linewidth of the Doppler broadening thus depends on the temperature of the atoms, directly related to their velocity. By measuring the linewidth of the Doppler profile, we can infer the atomic transverse velocity as the most probable velocity of the Maxwell-Boltzmann distribution.

We collect the atomic fluorescence after the Zeeman slower at the MOT windows depicted in figure 1.3. The finite interaction time between the laser beam and the atomic beam leads to the so called transit-time broadening due to the Fourier relation between time and energy or frequency. The spread in frequency is related to the atomic beam velocity in the propagation direction and the atomic beam diameter as $\Delta f_{tt} = \frac{v_{beam}}{d}$. For our measurements, transit-time broadening is negligible as the atomic velocities after the Zeeman slower are of an order of magnitude of 10 m/s and the beam diameter of the order of millimeters yielding $\Delta f_{tt} \ll 1$ MHz.

3.1 Strontium oven

The realistic atomic absorption spectrum is given by the convolution of the Lorentzian and Doppler profile, named Voigt profile, and is given by [29]

$$D_V(\nu) \equiv D_{Lorentz} \otimes D_{Doppler} = \frac{\gamma\nu_0 \ln 2}{\alpha_D \pi^{3/2}} \int_{-\infty}^{+\infty} \frac{e^{-\frac{\ln(2)\nu'^2}{\alpha_D^2}}}{(\nu - \nu')^2 + \gamma^2} d\nu' \quad (3.6)$$

The atomic fluorescence was measured at the MOT windows transversely to the atomic propagation direction as the temperature of the old oven was constantly decreased, thus changing the average velocity of the effusing atoms. The interrogation was performed by scanning through a wide range of laser frequencies to be sure to hit the atomic resonance exactly. The laser beam power was $P = 1.5mW$. The atomic fluorescence was collected with an R7400u-20 photomultiplier.

Figure 3.1 shows the Voigt fit of the measured atomic fluorescence for an oven temperature of $480^\circ C$. The highest peak in the data corresponds to the resonance of the abundant ^{88}Sr while the smaller peak appearing in the data corresponds to a nearby resonance of ^{86}Sr , composing 9.86% of the strontium sample present in the oven. From the Voigt profile fit, a Gaussian HWHM of the Doppler broadening can be retrieved and related to a transverse atomic temperature and velocity.

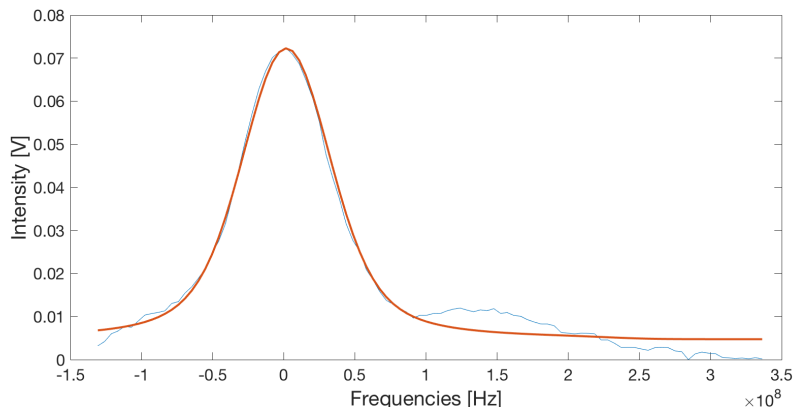


Figure 3.1: Spectral profile of atoms initially effusing from an oven at $480^\circ C$ fitted to a Voigt profile, the convolution of the natural Lorentzian profile and the Doppler broadened profile. The Voigt profile is centered around the resonance frequency of the cooling transition.

Figure 3.2 shows the obtained HWHM of the Doppler broadening as function of oven temperature. As expected, the HWHM increases as function of temperature. Due to the different elements in the beamline preceding the MOT windows where the measurement is performed, the HWHM does not increase proportionally to the square-root of temperature as expected from the Doppler broadening HWHM.

3.2 Cooling Light Generation

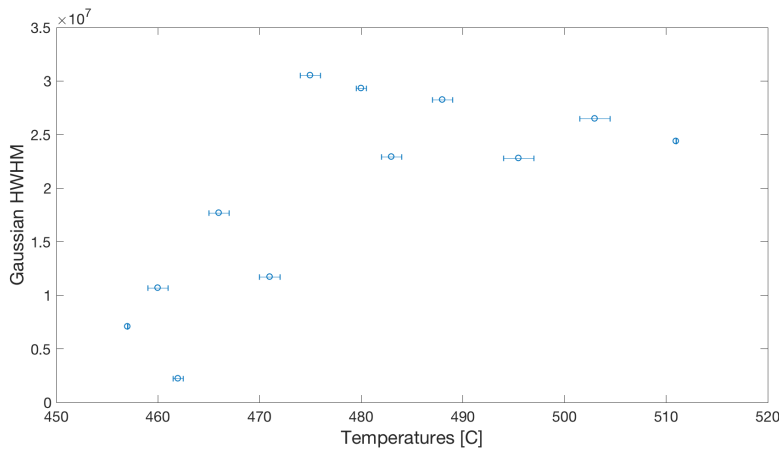


Figure 3.2: Gaussian HWHM as function of oven temperature as obtained from fitting to a Voigt profile.

Using equation 3.5, we find that the atoms have an average transverse temperature of ≈ 1 °K for an oven at 784.4 °K (511 °K). This corresponds to an average transverse velocity of $\tilde{v} \approx 10$ m/s. Hopefully, the microchannel array, present in the new oven, will lead to further collimation of the atomic beam and by extension narrower Doppler linewidths as well as an increased amount of atoms further down the beamline.

3.2 Cooling Light Generation

A stable cooling light generator working at the cooling light frequency is essential to the final experiment as it will be used to cool and collimate atoms throughout the beamline. In this section, the experimental development and considerations in the construction of the ECDL used as cooling light generator are presented. Firstly, we present a characterization of the blue laser diode used within the ECDL. Then we proceed to characterize the whole of the ECDL, considering its efficiency, performance and role in the current and future experimental setup. Finally, we present a description of the controller stabilizing the ECDL mount temperature and its performance.

3.2.1 Diode Characterization

In order to generate the cooling light, a device generating light at the frequency of the cooling transition is required. We use the commercially available Nichia NDB4216 blue diodes as laser diodes within our ECDL. Characterizing the blue laser diodes will give us insights into the parameter values desired for attaining the wanted ECDL single lasing frequency and how to avoid damaging the diode when placed inside the external cavity.

As the diode current is high enough for the optical gain to balance the round trip losses of light of the laser diode cavity, stimulated emission dominates within the gain medium. As a result, from this threshold current I_t and higher, the laser diode output power increases drastically. As shown in figure 3.3, for a laser

3.2 Cooling Light Generation

diode at $T = 40^\circ$, the output power increases linearly with 1.02 W/A when the threshold current of $I_t = 31.7 \text{ mA}$ is exceeded.

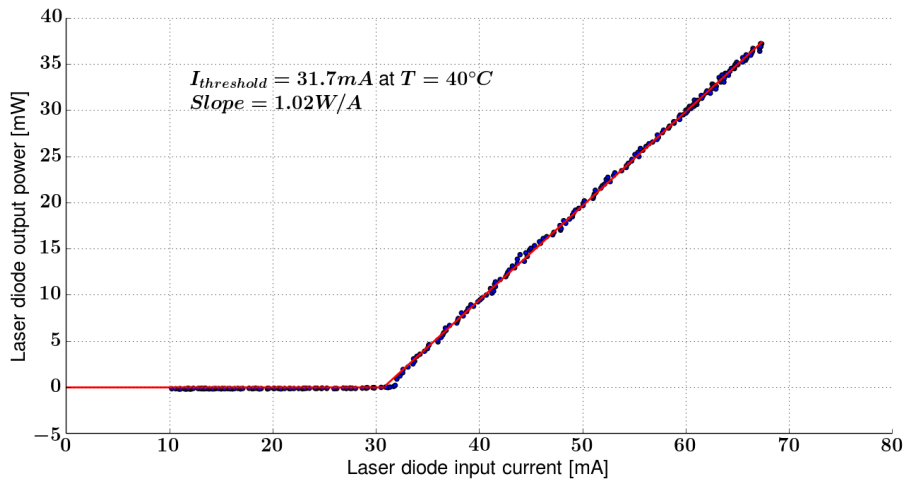


Figure 3.3: Laser diode output power as function of input current. The laser diode output power is close to 0 until the threshold current is exceeded at $I_{\text{threshold}} = 31.7 \text{ mA}$ for a diode at $T = 40^\circ \text{C}$. For input currents higher than $I_{\text{threshold}}$, the output power increases at a rate of 1.02 W/A .

As one lasing frequency dominates when the threshold current is exceeded, the spectral profile of the laser diode narrows considerably around the dominating frequency. This is shown in figure 3.4.

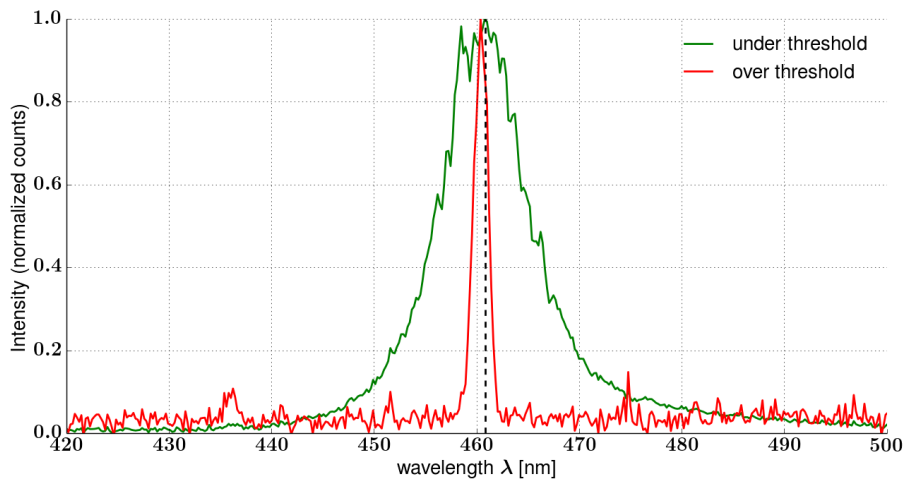


Figure 3.4: Laser diode output spectra for currents above and below the threshold current for a fixed diode temperature of $T = 40^\circ \text{C}$. For currents below the threshold current, the spectrum is broad as shown by the green curve. The dotted line shows the wavelength of interest for our experiment, naturally contained within the gain spectrum. As the threshold current is exceeded, the spectrum narrows considerably (red curve). The data was recorded using an Ocean Optics USB4000 spectrometer.

3.2 Cooling Light Generation

Further increasing the laser diode input current continues to change the output spectrum as shown in figure 3.5. The laser diode current changes the lasing frequency through two mechanisms. Firstly, changes in the cavity geometry and index of refraction occur via temperature changes dependent on the diode current. Secondly, the population inversion augmentation resulting from a current increase results in linewidth broadening effects which is outside the scope of this thesis [13].

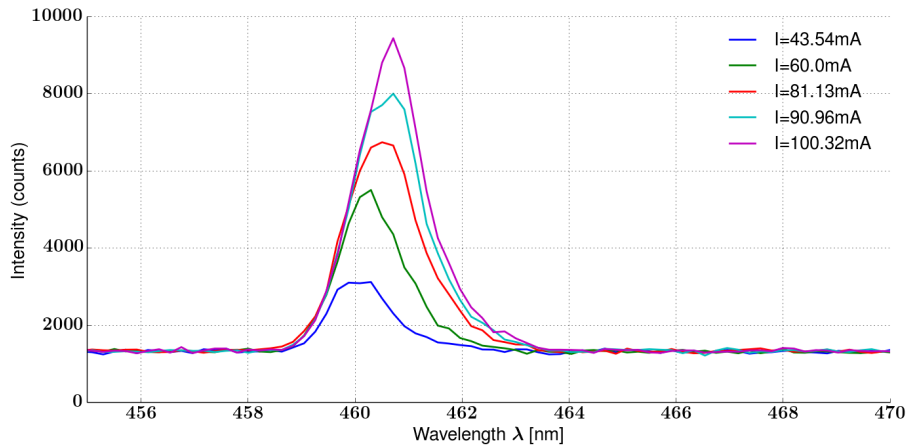


Figure 3.5: Laser diode spectrum for different input currents at $T = 40^\circ\text{C}$. The data was taken with an Ocean Optics USB4000 spectrometer.

The laser diode is highly sensitive to temperature changes as material expansion leads to fluctuations in the internal cavity length, thus altering its resonant modes.

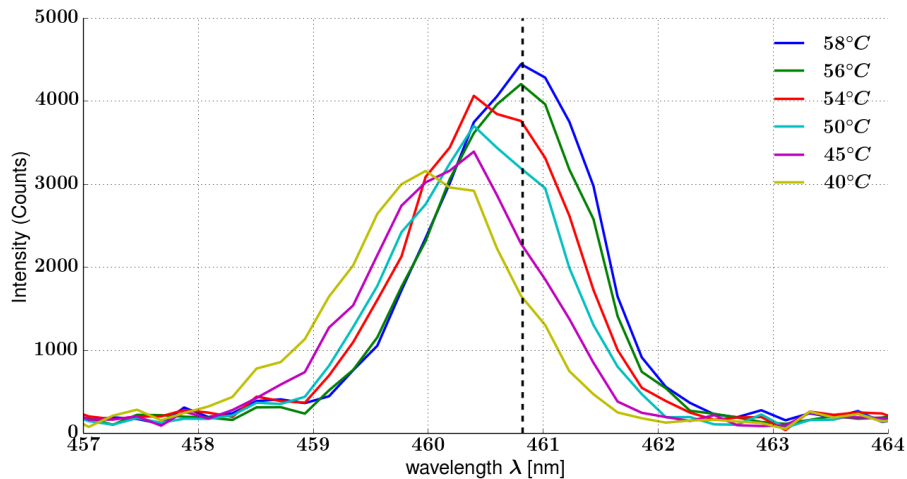


Figure 3.6: Laser diode Spectrum at different temperatures and fixed input current $I = 50 \text{ mA}$. According to the laser diode data sheet, the absolute maximum laser diode temperature is of 60°C (Lower limit of $4.6 \text{ k}\Omega$ on the thermoelectric temperature controller). The data was taken with an Ocean Optics USB4000 spectrometer.

3.2 Cooling Light Generation

Control over the diode temperature is thus necessary and will also allow some control over the spectrum produced. Temperature stabilization is achieved by a THORLABS TED200C thermoelectric temperature controller through a Peltier element and thermistor in close proximity to the laser diode. The Peltier element is a small semi-conductor creating a temperature gradient between its two sides when a voltage is applied over it. Figure 3.6 shows the laser diode output spectrum at varying temperatures for a fixed diode current. As can be seen, the laser diode spectrum shifts as function of temperature. The peak intensity also increases as function of temperature and thus higher laser diode temperatures are desired in our experiment.

According to the Nichia diode data sheet, the absolute maximum power allowed inside the laser diode is 120 mW. In order not to exceed this setting, the maximum allowed laser diode current is investigated. As the diode temperature physically changes the length of the gain medium, the threshold current I_t is altered as well since changing the cavity length alters the round trip losses of light. The laser diode power is thus temperature dependent. The threshold current as is plotted as function of temperature in figure 3.7.

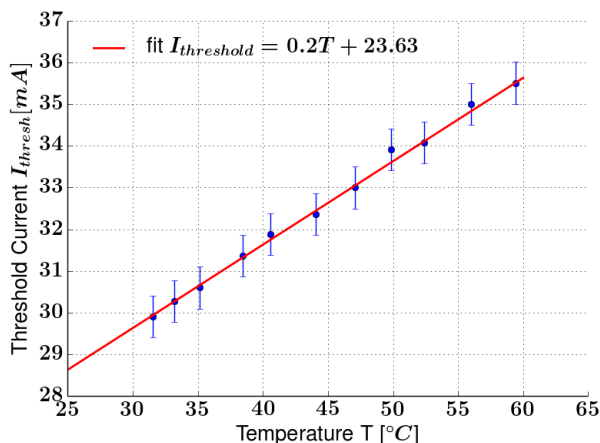


Figure 3.7: Laser diode threshold current as function of temperature. The threshold current increases linearly with the temperature as $I_{thresh} = 0.2T - 23.63$.

Combining the results from figure 3.3 and 3.7, the maximum allowed current flowing through the laser diode is computed. The maximum allowed current is shown in figure 3.8 as function of temperature and resistance of the 20 k Ω thermistor resistance as read by the THORLABS TED200C thermoelectric temperature controller stabilizing the temperature of the laser diode. The relation between the resistance of the thermistor and its temperature is given in the THORLABS data sheet [30].

3.2 Cooling Light Generation

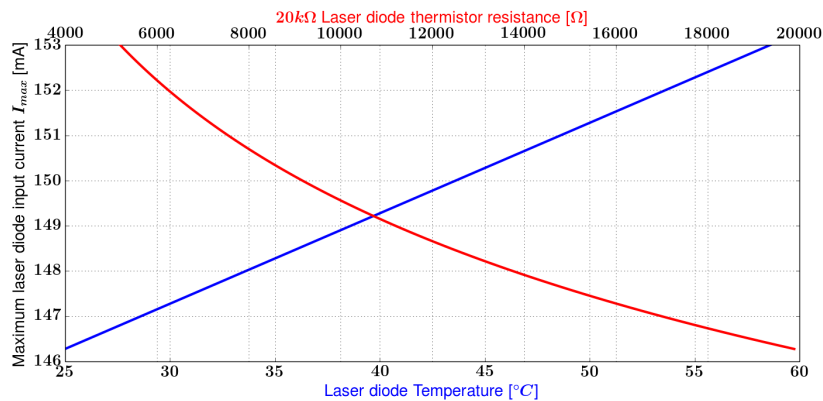


Figure 3.8: Maximum laser diode input current as function of laser diode temperature and thermistor resistance. The relation between the temperature and resistance can be found in the THORLABS data sheet [30].

3.2.2 ECDL

Having characterized the laser diode in the previous section, we now turn to its use within the ECDL. The ECDL mount is composed of a large aluminum block on which all the optical elements are mounted. A schematic drawing of the ECDL setup used is shown in figure 3.9. The aluminum block is enclosed within a box to isolate the optics from outside temperature fluctuations.

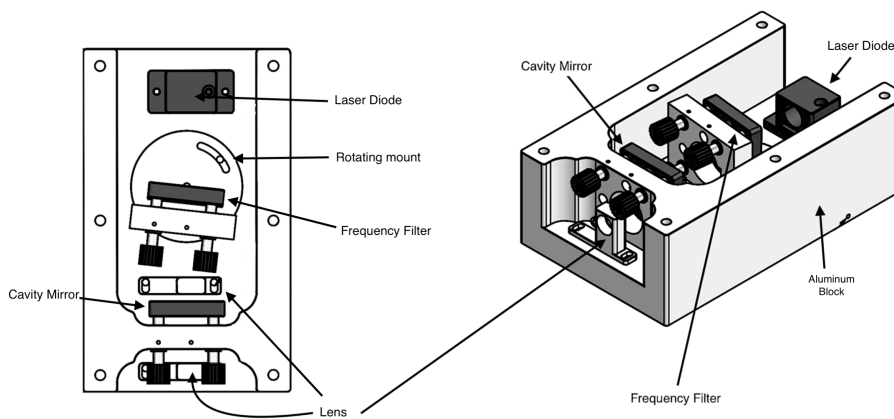


Figure 3.9: Schematic drawing of the ECDL mount. All optical elements are mounted on an aluminum block, itself enclosed within a box. The frequency filter is mounted on a rotating mount to allow fine tuning of its orientation. Lenses are placed before and after the external cavity mirror to collimate and adjust the laser beam.

As the ECDL lasing frequency is sensitive to changes in the external cavity length, the ECDL mount was temperature stabilized with a heating element located underneath the aluminum block. A description of the temperature controller regulating the ECDL mount temperature is presented in section 3.3.

3.2 Cooling Light Generation

Due to the presence of the external cavity, a larger amount of power is present within the laser diode as a portion of the light will be reflected on the external cavity mirror of the ECDL. The absolute maximum laser diode input current is thus altered. Assuming that the back of the laser diode has unity reflectance $R_1 = 1$ and using equation 2.8, we can find the maximum allowed power inside the diode given an optimized cavity with a frequency filter placed in its center. The reflectance of the external cavity mirror was measured to be $R_2 = 0.3$. For optimal filter orientation, the filter transmittance was measured to be $T_f = 0.2$. Computing the power inside the laser diode, e.g at the mirror with unity reflectance at the back of the diode, we have that $\phi = 0$. The power inside the cavity is thus given by,

$$P = \frac{P_0}{1 + T_f^2 R_2} \quad (3.7)$$

Inserting the maximum allowed power inside the diode $P = 120$ mW in the above equation and isolating for P_0 , we find that the diode emitted power must not exceed $P_0 = 95$ mW. The corresponding laser diode input current is plotted in figure 3.10 once again as function of temperature and 20 k Ω thermistor as read by the THORLABS controller. Due to the presence of the external cavity, lower laser diode input currents are allowed as some of the laser light is reflected back into the diode. This will also reduce the laser output power.

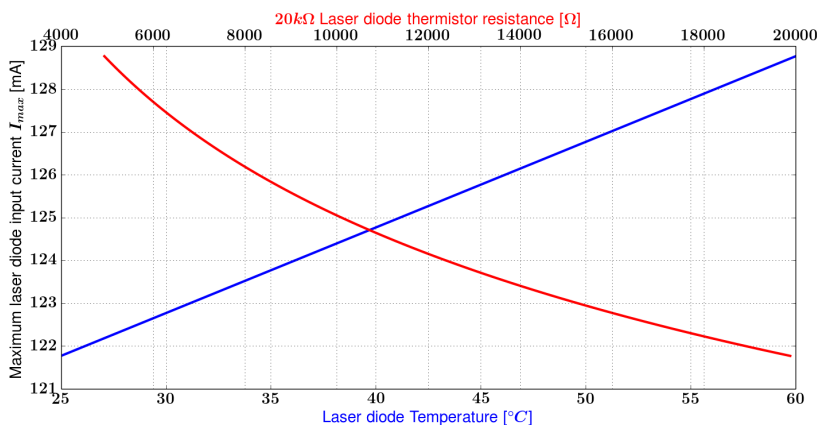


Figure 3.10: Maximum laser diode input current with external cavity and frequency filter as function of temperature and thermistor resistance as read by the THORLABS thermoelectric temperature controller.

3.2.3 Injection

Injection is the process through which the laser output is optimized so as to obtain a stable single mode lasing. The injection parameter space is a 4-dimensional parameter space composed of the diode temperature, diode current, cavity mirror position and frequency filter position. The cavity length can be fine tuned through the piezoelectric element located behind the external cavity mirror.

3.2 Cooling Light Generation

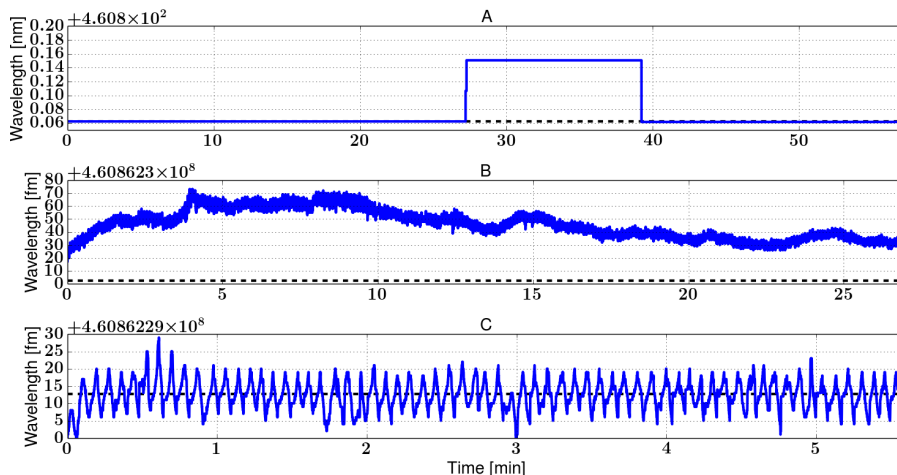


Figure 3.11: Lasing wavelength of the injected ECDL. A) lasing wavelength over 30 minutes. Two mode jumps occur as the lasing frequency cannot be sustained anymore. B) Zoom on the 27 first minutes of plot A) showing the slow drift in lasing wavelength. C) ECDL lasing wavelength as the piezoelectric element position was constantly manually tuned.

The frequency of the laser was monitored by a high finesse wavelength-meter to ensure injection at the atomic cooling transition frequency. We expect to find a parameter-set that results in a lasing frequency independent of small changes in the diode current and cavity length, suggesting a stable lasing mode and thus, injection. During the process, the ECDL mount was temperature stabilized by the temperature controller described in section 3.3. In light of the diode and ECDL characterization presented above, we are looking for a stable mode at high diode current as this will maximize laser output power.

A stable lasing frequency is found close to the relevant atomic resonance for up to almost half an hour but was observed to slowly drift until the mode could not be sustained anymore, resulting in a sudden mode jump of a few MHz as can be seen on plot A of figure 3.11. Plot B shows the slow drift in lasing wavelength of the 27 first minutes of plot A. The drift is most likely dominated by changes in the external cavity length due to the imperfect mount temperature stabilization. As is shown in plot C, the lasing wavelength could be maintained stable with minimal deviation around the cooling transition wavelength for 5 minutes by manually correcting the cavity length through the piezoelectric element. This suggests the lasing frequency could be stabilized by automatizing the correction on the cavity length. The laser mode was also independent of tiny changes in the diode current which in turn could also be used to stabilize the lasing frequency. Many different injection modes were found, some more stable than others and a stronger mode than the one shown in figure 3.11 can potentially be found. The output power of the ECDL for the lasing mode of figure 3.11 was measured to be 30mW.

In order to stabilize the lasing frequency to the relevant atomic transition, a feedback loop could be formed by monitoring the atomic fluorescence generated

3.2 Cooling Light Generation

by spectroscopy with the ECDL light as measured by a photodiode. As the atomic fluorescence is highest when the frequency of the laser light equals that of the atomic transition, the measured fluorescence signal could be processed by a computer program, adapting the external cavity length to maximize the intensity of the photodiode signal, in turn maintaining a stable lasing frequency locked at the atomic cooling transition. A schematic of a setup capable of realizing such feedback loop is shown in figure 3.12.

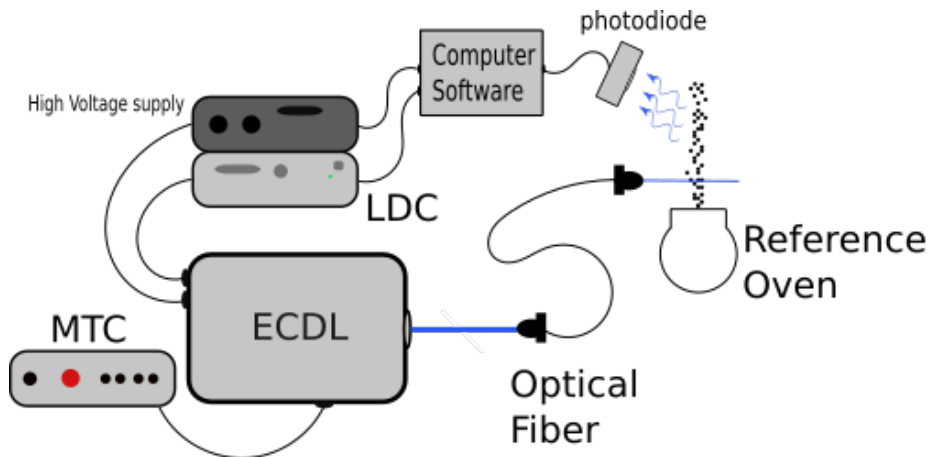


Figure 3.12: Schematic of a feedback loop with a reference oven. The ECDL output light is coupled to an optical fiber to perform spectroscopy on the atoms of a reference oven. The fluorescence is measured by a photodiode and processed by a computer software to adjust the cavity length through a piezoelectric element to maintain the lasing frequency on resonance with the atoms. The ECDL mount is temperature stabilized by the mount temperature controller (MTC) described in section 3.3.

3.2.4 Experimental Setup

In this section, the experimental setup necessary to divide and manipulate the cooling light from the ECDL is presented. An illustration of the experimental setup built during this project is shown in figure 3.13. As the expected 30 mW of power produced by the ECDL is insufficient for efficient cooling purposes, a Slave laser has been added to the setup. The Slave laser contains the same blue laser diode as the ECDL and will act as an amplifier through injection locking. Injection locking is the process through which light from a master laser, possessing the desired light properties, is used to stimulate emission within the gain medium of a slave laser. The slave laser output thus mimicking the light properties of the master laser. Through this injection locking process, the Slave laser output will inherit the ECDL light. The Slave laser is expected to deliver up to 120 mW of power and will be used solely for laser cooling.

Due to the rectangular geometry of the laser diode gain medium, the emitted ECDL light has an elliptical beam shape, diverging more in one axis than the other. Lenses were placed in front of the ECDL to collimate and alter the elliptic beam shape to a Gaussian beam shape in order to ease optical fiber in-coupling and future beam matching processes. An Optical Isolator (O.I) is placed after

3.2 Cooling Light Generation

the beam shape correction lenses in order to prevent possible frequency noise in the diode from reflections from the rest of the setup.

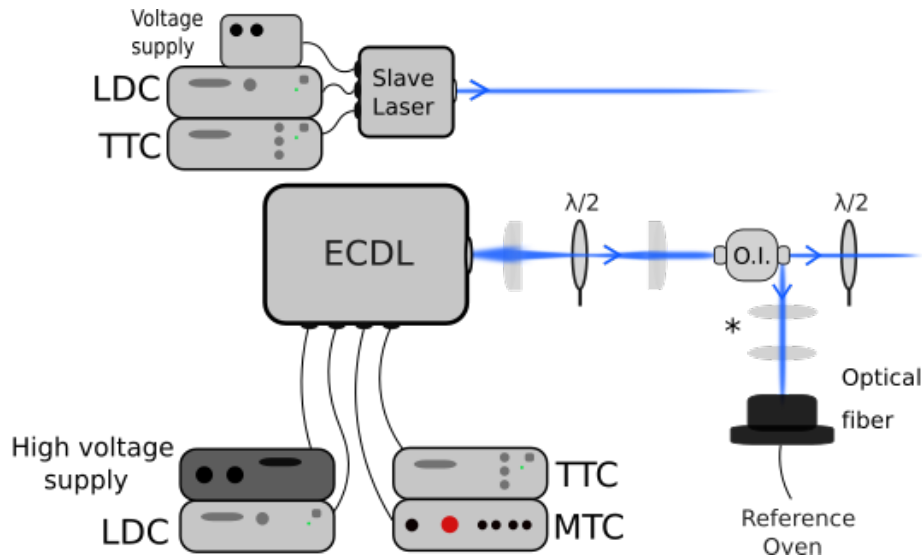


Figure 3.13: Schematic of the Experimental setup. Both the ECDL and slave laser are hooked to a THORLABS LDC200C laser diode controller (LDC) and a THORLABS TED200C thermoelectric temperature controller (TTC). The mount temperature control (MTC) regulating the mount temperature of the ECDL is described in section 3.3. A constant voltage is applied over the Slave laser heating element to provide a heat sink for the Peltier element regulating its diode temperature. An Optical isolator (OI) is used in order to prevent frequency noise inside the laser diode. Part of the ECDL light reflects through one of the rejection ports of the O.I and is coupled to an optical fiber. Lenses are placed in front of the ECDL and optical fiber in order to collimate and optimize the beam shape.

A $\lambda/2$ plate is used to control the diode polarization for optimal transmission through the optical isolator. One of the rejection ports of the optical isolator is used to couple light to an optical fiber. The latter will be used to construct the feedback loop with the reference oven mentioned previously. Ideally, 1 mW of power is used for fiber in-coupling, leaving 29 mW to be appropriately divided for the cooling and the Slave laser. The fiber is attached to a cylindrical lens holder in which the position of a 5 mm aspheric lens can be optimized. By optimizing the position and focal length of the lenses in front of the fiber and the position of the aspheric lens, fiber transmissions of 30% were obtained. Transmissions of at least 50% are desired. The low transmission is attributed to a poor laser beam shape.

The setup has to be extended so as to deliver part of the ECDL light for the Zeeman slower, 2D MOT and optical molasses through injection locking of the Slave diode.

3.3 Temperature Stabilization

Minuscule changes in the ECDL external cavity length due to environmental temperature fluctuations can have a detrimental effect on the stability of its lasing frequency. It is thus crucial to stabilize the temperature of the whole ECDL mount. The temperature of the Slave laser mount is also relevant in order to provide a heat sink for the Peltier element regulating the diode temperature. Temperature stabilizing the Slave laser mount might also facilitate the injection locking process. In this section, the controller stabilizing the mount temperature of the ECDL and Slave laser mount is described. Firstly, the ideal stabilization temperature for both mounts is found. Then a description of the 3 main parts composing the controller; the sensor, control and actuator, is presented. Finally, the performance of the mount temperature controller is analyzed.

The working mechanism of the Mount Temperature Controller (MTC) can be separated into 3 distinct parts. A sensor part, a control part and an actuator part. The sensor part measures the temperature of the mount and sends the measured signal to the control part. The latter processes the received signal and computes an appropriate response for the actuator part to heat the system accordingly. A feedback loop is formed as the mount temperature is continuously measured and processed to provide an appropriate response of the heating element, thereby stabilizing the mount temperature. A basic block diagram schematic of the temperature control scheme is shown in figure 3.14. The inner-workings of each part is investigated in the following sections. Initially, the controller was designed to stabilize the temperature of the ECDL and Slave laser mounts simultaneously. The controller was however focused on the stabilization of the ECDL mount temperature due to unavoidable cross talk as both mounts were stabilized simultaneously as investigated in section 3.3.5.

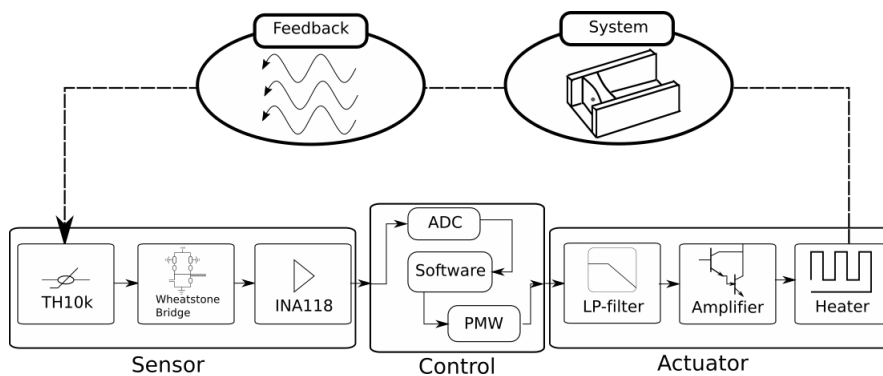


Figure 3.14: Simplified block diagram schematic of the mount temperature controller mechanism. It is composed of 3 main parts: the sensor part, the Arduino which composes the control part and the actuator part. All elements from the Wheatstone bridge to the amplifier included were mounted onto a breadboard alongside a power supply and enclosed within a box.

3.3 Temperature Stabilization

3.3.1 Optimal Stabilization Temperature

As the laser mounts are heated through Joule effect in the heating elements, the mount temperature controller can only actively heat. Cooling is effectuated through heat dissipation to the environment. The optimal mount stabilization temperature can thus be found where the heating rate equals the cooling rate. The optimal stabilization temperature of the ECDL and Slave laser mounts will differ greatly due to the different material, size and mass of their mount and their respective heating element.

A $10K\Omega$ thermistor, a temperature dependent resistor, is used to measure the ECDL and Slave mount temperatures. This thermistor is said to be "in-loop" as its resistance is used to compute the error signal in the feedback loop. The resistance of the in-loop thermistor was monitored as the ECDL and Slave mounts were maximally heated and cooled. The respective heating and cooling rates were then computed through differentiation of the mount resistance as function of time. The results are shown in figure 3.15.

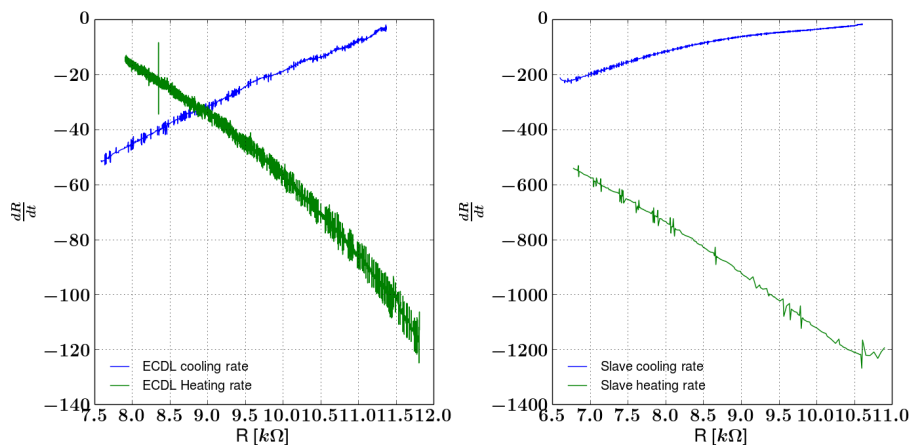


Figure 3.15: ECDL and Slave mount maximum heating and cooling rates.

The intersection between the cooling and heating rate of figure 3.15 instruct us with the optimal stabilization resistance. Using the THORLABS data sheet ([30]) to convert the thermistor resistance into a temperature, we obtain the optimal mount stabilization temperature. For the ECDL, $R_{optimal} \approx 8780 \Omega$ which corresponds to a mount stabilization temperature of $T_{optimal} = 28^\circ C$. The low mass of the Slave laser mount and low resistance of its heating element causes large heating rates within a realistic temperature range. The ideal stabilization temperature was deemed too high as large currents would be needed to heat the mount accordingly and the Slave laser stabilization temperature was set to be $T_{Slave} = 35^\circ C$ which corresponds to a thermistor resistance of $R_{Slave} = 6532 \Omega$.

3.3.2 Sensing

In this section, a presentation of the inner-workings of the sensing part of the temperature controller is presented. The sensing part of the controller is divided in 3 individual parts as depicted in the figure 3.16. Initially the temperature of the system is measured by the 10 k Ω in-loop thermistor. The resistance of the in-loop thermistor, containing information about the temperature of the mount, is then measured by a Wheatstone bridge whose output signal is amplified by an Operational amplifier (Op-amp) before being processed by the control part of the circuit.

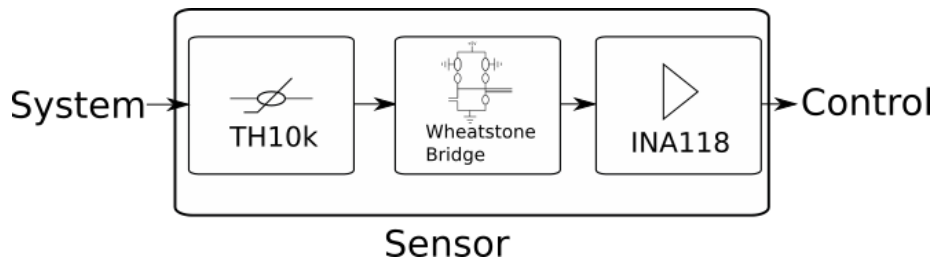


Figure 3.16: Schematic of the sensing part of the mount temperature controller. The system temperature is measured by a 10 k Ω thermistor with a Wheatstone bridge. The Wheatstone bridge signal is then amplified by a INA118 operational amplifier.

Wheatstone Bridge

In order to measure the resistance of an unknown component, in this instance the thermistor, and translate it to a voltage, readable by the control part of the system, we use a Wheatstone bridge. The Wheatstone bridge circuit, including the INA118 Op-amp is shown in figure 3.17. The transfer function of the Wheatstone bridge is given by,

$$\frac{U_{out}}{U_{in}} = \left(\frac{R_{11}}{R_4 + R_8 + R_{11}} - \frac{R_T}{R_3 + R_7 + R_T} \right) \quad (3.8)$$

where U_{out} and U_{in} are the output and input voltage, R_T is the thermistor resistance, $R_{7,8,11}$ are normal resistors on the bridge while $R_{3,4}$ are variable resistors or potentiometers, allowing for fine tuning of the Wheatstone bridge response. The voltage U_{out} is then amplified by a INA118 Op-amp. The Op-amp gain is a function of the gain resistor R_g (R_6 in figure 3.17) and is given by, [14]

$$g = 1 + \frac{50k\Omega}{R_g} \quad (3.9)$$

The input voltage range of the Arduino board which constitutes the control part of the system is 0 – 3.3V. Therefore, the resistors of the Wheatstone bridge are chosen so that the Wheatstone bridge voltage multiplied by the Op-amp gain lies within 0 – 3.3V as is approximately linear for thermistor resistances corresponding to temperature range of 2°C. The Wheatstone bridge response

3.3 Temperature Stabilization

is thus 1.6V when the mount is at the right temperature as measured by the in-loop thermistor. The values of the fixed resistors are shown on the Wheatstone bridge circuitry of figure 3.17. The potentiometers were experimentally tuned so as to obtain the Wheatstone bridge response shown in figure 3.18.

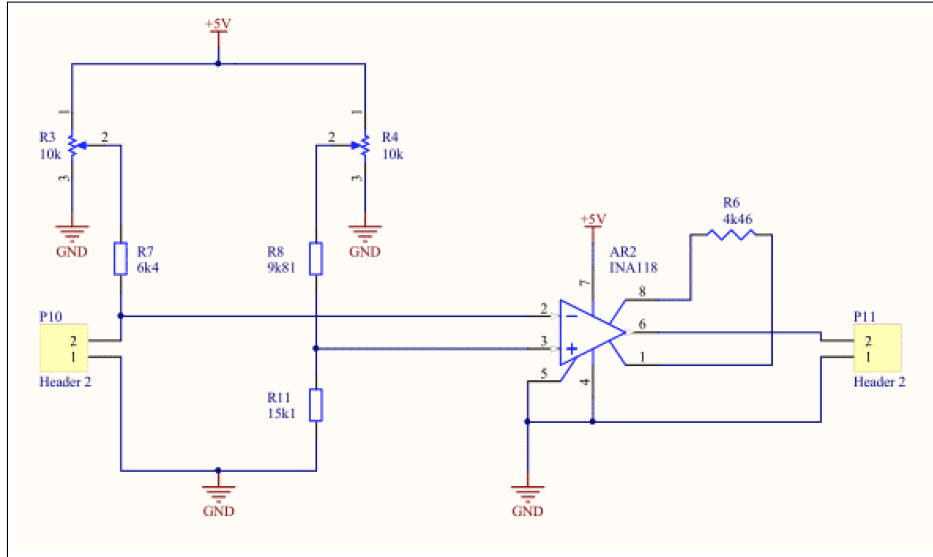


Figure 3.17: Wheatstone bridge circuit and INA118 Op-amp.

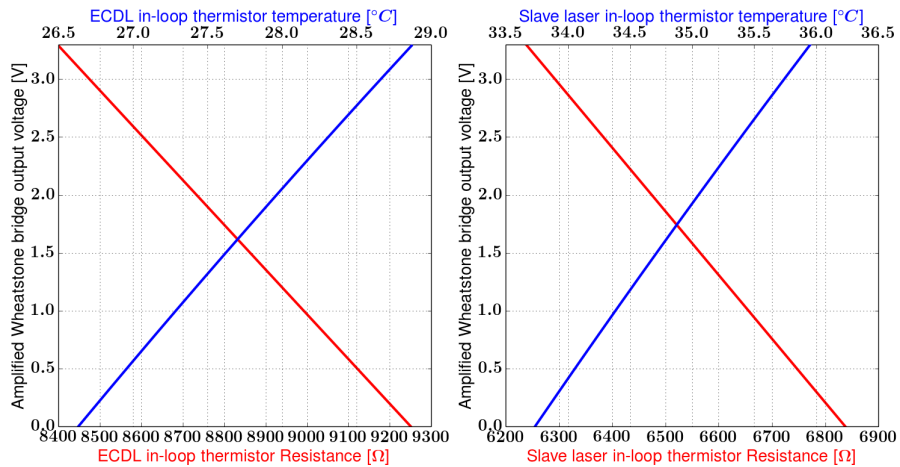


Figure 3.18: ECDL and Slave Wheatstone bridge output voltage as function of thermistor resistance and temperature.

The amplified signal of the Wheatstone bridges is then propagated to the control part of the mount temperature stabilization controller.

3.3 Temperature Stabilization

3.3.3 Control

In this section, we present the inner-workings of the control part of the mount temperature controller. We start by presenting a theoretical description of control theory. Then we present the experimental implementation of the theoretical system described and justify the use of a Proportional-Integral (PI) mechanism as control algorithm for our system.

Analysis

The objective of the mount temperature stabilization scheme is to match the output $y(t)$, i.e. the mount temperature, of a system G , to a control signal, or set-point $r(t)$, as faithfully as possible. This is effectuated by applying a control law K , altering the output signal $y(t)$ to minimize a computed error signal $e(t) = r(t) - y(t)$. In order to successfully describe the system at play, it is convenient to work in the frequency domain.

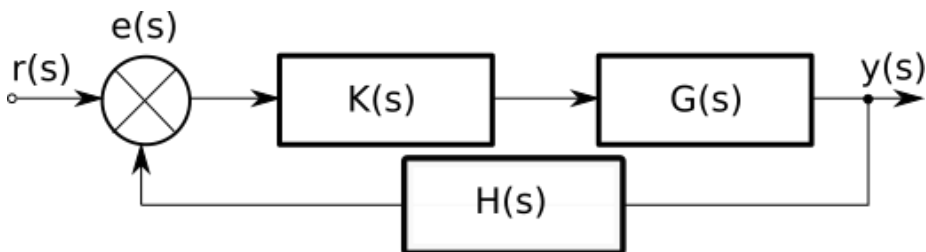


Figure 3.19: Schematic block diagram illustrating the signal flow through the different elements of a simplified feedback system. $K(s)$ is the transfer function of the control law and $G(s)$ the system transfer function. An error signal $e(s) = r(s) - y(s)$ is computed from the control signal $r(s)$ and the system's temperature $y(s)$. The response of the system to an error signal $e(s)$ is computed by a control part $K(s)$. $H(s)$ represent the sensor transfer function.

We define $f(s)$, a function in the frequency domain, as the Laplace transform of its equivalent in the time domain $f(s) \equiv \mathcal{L}[y(t)] = \int_0^\infty y(t)e^{-st} dt$, where $s = i\omega$ is the complex Laplace parameter and ω the angular frequency. Here, the real parameter σ of the full complex Laplace parameter $s = \sigma + i\omega$ is set to 0. A block schematic illustrating the signal flow from the input $r(s)$ to the system's output $y(s)$ is shown in figure 3.19. Here we have added a complex sensor dynamic $H(s)$ that can arise due to sensor noise or discretized sampling rate. In the time domain, the output $y(t)$ would be the convolution of the elements connected in series. In the frequency domain, the final output $y(s)$ is simply given by the product of the transfer functions of the different parts of the diagram. We can thus write,

$$y(s) = K(s)G(s)e(s) = \frac{K(s)G(s)}{1 + K(s)G(s)}r(s) \quad (3.10)$$

We define $T(s)$, the closed loop dynamics of the system, as the ratio of the system output $y(s)$ to the input $r(s)$ as, [25]

$$T(s) \equiv \frac{y(s)}{r(s)} = \frac{K(s)G(s)}{1 + K(s)G(s)} \quad (3.11)$$

3.3 Temperature Stabilization

The open loop dynamic of the system is given by $L(s) = K(s)G(s)$ and represent the system's behavior without feedback, thus a control law response $K(s)$ that does not depend on the system output $y(s)$. $T(s)$ represents the alteration of the system transfer function $G(s)$ due to the use of a control law $K(s)$ on the computed error signal $e(s)$. In other words, we want to choose $K(s)$ so that $T(s) = 1$ at long time scales $s \rightarrow 0$, meaning that the system output $y(s)$ perfectly follows the control signal $r(s)$. Experimentally, the transfer function $G(s)$ can be found by Laplace transforming the kick response or impulse response of a system. The kick response is a system's response to a delta function input and can be found by differentiating the step response, which is a system's response to a Heaviside step function. [25].

From the closed loop transfer function $T(s)$ of equation 3.11, one can see that if $K(s)G(s)H(s)$ ever equals -1 the response will be infinite, leading to an unstable system diverging endlessly. The real part of a transfer function corresponds to the magnitude of the frequency response while the imaginary part corresponds to the phase shift resulting from signal propagation. In other words, instability will occur when $|KGH| = 1$ or $\text{Re}\{T(s)\} = 1$ with a simultaneous phase lag of 180° or $\text{Im}\{T(s)\} > 180^\circ$. It is useful to represent a system's response as function as bode plots, plotting the real and imaginary part of the system transfer function in separate plots [25].

Proportional-Integral (PI) type control mechanisms are widely used in various control systems as they can provide fast and responsive control of the system output $y(s)$. As its name suggests, a PI mechanism is composed 2 parts, the Proportional part being directly proportional to the error and an Integral part, proportional to the magnitude of the sum of the preceding errors, in order to eliminate steady state errors. In the time domain, the PI response takes the form, [25]

$$u(t) = K_p e(t) + K_i \int_0^t e(t') dt' \quad (3.12)$$

where K_p and K_i are the Proportional and Integral gain parameters, respectively. In the frequency domain, equation 3.12 becomes, [25]

$$u(s) = K_p + \frac{K_i}{s} \quad (3.13)$$

Experimental Control

The control part of the temperature controller is executed by a programmable Arduino board. The control process can be divided into three main parts as shown in figure 3.20. Firstly, the signal received from the sensing part is converted from an analogue to a digital signal using the board's in-built Analogue to Digital Converter (ADC) with a 10 bit resolution. The Arduino software then computes an appropriate response to the sensed mount temperature through a control law $K(s)$. Finally, the Arduino outputs an analogue signal through its Pulse Width Modulation (PWM) pins.

3.3 Temperature Stabilization

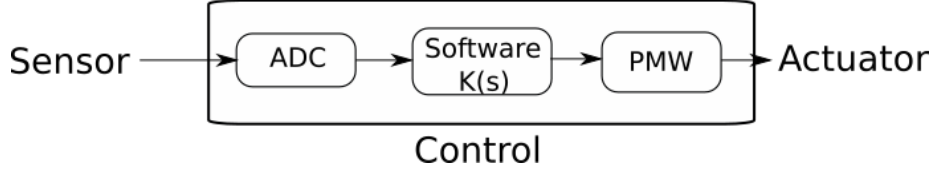


Figure 3.20: Schematic block diagram of the control part of the temperature controller.

The step response of the ECDL and Slave laser systems were measured separately by monitoring their respective response to the power supply’s maximum deliverable current. The results are shown in figure 3.21 and fitted to exponential functions which is a typical behavior for heat-reservoir systems. [15]

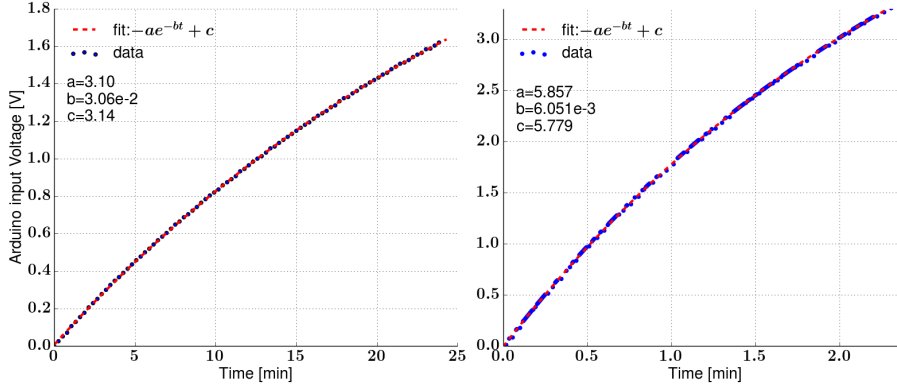


Figure 3.21: Step response of the ECDL and Slave laser systems measured separately. Arduino input voltage of the ECDL and Slave laser as function of time.

We obtain the kick response in the time domain through differentiation of the step response, yielding $\frac{d}{dt}(-ae^{-bt} + c) = abe^{-bt}$, which in turn can be used to find the system transfer function through Laplace transform $G(s) = \mathcal{L}[abe^{-bt}] = \frac{a}{1+s/b}$. This resembles a low-pass filter with a dc offset of a and cutoff frequency b .

The Arduino ADC utilizes the "Zero-order hold" method, freezing the input voltage over a certain sample period T_s in order to digitize the Wheatstone bridge output. This leads to a delay of $\Delta t = T_s/2$ in the digitized signal. The sensor transfer function due to digitization lag can thus be expressed as $H(s) = e^{-s\Delta t}$ [25].

Inserting the newly found system transfer function $G(s)$, the control transfer function $K(s)$ and the sensor dynamic $H(s)$ into equation 3.11, we obtain the closed-loop transfer function,

$$T(s) = \frac{a(sK_p + K_i)}{s + \frac{s^2}{b} + a(sK_p + K_i)e^{-s\Delta t}} \quad (3.14)$$

For long time scales and appropriate values of K_p and K_i , the closed loop

3.3 Temperature Stabilization

transfer function becomes,

$$\lim_{s \rightarrow 0} T(s) = 1 \quad (3.15)$$

which is the desired behavior of the system. The use of a PI-type mechanism is thus justified for temperature stabilizing the ECDL and Slave laser mounts and equation 3.12 was used within the Arduino software to compute the actuator response from the measured mount temperature. The gain parameters K_p and K_i have to be experimentally optimized to obtain a satisfying mount stabilization behavior. Without the digitization lag $H(s)$, the instability condition would never be satisfied in $T(s)$ for any values of K_p and K_i . The need for a phase lag of 180° indeed requires that the open-loop transfer function $L(s) = K(s)G(s)$ is of at least third order in s [25].

The Arduino code implementing the PI mechanism is integer based as *float* based variables would slow down the speed of the script and introduce noise. Values of K_p and K_i below 1 would result thus in a resolution loss due to the integer nature of the computed error $e(t)$. Using the gains $K_p = 1$ and $K_i = 0$ result in a temperature stabilization below set-point as shown in figure 3.22. Higher appropriate values of K_p could result in a stabilization around set-point but without an integral gain K_i , the mount temperature would sensitive to external temperature fluctuations over time. As displayed in figure 3.22, for the minimum gain parameters values $K_p = 1$ and $K_i = 1$ of the Arduino code, the ECDL mount temperature is unstable and displays large oscillations around set-point. This suggests a too large value of K_i . In order to reduce the significance of the Integral part of equation 3.12 by preventing it from accumulating large summation values without reducing K_i below 1, 3 different methods were implemented. Firstly, K_i is set to 0 until the mount temperature is close to set-point. Secondly, the error dependence of the Integral part is set to 1, yielding $K_i \int_0^t 1 dt'$ instead of $K_i \int_0^t e(t') dt'$. Finally, the sample rate of the ADC was reduced, limiting the summation rate of the Integral part of equation 3.12. The temperature stabilization of the ECDL mount after implementation of the correction methods mentioned above is shown in figure 3.22. As can be seen, the mount temperature is stabilized on set-point after 1 overshoot. The temperature stabilization can be improved by implementing fixed-point variables in the script, allowing for K_p and K_i values less than 1 without loss of resolution, circumventing the necessity for the aforementioned correction methods.

The Arduino is powered by 5V pins of the power supply and is mounted and grounded on the breadboard inside the box. The PWM pins used to forward the signal to the actuator output a voltage in the range $0 - 3.3$ V with an 8 bit resolution. The PWM pins simulate an analogue signal by creating a square wave and controlling the time during which the square pulse takes its maximum value, called duty time. Essentially, higher duty times increase the square pulse width [31]. To increase the power supply's efficiency, the actuator circuitry is build so that a minimum input voltage of 0 V, or the lowest PWM signal with duty time 0 produced by the Arduino, is converted to highest deliverable current from the power supply. Likewise, a 3.3 V output, or Arduino PWM output of duty time 1, is converted to 0 A to the heating elements, thus cooling the system. The wiring and layout of the Arduino board is depicted in figure B.1.

3.3 Temperature Stabilization

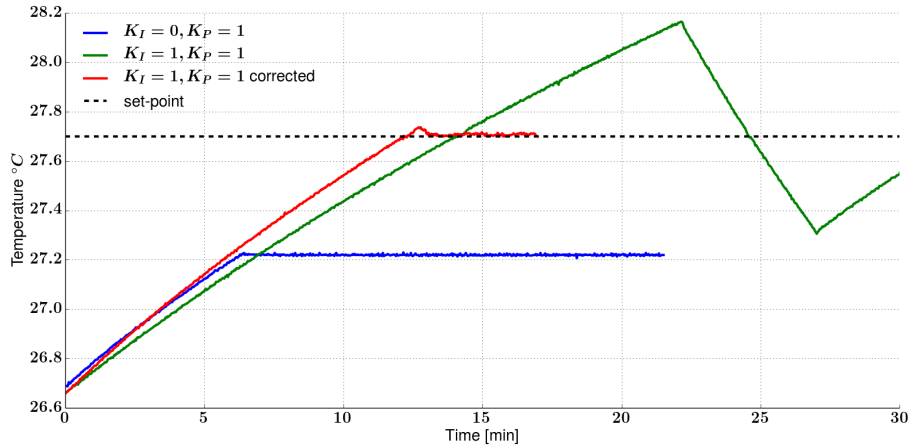


Figure 3.22: ECDL mount temperature for different gains K_p and K_i .

In order to avoid overheating the laser mounts, the code disables the temperature control if the respective Arduino input value is higher than 3.3 V, corresponding to a measured mount temperature of at least 1°C above set-point. A red Light Emitting Diode (LED) was mounted onto the front panel of the MTC box. It is set to light up when the mount temperature of the ECDL lies within approximately 10^{-2}°C of the set-point temperature, confirming a temperature stabilized mount.

3.3.4 Actuating

A schematic block diagram of the three different elements composing the actuating part of the system is shown in the figure 3.23.

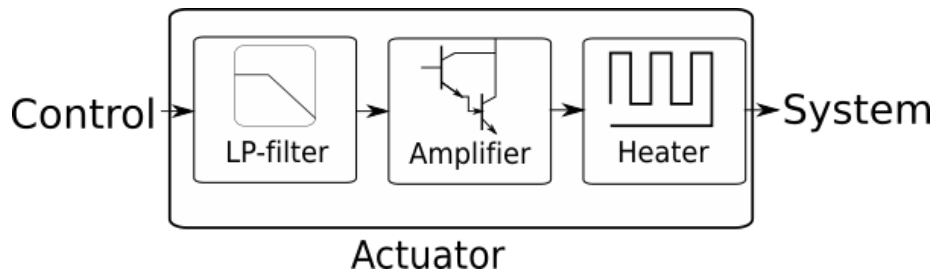


Figure 3.23: Schematic block diagram of the different elements composing the actuator part of the temperature controller.

The actuator part is composed of an electrical circuit, separated for the ECDL and Slave laser, comprising the two first elements of the block diagram of figure 3.23. The actuator circuit includes an RC-circuit or low pass filter. The latter attenuates high frequency signals and thus in effect reduces fast oscillating noise in the system. The actuator circuit also includes a Darlington

3.3 Temperature Stabilization

pair which is used to amplify the signal before the heating elements. The latter is composed of two transistors connected such that the current amplified by the first one is further amplified by the second one, leading to high current gains. The voltage over the collector-emitted junction of the Darlington pair is regulated by a potentiometer. The latter can be tuned to adjust the current drawn on the power supply. The power supply can deliver a maximum of 1 A. The ECDL heating element is located underneath the aluminum block on which all the optics is mounted and has a resistance of $R = 87\Omega$. The Slave laser has a smaller heating element of $R = 47\Omega$. As mentioned previously, the laser mounts are heated through Joule effect in their respective heating element.

3.3.5 Performance

The current needed to stabilize both the ECDL and Slave exceeds the 1 A deliverable by the power supply of the temperature controller. This results in instabilities when both mounts are stabilized simultaneously as shown in figure 3.24. When the Slave temperature stabilization is disabled, marked by a vertical black line in figure 3.24, the ECDL suddenly regains its stability.

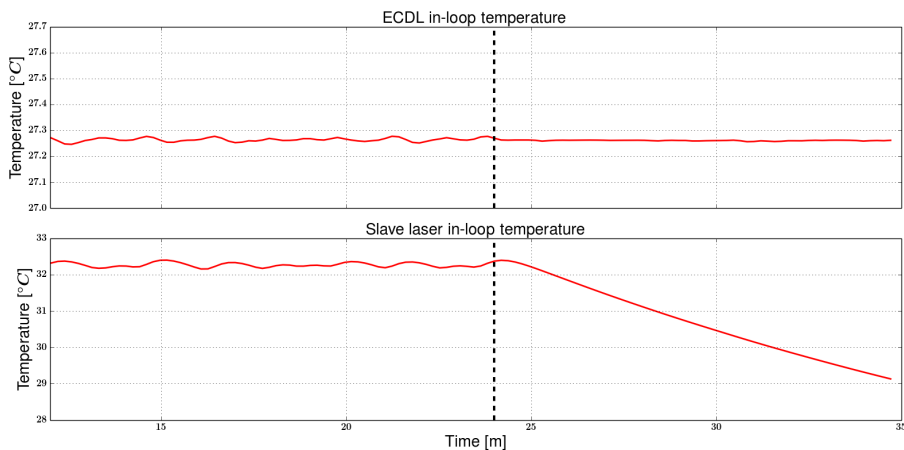


Figure 3.24: Instability in the mount temperatures of the ECDL and Slave lasers. The dashed black line marks the time at which the Slave mount temperature control was disabled.

Different values of the potentiometer regulating the voltage over the collector-emitter junction of the Darlington pair were experimentally tested in hope of reducing the maximum current drawn from the power supply and eliminate crosstalk between the ECDL and Slave laser. Unfortunately values of the potentiometer resistance supporting the simultaneous stabilization of the ECDL and Slave mounts were not found.

As it is important to provide a heat sink for the Peltier element regulating the diode temperature, the Slave mount was set to be heated through a constant voltage applied over its heating element. Without a controller, external

3.3 Temperature Stabilization

temperature fluctuations are not taken into account and the mount temperature drifts slowly with time as displayed in figure 3.25. The heated Slave mount temperature drift still presents an improvement of almost 1 order of magnitude and a raised mean temperature over the non-heated mount.

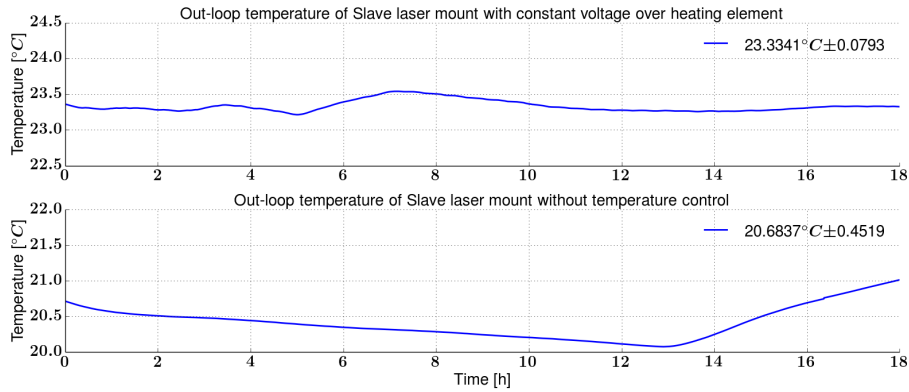


Figure 3.25: Slave laser mount temperature on external voltage supply.

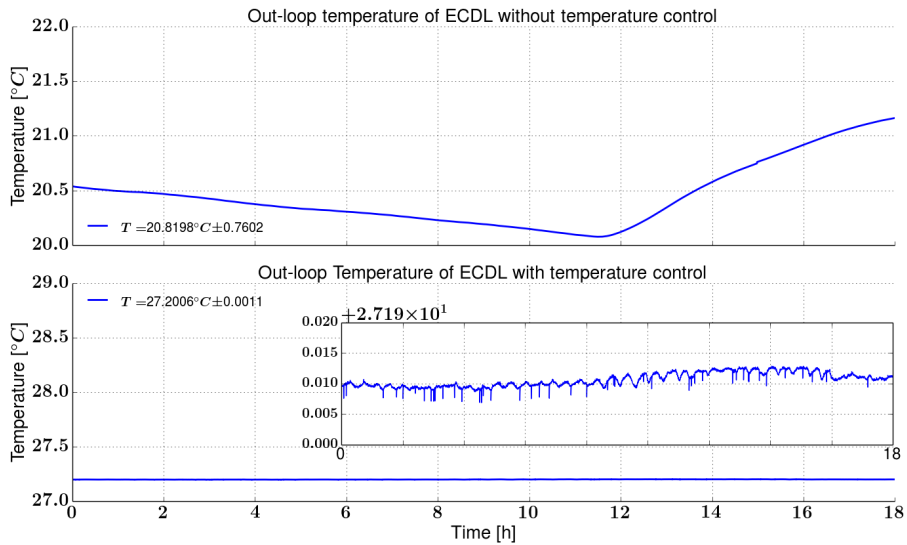


Figure 3.26: Comparison of the temperature of the stabilized and non-stabilized ECDL mount. The resistance of an out-loop thermistor, close to the external cavity was measured through 4-wire measurement with an AGILENT digital multimeter and converted to temperature.

As the blue diodes are very sensitive to temperature fluctuations, a separate mount temperature control might be needed to achieve successful injection locking of the Slave laser. In view of the instabilities, the temperature controller was set to stabilize solely the ECDL mount as its temperature is more important

3.3 Temperature Stabilization

than the Slave mount.

Within the ECDL, the in-loop thermistor is located a few centimeters from the external cavity mirror, where a stable temperature is most important. In order to get a more accurate temperature representation, an 'out-loop' thermistor was placed inside the aluminum block near the external cavity mirror. After experimentally optimizing the different parameters of the temperature controller, the resistance of the ECDL out-loop and thermistor was monitored over 18 hours with an AGILENT digital multimeter. In order to eliminate the resistances from the wires in our measurements, a 4-wire measurement was performed. The out-loop temperature of the ECDL mount is shown in figure 3.26. As can be seen, stabilization to the millidegree Celcius level was achieved, providing an amelioration of over 2 orders of magnitude in the mount temperature drift. The observed spikes are considered errors in measurements as they are unphysical.

The slow drift in the stabilization temperature is attributed to a change in the resistance of the Wheatstone bridge resistors due to slow temperature changes in the laboratory, creating a bias in the stabilization temperature.

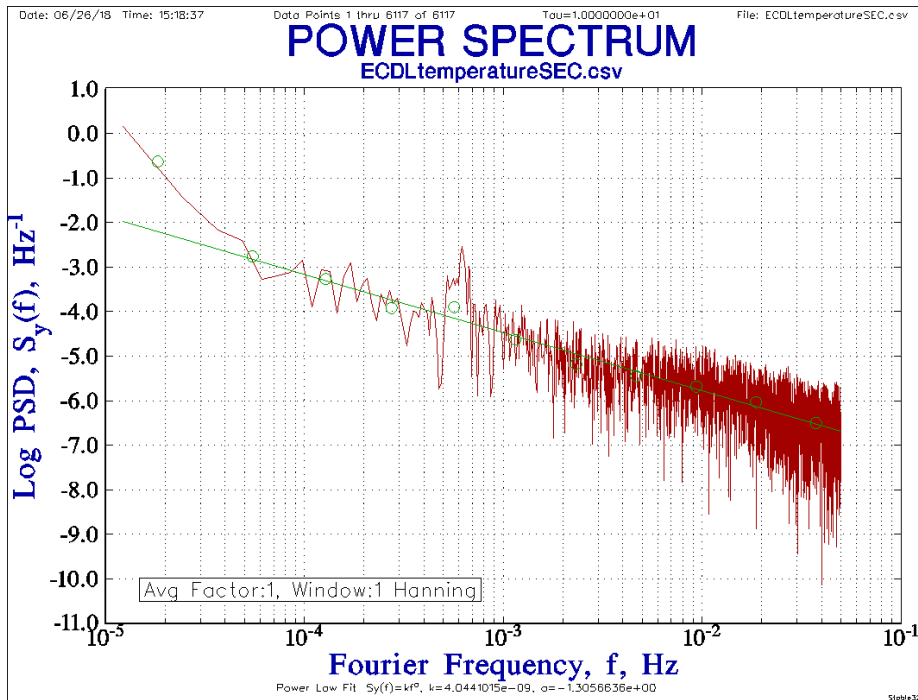


Figure 3.27: Power spectral density of the measured stabilized ECDL mount temperature.

In order to better understand the noise processes taking part in the ECDL mount temperature, the Power Spectral Density (PSD) of the signal is computed. The latter describes how much power of a time signal is distributed amongst which frequencies. It is found by computing the expectation value of

the square of the Fourier transform of a signal over a period T as, [1]

$$S_y(f) = \lim_{T \rightarrow \infty} \frac{1}{T} \int_0^T |y(\hat{t})|^2 dt \quad (3.16)$$

where $y(\hat{t})$ is the Fourier transform of the signal over time $y(t)$. The power spectral density of the ECDL mount temperature is presented in figure 3.27.

As can be seen, low frequency noise processes dominate the system. Eliminating these can be very difficult as their source is difficult to localize. The spike in the PSD at $\sim 10^{-3}$ Hz, corresponding to timescales of about 30 minutes is attributed to the air-conditioning fan activation of the laboratory temperature stabilization system. Further thermal isolation of the controller box containing the electronics could eliminate some low frequency drift and improve the temperature stabilization of the ECDL mount.

4 Cold Strontium Beam

In order to achieve continuous interrogation of atoms within the interrogation cavity at the end of the beamline depicted in 1.3, controlled atomic velocities along all axes are required. The first necessary cooling stage are the optical molasses at the oven output, transversely cooling the atomic beam and increasing the amount of atoms propagating through the beamline. To investigate to what extent these requirements can be met in theory, a Monte Carlo simulation, a simulation based on random sampling to obtain numerical results, of the propagation of the atomic beam through part of the beamline was developed. In this section, a description of the simulation and its pertinence is presented along with the obtained results. Hopefully, the results will provide insights on the optimal parameters governing the optical molasses efficiency and save optimization time in the laboratory. At the end of this section, the efficiency of the old oven, through which the atoms effused out of an exhaust hole, was compared with the new oven, containing a microchannel array.

The part of the beamline through which the atoms are propagated in the simulation is illustrated in figure 4.1. It is divided into 3 different sections: The oven, the effusion medium and the zone immediately after designed for the optical molasses described in section 4.2. The atoms are collected at the input area of a selection tube after the optical molasses zone. Here, the effusion medium refers to the microchannel array in the case of the new oven and the effusion hole in the case of the old oven.

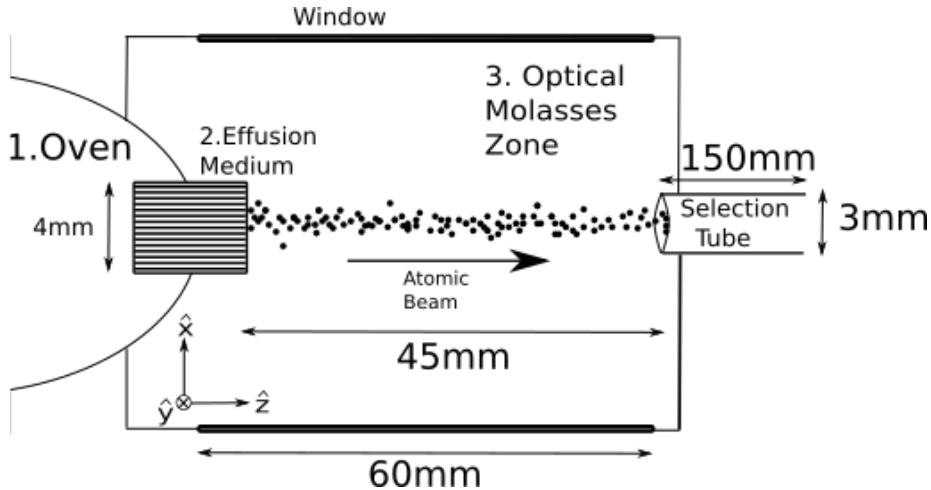


Figure 4.1: Schematic of the 3 part of the beamline: the oven, the effusion medium and the optical molasses zone, through which the atomic propagation is simulated. Two pairs of orthogonal windows allow for the insertion of laser beams into the optical molasses zone to cool the atomic beam. The atomic velocities and position are collected at the selection-tube input area. The schematic is not to scale.

4.1 Oven and effusion

Strontium atoms are present in solid form inside the oven. When the oven is heated the atoms become gaseous and their speed follows the 3 dimensional Maxwell-Boltzmann distribution,

$$f(v) = \left(\frac{m}{2\pi k_B T}\right)^{\frac{3}{2}} 4\pi v^2 e^{-\frac{mv^2}{2k_B T}} \quad (4.1)$$

where m is the mass of the ^{88}Sr isotope, k_B is the Boltzmann constant and T is the temperature. In the above equation, $v^2 = v_x^2 + v_y^2 + v_z^2$ is the total speed of the atom as function of the transverse velocities $v_{x,y}$, orthogonal to the atomic beam propagation direction, and propagation velocity v_z , parallel to the atomic beam propagation direction. The 3D Maxwell-Boltzmann distribution is shown in figure 4.2 for an oven temperature of 530°C (803 K). The most probable atomic speed of the distribution is given by $a = \frac{K_B T}{m}$ and is of $a = 276 \text{ m/s}$ for an oven at 530°C .

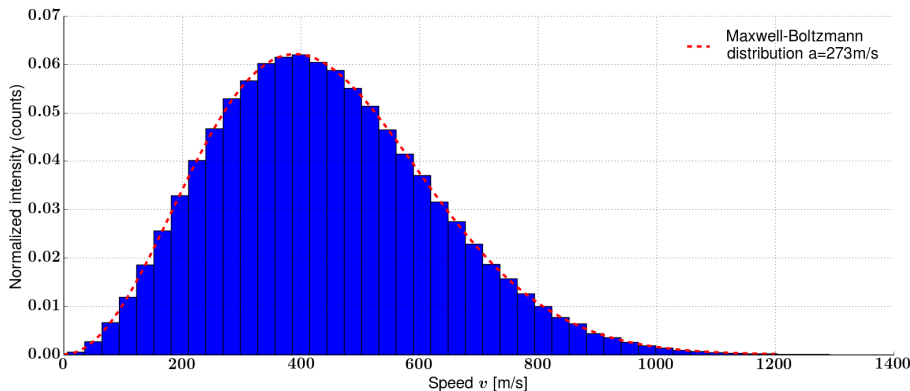


Figure 4.2: 3D Maxwell-Boltzmann speed distribution of ^{88}Sr at $T = 530^\circ\text{C}$ (803 K). The distribution is a Maxwell-Boltzmann distribution with most probable speed given by $a = \frac{K_B T}{m} = 276 \text{ m/s}$.

In the current beamline, the atoms effuse out of the oven through a microchannel array, a densely packed array of many small channels with a large length to diameter ratio $\frac{L}{d} \gg 1$. They are typically used in vacuum systems to increase beam collimation and conserve rare material [16]. Because of the small orifices of the microchannels, the thermal equilibrium inside the oven is left undisturbed and the velocity distribution of the atoms inside the oven will always follow the Maxwell-Boltzmann distribution of equation 4.1. Due to the extremely low pressures within the beamline, the atomic mean free path is much greater than any component in the beamline. We can therefore safely assume that the atoms collide with the walls more often than with themselves. Within this "Free-molecular flow regime", the Kinetic theory of gases provides a sufficient description of the physics of atomic propagation [18]. The atomic trajectories can thus assumed linear until an obstacle is met, and independent of the trajectories of other atoms. As no atom-atom collisions take place within

the microchannel array, we can, without loss of generality, simulate the propagation of each atom through a single one of the microchannels that make up the array as this will reduce computational time considerably. The layout of the microchannel array only becomes relevant for propagation beyond the array and into the optical molasses zone and is investigated in section 4.2.

Additionally to the Free-molecular flow regime assumption, two fundamental assumptions were made about the atomic propagation through the microchannel array. The first is that the atom-wall interactions are elastic; thus no energy will be lost upon interaction with a boundary. The total speed vector of each atom will thus be conserved throughout propagation. This is a good assumption as the array is close to the oven and has a high temperature. The second assumption is that the velocity of the atoms injected into the microchannel array from the oven as well as their diffusive reflection from a surface within the channels follows Knudsen's cosine law of reflection [16] [19] [21] [23]. The latter is described in the section 4.1.1. It is interpreted as an analogue to Lambert's law of reflection for light and can, for the case of the atom-wall interactions, be interpreted as an artifact of surface roughness as seen from the atoms perspective. The Cosine law states that the flux of atoms leaving a surface is independent of the previous atomic propagation direction. This means that atoms can be reflected back into the oven and never make it through the channel.

The simulation injects N atoms with velocities obeying equation 4.1 and the Cosine Law. The initial atomic positions on the input surface of the microchannel are randomly distributed [21]. The individual atomic positions are then linearly propagated until 1 of 2 events occurs. The first is that they leave the microchannel through the input or output surface, in which case the information about their position and velocities are, respectively, discarded or kept. The second is that they hit a boundary within the channel, in which case new velocities are sampled according to the Cosine Law. The simulation stops when all the atoms have left the channel.

4.1.1 Cosine Law Sampling

Under Free-molecular flow conditions, atoms leaving a wall are diffusively reflected according to the Cosine Law, without any memory of their initial angle of incidence. The Cosine law is also used to sample the angle of incidence of atoms entering a channel of the microchannel array [21]. In terms of polar and azimuthal angles, θ and ϕ , the Cosine law is given by [19],

$$dn = \frac{N_0}{\pi} \cos \theta \sin \theta d\phi d\theta, \quad N_0 = \frac{NAv_a}{4} \quad (4.2)$$

where dn is the atomic flux across a surface element of area A , N is the number density of atoms and $v_a = \langle v \rangle$, is the average atomic velocity. From this expression, the probability distribution of the polar and azimuthal angle $f(\phi)$ and $g(\theta)$ can be derived by integration over all azimuthal and polar angles,

respectively. Hence,

$$f(\phi) = \frac{1}{N_0} \frac{dn_\phi}{d\phi} = \frac{1}{\pi} \int_0^{\pi/2} \cos \theta \sin \theta d\theta = \frac{1}{2\pi} \quad (4.3)$$

$$g(\theta) = \frac{1}{N_0} \frac{dn_\theta}{d\theta} = \frac{1}{\pi} \cos \theta \sin \theta \int_0^{2\pi} d\phi = \sin(2\theta) \quad (4.4)$$

The velocity vector of each atom must obey the $f(\phi)$ and $g(\theta)$ distributions when entering a channel or bouncing off of a wall and can be sampled from those distributions. The velocity vectors are generated using the inverse transformation method, consisting of inverting the cumulative distribution function (CDF) of the normalized angular distribution functions. The CDF of a probability distribution function $h(x)$ is given by $F(x) = \int_{-\infty}^x h(x') dx'$. In the case of a continuous distribution, it gives the probability that the distribution function $h(x)$ takes a value between $-\infty$ and x . $F(x)$ thus takes values between 0 and 1. The polar angle can be generated from a single random number $F(x)$ in the range $[0, 1]$ by following the above steps on $g(\theta)$,

$$F(x) = \frac{\int_0^\theta g(\theta) d\theta}{C} = \sin^2 \theta \quad (4.5)$$

$$\theta = \arcsin \sqrt{F(x)} \quad (4.6)$$

where $C = \int_0^{\pi/2} \sin(2\theta) d\theta$ is the normalization factor and $F(x)$ is a number in the range $[0, 1]$. For the case of the azimuthal angular distribution, the generation of a random number in the range $[0, 2\pi]$ suffices since $f(\phi)$ is constant.

The generation of a direction vector in polar coordinates obeying the Cosine law can thus be found from 2 uniform random numbers. One can then find the 3 components of the generated vector in Cartesian coordinates that obey the cosine law through,

$$\hat{x} = \sin \theta \cos \phi \quad (4.7)$$

$$\hat{y} = \sin \theta \sin \phi \quad (4.8)$$

$$\hat{z} = \cos \theta \quad (4.9)$$

where \hat{z} is the Cartesian coordinate orthogonal to the surface the atom enters and \hat{x}, \hat{y} are the coordinates in the plane of that surface. The magnitude of the generated vector is here set to be 1 and hence has to be multiplied by the magnitude of the speed of the atom $v = \sqrt{v_x^2 + v_y^2 + v_z^2}$ in the simulation. [19]

4.1.2 Results

By making assumptions about the rate at which atoms hit the walls, one can derive a theoretical expression for the transmission probability of a channel. For a long cylindrical channel, the transmission probability depends uniquely on the radius and length and is given by $TP = \frac{8r}{3l}$ [16] [22]. In the current setup, the microchannels have a radius $r = 0.075$ mm and a length $l = 8$ mm, resulting in a theoretical transmission probability $TP_{theory} = 0.02500$. The Monte Carlo simulation yields, for channels of these dimensions, $TP_{MonteCarlo} =$

0.02512 ± 0.00015 .

The velocity distribution of the atoms at the input and output of the microchannel array is shown in figure 4.3. Due to the large length to diameter ratio of the channels, atom-wall collisions are frequent, resulting in a higher escape probability for atoms having low transverse velocity $v_{x,y}$ and high velocities along the tube axis v_z . The v_z velocity distribution fits to a Weibull distribution, $f_{weibull}(T) = \frac{\beta}{\eta} \left(\frac{T-\mu}{\eta}\right)^{\beta-1} e^{-\left(\frac{T-\mu}{\eta}\right)^\beta}$, a generalized Maxwell-Boltzmann distribution with displacement $\mu = 0$, shape parameter β and scale parameter η [20]. As expected, between the input and output of the channels, the transverse velocity distribution narrows while the v_z distribution shifts towards higher velocities. The total speed $v^2 = v_x^2 + v_y^2 + v_z^2$ of the atoms effusing from the channels still obey equation 4.1.

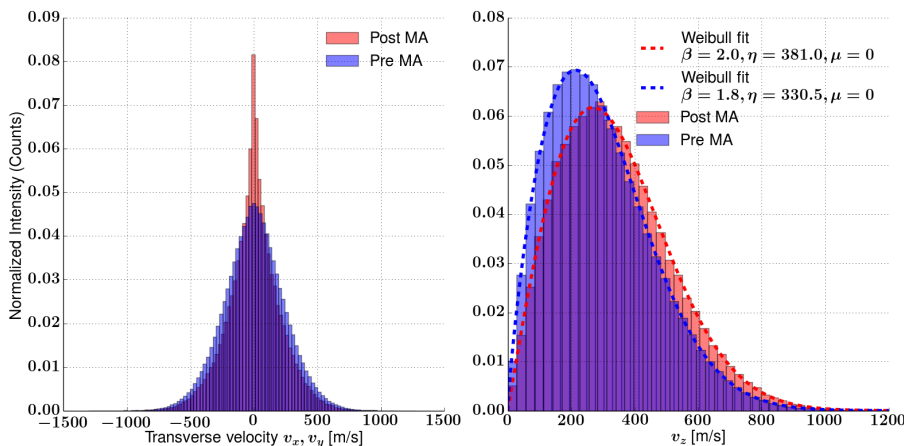


Figure 4.3: Atomic velocity distributions at the input and output of the microchannel array (MA). The left plot represents the transverse velocity $v_{x,y}$ distribution while the right plot shows the v_z distribution. The velocity distributions at the channel input are shown in blue while the distributions at the output are shown in red. The v_z distributions are fitted to Weibull distributions. The channels of the microchannel array poses stringent requirements on the escape velocity of the atoms, augmenting their chances of escape for high v_z components and low transverse velocities as a result of the frequent atom-wall collisions.

The velocity distribution of the atoms effusing from the microchannel is not directly comparable with existing experimental results as the simulation works in a "pulsed" fashion as opposed to the continuous atomic streams injected into the channels investigated in the literature. Only very few measurements of the velocity profile perpendicular to the output surface of the channels are available and none for the transverse velocity profile [22]. Theoretical analysis of the angular distribution $\theta = \arctan\left(\frac{v_x}{v_z}\right)$, the angle the atomic speed-vector makes with the normal to the output surface of the channel, is however available.

The theoretical distribution is derived for a continuous stream of atoms entering the channel by assuming a linear atom-wall collision rate along its

length [16]. The angular distribution includes contributions from the source (atoms that pass through without striking any walls) and from the walls if $\tan(\theta) \leq 2r/L$ where r and L are the tube radius and length, respectively. For $\tan(\theta) \geq 2r/L$, we only have wall contributions. Based on simple geometric considerations and using the abbreviation $q = (\frac{L}{2r}) \tan(\theta)$ and $\beta = \frac{2r}{L}$, the author of [38] derived the angular distribution at the output of a channel with dimension β as,

$$I(\theta) = \frac{\nu_0}{\pi} \sigma j(\theta) \quad (4.10)$$

where ν_0 is the rate at which atoms in the gas reservoir enter a unit area of the orifice, $\sigma = \pi r^2$ is the area of the tube cross section and $j(\theta)$ is the angular dependence given by,

$$j(\theta) = \alpha \cos \theta + \frac{2}{\pi} \cos \theta \left[(1 - \alpha) R(q) + \frac{2}{3q} (1 - 2\alpha) (1 - (1 - q)^{3/2}) \right] \quad (4.11)$$

for $q \leq 1$ and,

$$j(\theta) = \alpha \cos \theta + \frac{4}{3\pi q} (1 - 2\alpha) \cos \theta \quad (4.12)$$

for $q \geq 1$. Here, $R(q) = \arccos q - q(1 - 1^2)^{1/2}$ and

$$\alpha = \frac{1}{2} - \frac{1}{3\beta^2} \left(\frac{1 - 2\beta^2 + (2\beta^2 - 1)(1 + \beta^2)^{1/2}}{(1 + \beta^2)^{1/2} - \beta^2 \sinh^{-1}(\frac{1}{\beta})} \right) \quad (4.13)$$

The theoretically derived angular distribution is plotted in figure 4.4 alongside the angular distribution for all atoms and for the atoms with low propagation time $t_{\text{propagation}}$, obtained through simulation. All the distributions in figure 4.4 are normalized so that their maximum is 1. The broadening of the simulated distribution of all atoms is attributed to the "pulsed" working fashion of the simulation. This causes a large amount of slow atoms to bounce many times before escaping the channel, hereby reducing the restriction on the velocity of the escaping atoms as they bounce closer to the output. In the steady-state continuous flow of atoms through the channel, the angular distribution is dominated by atoms with high v_z and low $v_{x,y}$ and thus a low propagation time $t_{\text{propagation}}$ through the channel. The discrepancy in the tails between the dark blue histogram and the red curve is attributed to the fast atoms in the simulation, that exit the channel after bouncing few times near the exit, reducing the restriction on the escape velocity and producing initially fast atoms escaping with high $v_{x,y}$ and low v_z .

As the theoretical angular distribution was derived based on the same assumptions as the expression for the transmission probability, which is consistent with our simulations, the velocity distributions obtained through simulations are relevant. To test the robustness of the simulation, the transmission probability was computed for channels of different length to diameter ratios. Theoretically, the transmission probability of long cylindrical tubes can be approximated by $TP = \frac{8r}{3l} (1 + \frac{8r}{3l})^{-1}$ [22].

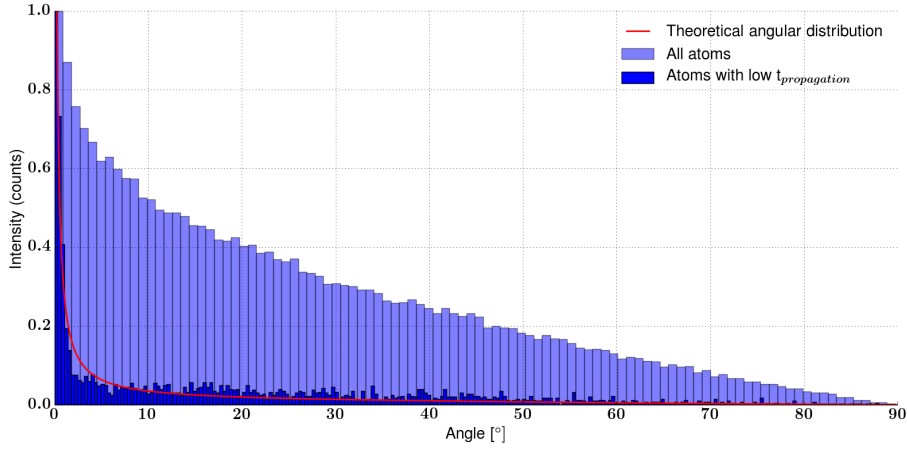


Figure 4.4: Theoretical and simulated angular distribution $\theta = \arctan\left(\frac{v_x}{v_z}\right)$ of the atoms effusing from a microchannel of the relevant dimensions. The simulated distribution is shown for all atoms and for atoms with low propagation time through the channel to more appropriately compare the 'pulsed' fashion of the simulations with the theoretical steady-state flow description. The distributions are normalized so that their maximum is at 1 to ease comparison.

A comparison between the simulated and theoretical results is shown in figure 4.5. As displayed, the simulation TP follows the theoretical prediction until the ratio $\frac{2r}{l}$ approaches 1, where the 'long channel' approximation does not hold any more.

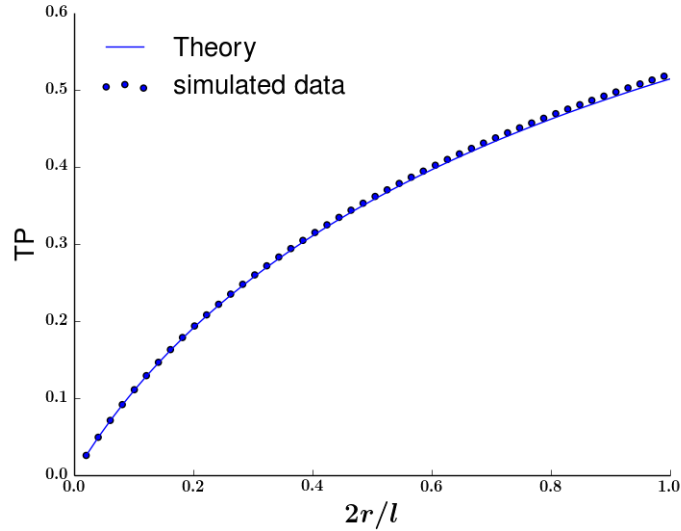


Figure 4.5: Simulated and theoretical transmission probabilities for cylindrical tubes of different length to diameter ratios.

4.2 Simulated Optical Molasses

The optical molasses technique is widely used in many optics experiments in order to collimate an atomic beam, decreasing the transverse velocity of the atoms composing it. The technique is used in our beamline, right after the oven, to increase the amount of atoms propagating through the beamline. As investigated in section 2.3.1, the optical molasses consists of using two pairs of counter-propagating laser beams, both pairs being orthogonal to each other and to the atomic beam propagation direction. In this section, we investigate the dependency of the collimation efficiency of the optical molasses technique on the laser beam power, detuning, and shape. The optimal parameters for our setup are then presented.

The atomic beam is subjected to the optical molasses directly after effusing from the microchannel array. A schematic drawing of the optical molasses technique and the atomic beam path through the geometry is shown in figure 4.6a. In practice, all lasers used for molasses are derived from the same laser and the counter-propagating beams are created by reflecting the atomic beam off a mirror. The saturation intensity of the atomic transition is much larger than the intensity of the simulated laser beams $I_{sat} \gg I_{laser}$. We can thus assume that the reflected laser beam power is unchanged after one round trip through the atomic beam. Each counter-propagating laser beam pair is assumed to be perfectly aligned and perfectly orthogonal to the other beam pair. Additionally, the laser beams are assumed to be perfectly collimated, meaning the beam radius does not change over the width of the atomic beam.

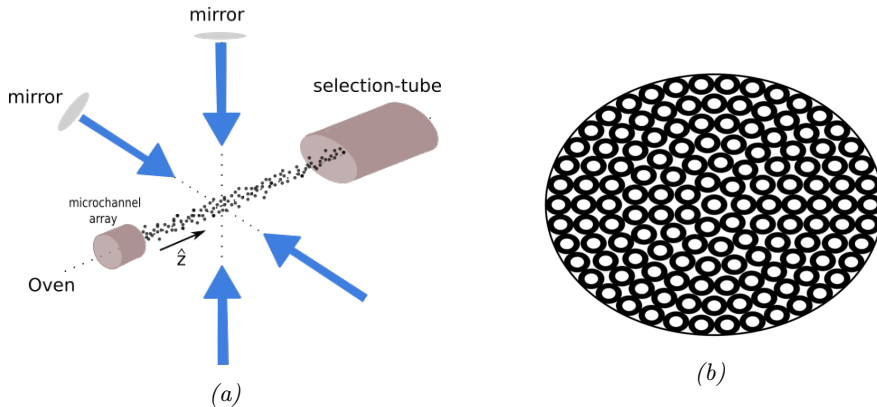


Figure 4.6: a) Schematic of the geometry of the optical molasses zone. The atoms effuse out of the microchannel array and are subjected to the optical molasses beams before entering an output-tube leading to the rest of the beamline. Each laser beam double passes the atomic beam by reflecting off a mirror. b) Geometrical Layout of the microchannel array. 136 channels of length $l = 8$ mm and inner radius $r_{inner} = 0.075$ mm are densely packed within a cylinder of radius $r_{cylinder} = 4$ mm. Each channel has a outer layer of radius $r_{outer} = 0.3$ mm.

The layout of the microchannel array is now relevant as the position of the atoms will be dependent on which channel they enter from the oven. The position of the atoms at the output of the channel through which they were prop-

agated is uniformly distributed amongst the 136 channels of the microchannel array. The geometry of the array is shown in figure 4.6b.

The transmission probability is computed as the ratio of atoms reaching the selection-tube to the amount leaving the microchannel array,

$TP = \frac{\text{Atoms at selection-tube}}{\text{Atoms leaving the microchannel array}}$. The latter is a good estimate of the efficiency of the optical molasses as the amount of atoms reaching the selection-tube is directly related to the atomic transverse velocity distribution and thus the collimation of the atomic beam.

To determine the optimal beam power and detuning of the optical molasses beams, the efficiency of the optical molasses technique for non-physical laser beams with uniform intensity distribution was investigated. The beam diameter is set to be equal to the diameter of the windows through which the optical molasses laser are sent, sealing the vacuum interior of the beam line from the outside atmosphere.

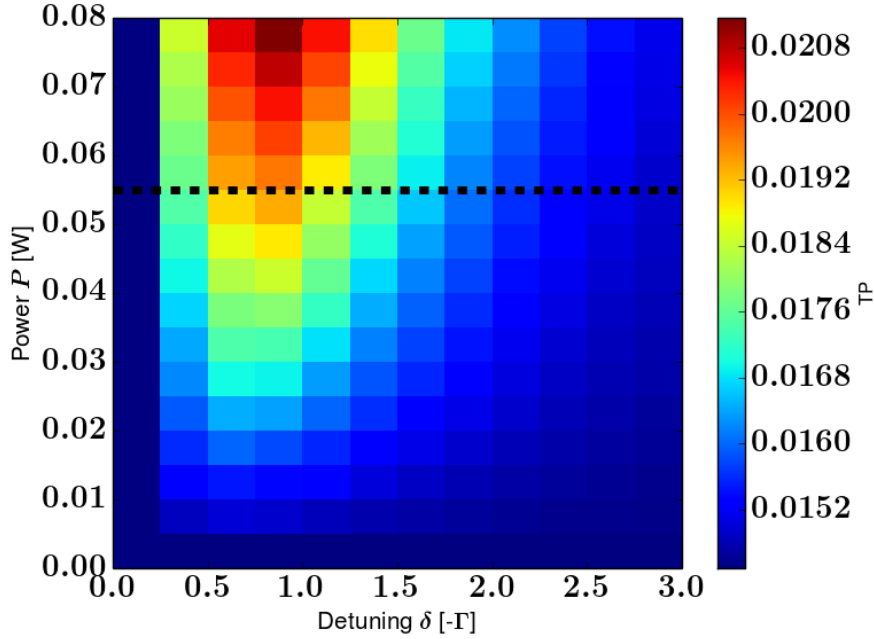


Figure 4.7: Transmission probability of the optical molasses zone for laser beams with uniform intensity profile as function of the power P and detuning δ . The detuning δ is in units of the atomic transition linewidth in radians $\Gamma = 2\pi\gamma$, where γ is the transition linewidth in Hz. Optimal detuning is found to be at $\delta_{\text{optimal}} = -\frac{3}{4}\Gamma = -\frac{3}{2}\pi\gamma$. The transmission probability increases as the power increases. The horizontal dashed black line at $P = 50$ mW represents the realistic maximum power deliverable for optical molasses in the laboratory if all the light from a Slave laser is used for this purpose. The case where $P = 0$ mW corresponds to the absence of laser beams. In this case, the transmission probability is $TP_{P=0} \approx 0.014$. For the best experimentally realistic parameters, the transmission probability is $TP_{\text{best}} \approx 0.019$.

The transmission probability of the optical molasses zone as function of the laser beam detuning $\delta = \omega - \omega_0$ and power P is shown in figure 4.7. The optimal detuning is found to be $\delta_{optimal} = -\frac{3}{4}\Gamma$. As high laser beam powers result in high transmission probability, an injection locked slave laser, expected of producing up to 120 mW of power, could be used solely for operating the optical molasses cooling. Assuming power losses due to transport from the laser output to the molasses zone, we place an upper bound of $P_{deliverable} = 100$ mW on the realistically usable laser power produce by the Slave laser. This results in an experimentally realistic 50 mW of power for each laser beam pair as delimited by the dashed black line in figure 4.7. For laser beams with optimal detuning $\delta_{optimal}$ and realistic power $P = 50$ mW, the transmission probability is $TP_{best} \approx 0.019$. The TP of the molasses zone without any laser beam is represented on figure 4.7 by laser beams of power $P = 0$. In this case, the transmission probability is $TP_{P=0} \approx 0.014$.

While the effort invested for the minuscule gain in TP obtained from having no beams to the best possible laser beam as optical molasses might seems to be a waist of efforts, it results in significantly colder atoms at the selection-tube input as displayed in figure 4.8. As the laser beams are assumed perfectly orthogonal to the atomic beam in the simulation, the atomic velocities along the z -axis remain unchanged.

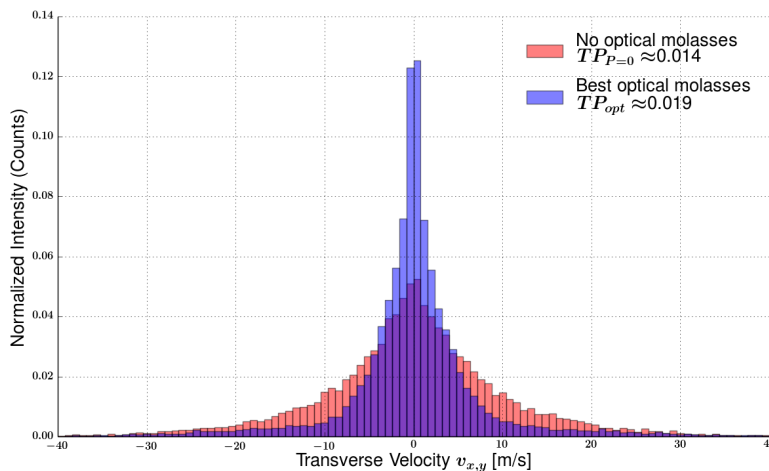


Figure 4.8: Transverse velocity distribution of the atoms at the selection-tube input area with and without optical molasses. The blue histogram represents the transverse velocity distribution for optical molasses laser beams of uniform intensity, optimal detuning $\delta = -\frac{3}{4}\Gamma$ and power $P = 50$ mW. The red histogram is the atomic transverse velocity distribution at the same location but when no optical molasses were used. The overlap between the two distributions is shown in purple. The area of the distributions have been normalized to 1.

The sharp tails of the blue distribution are attributed to the atoms that were little or not at all affected by the laser beams due to their high transverse velocity $v_{x,y}$, but still managed to enter the selection-tube due to their large v_z component.

The uniform distribution of the laser beam intensities used in the simulations above, additionally to being unphysical, leads to an inefficient power distribution as atoms with a position outside of the selection-tube entrance area will be affected by laser power in vain since their trajectory cannot be bent to more than asymptotically parallel to the z -axis. The efficiency of the optical molasses was thus tested for other, more efficient and experimentally realistic laser beam intensity profiles which hopefully concentrate the light more adequately for cooling the atomic beam. These intensity profiles are Gaussian and elliptic.

For each beam, the Gaussian beam intensity profile for is given by

$$I_{Gaussian} = \frac{P}{2\pi\sigma^2} e^{-\left[\frac{(z-\mu)^2+d^2}{2\sigma^2}\right]} \quad (4.14)$$

where σ is the variance of the beam and z is the position along the atomic beam propagation direction. $d = x, y$ is the position along the axis orthogonal to both z and the laser beam propagation direction, P is the laser beam power and μ is the beam center displacement from $z = 0$. It is envisioned that the Gaussian profile is most efficient close to the microchannel array output, where it can cool the atoms efficiently before they diverge too much and are lost. The displacement μ , of the Gaussian profile is thus an important parameter, effectively maximizing the atoms' exposure time to the laser beams and the amount of atoms interacted with.

The elliptical intensity profile is a variation of the Gaussian profile, breaking the symmetry in the cross sectional area of the beam profile, allowing different variances in both dimensions. The elliptic intensity profile is given by,

$$I_{elliptic} = \frac{P}{2\pi\sigma_z\sigma_d} e^{-\frac{z^2}{2\sigma_z^2}} e^{-\frac{d^2}{2\sigma_d^2}} \quad (4.15)$$

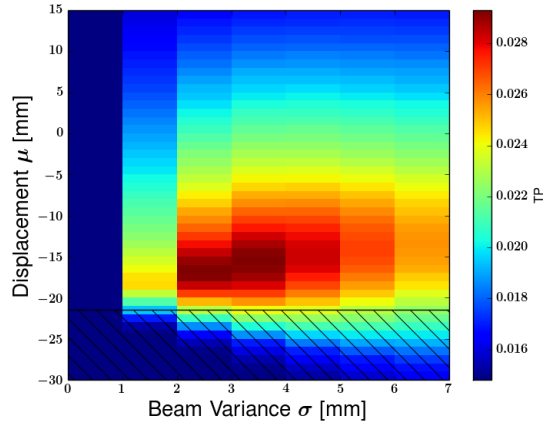
where z and σ_z are, respectively, the distance and beam variance along the z -axis, d and σ_d are, respectively, the distance and beam variance in the direction orthogonal to both the laser beam propagation direction and the z -axis. Unlike the Gaussian profile, the elliptic profile was not given an displacement parameter μ in order to reduce computational time. In practice, it is easier to optimize the beam displacement than the beam shape. Information about the beam shape is thus more relevant. Furthermore, it is expected that the displacement of the elliptic beam shape will have a less drastic effect on the TP than in the Gaussian case.

The variance σ , for both profiles, is related to the Full Width at Half Maximum (FWHM) and spot size diameter w through $FWHM = 2(2\ln(2))^{\frac{1}{2}}\sigma = (2\ln(2))^{\frac{1}{2}}w$ [34].

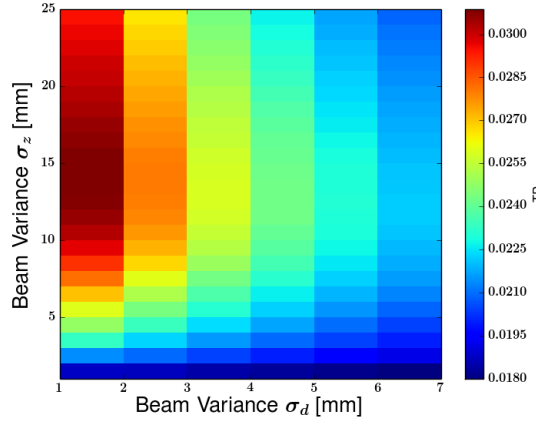
The efficiency of both laser beam shapes on the atomic collimation was investigated. For the Gaussian beam, the transmission probability was computed for different beam variances σ and displacement μ from the center of the optical molasses zone. A negative displacement μ means that the center of the Gaussian intensity profile is shifted closer to the microchannel array output. For the elliptic beam, the transmission probability was computed for different variances

σ_z and σ_d . In both cases, the beam power was set to $P_{opt} = 50$ mW and the detuning to $\delta_{opt} = -\frac{3}{4}\Gamma$. The results are shown in figure 4.9.

As can be seen 4.9 the use of the Gaussian and elliptical intensity profiles for the optical molasses laser beams results in an increase in transmission probability. As expected, the transmission probability benefits greatly from the Gaussian intensity profile being displaced close to the microchannel array. The hatched area of figure 4.9a marks the z -position of the microchannel array.



(a)



(b)

Figure 4.9: a) Transmission probability of the optical molasses zone of an atomic beam subjected to optical molasses laser beams with a Gaussian intensity profile of different displacement μ and variance σ . The horizontal hatched area delimits the z -position of the microchannel array. The best Gaussian intensity profile results in a $TP_{optimal\ Gaussian} \approx 0.029$. b) Transmission probability of the optical molasses zone of an atomic beam subjected to optical molasses laser beams with an elliptic intensity profile of varying variances σ_z and σ_d . The best elliptic intensity profile results in $TP_{optimal\ elliptic} \approx 0.030$.

As can be seen, displacements too close to the microchannel array output lead to a drop in TP due to laser power being distributed onto the channels, thus not interacting with the atoms. The TP is biggest for beam variances σ around the microchannel array radius $r_{MA} = 2$ mm. This result was also obtained by [20] where the optimal laser beam spotsize was shown to be linearly dependent on the size of the oven aperture. For the most optimal parameter-set, transmission probabilities of $TP_{\text{optimal Gaussian}} = 0.029$ are obtained.

In the case of an elliptical intensity profile, the ideal variance σ_z is a little shorter than half the length of the molasses zone. In practice, this means that the beam will be very elongated and will span the whole length of the molasses zone. This effectively maximizes the atom-light interaction time. The σ_d variance however has to be small to achieve higher transmission probabilities. A beam with variance $\sigma_d = 1$ mm corresponds to a beam diameter of about 4 mm, spanning the whole diameter of the microchannel array $d_{MA} = 4$ mm, thus containing most effusing atoms within its shape. It can be seen that the transmission probability is less sensitive to changes in σ_z than changes in σ_d . For the most optimal parameter-set, transmission probabilities of $TP_{\text{optimal elliptic}} = 0.030$ are obtained.

Despite the minuscule TP gain obtained by using the elliptic profile instead of the Gaussian profile, it results in considerably colder atoms. The transverse velocity distribution of the atoms at the selection-tube entrance for the best Gaussian, elliptic and uniform optical molasses laser beam intensity profiles are shown in figure 4.10.

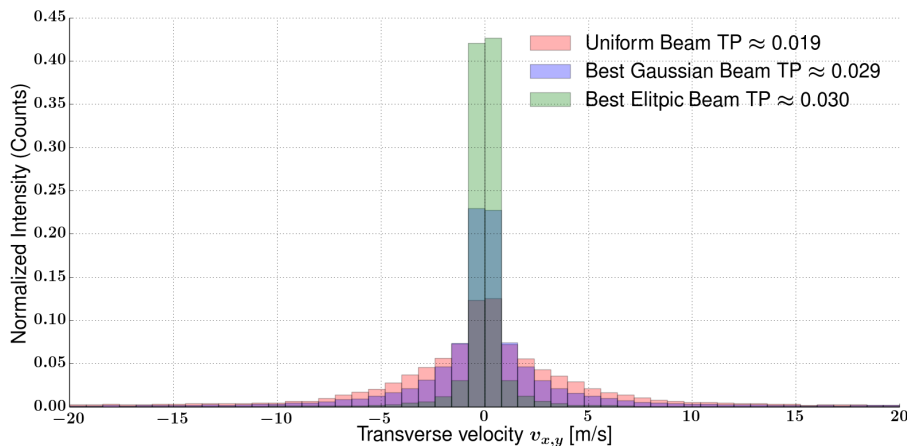


Figure 4.10: Comparison of the transverse velocity distribution of the atomic beam at the selection-tube entrance when subjected to the three optical molasses laser beam intensity profiles investigated. The laser beam parameters are optimized in light of the previous results. The green distribution represents the distribution for the elliptic intensity profile, the blue distribution is for the Gaussian profile and the red is for the uniform profile. The purple area is the overlap of the red and blue distributions and the dark green area is where all distribution overlap. The distributions are normalized so that their area is 1.

In conclusion, the elliptic laser beam intensity profile minimizes power loss and maximizes the atom-light exposure time due to its long and elongated shape. In light of the conducted simulations, the best parameters describing the detuning and intensity profile of the optical molasses laser beams are shown in table 4.1. The power P should be as high as possible.

Detuning δ	$\delta = -\frac{3}{4}\Gamma$
Beam variance	$\sigma_d = 1 \text{ mm}, \sigma_z = 13 \text{ mm}$

Table 4.1: Optimal parameters for optical molasses beams. As investigated in this section, the optimal beam shape is elliptic, possessing a beam diameter of $4\sigma_d = 4\text{mm}$, covering the whole of the microchannel array container cylinder. In the x -axis, it is very elongated to maximize interaction time with the atomic beam. The power P should be as high as possible while the optimal detuning is $\delta = -\frac{3}{4}\Gamma$.

4.3 Oven Efficiency Comparison

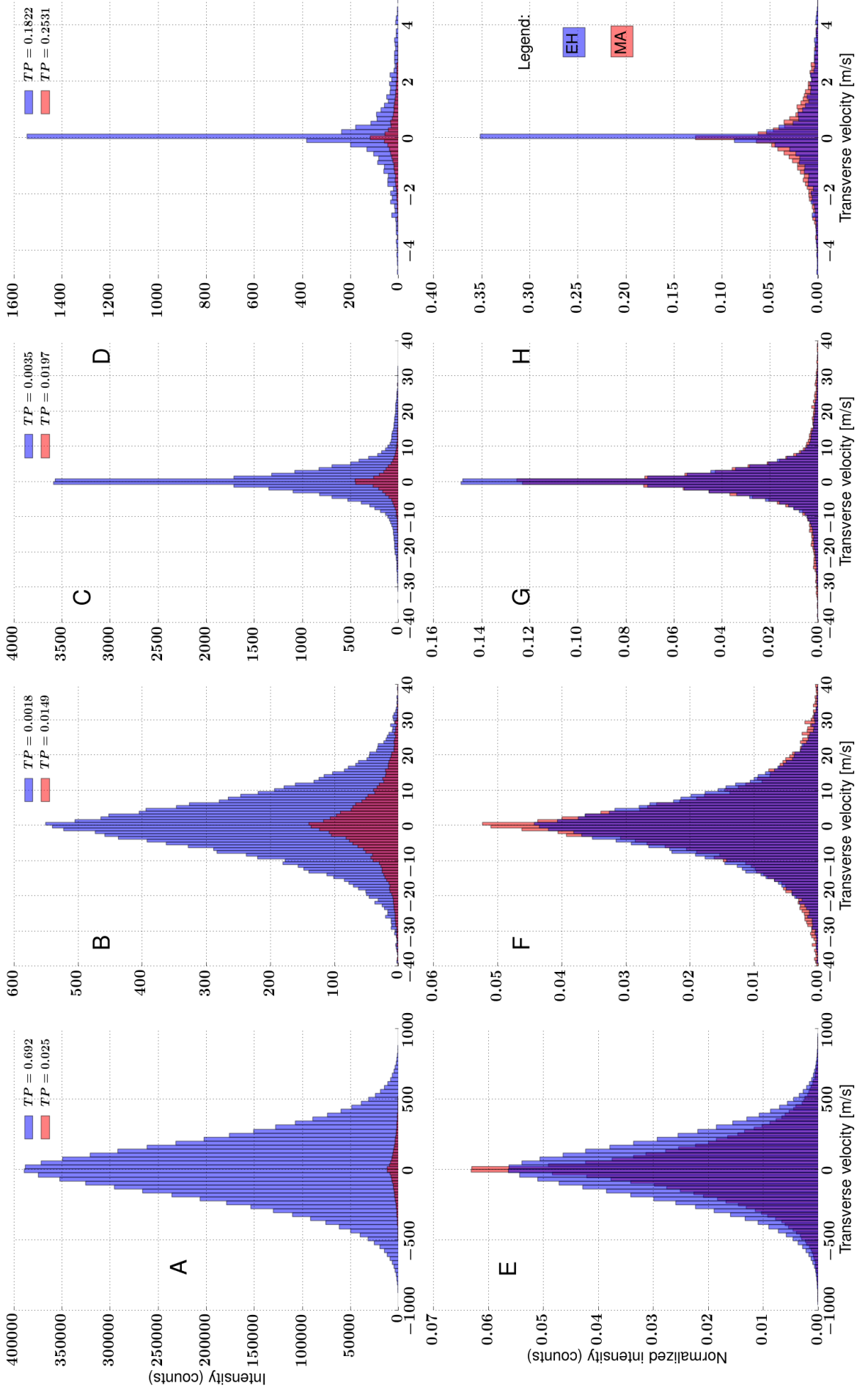
In this section, we investigate the efficiency of the use of the microchannel array (MA) as effusion mean from the oven as opposed to the exhaust hole (EH) used in an earlier version of the current setup. The EH is a short cylindrical tube of radius $r_{\text{EH}} = 2 \text{ mm}$ and length $l_{\text{EH}} = 1 \text{ mm}$. Compared with the shorter radii of $r = 0.075 \text{ mm}$ and longer channels of $l = 8 \text{ mm}$ of the channels composing the MA, the use of the EH is expected to cause a larger effusion flux due to the reduced amount of atom-wall collisions, reducing the likelihood of atoms being reflected back into the oven. However, based on the same grounds, the atomic beam is expected to effuse less collimated from the EH oven and contain a greater amount of different atomic velocity classes. [16] [22]

The transverse velocity profile of a large amount of atoms effusing from the MA and the EH is compared at 4 different locations on the atomic beam path: at the MA and EH output, at the selection-tube entrance with and without optical molasses and at the selection-tube output when optical molasses are used. Due to its larger input area, the atomic flux entering the EH is larger than that of the MA. In the following results, this difference is taken into account and the amount of injected atoms is scaled accordingly. The selection-tube, due to its distance to the oven, is assumed to be cold, resulting in the immediate condensation of the strontium atom reaching the tube boundary. In the simulation, atoms reaching a tube boundary are discarded.

In order to properly compare the efficiency of the oven effusion mean, a laser beam with power $P = 50 \text{ mW}$, detuning $\delta = -\frac{3}{4}\Gamma$ and uniform intensity profile was used for optical molasses as the latter is less geometry dependent than the other two profiles investigated in section 4.2. The results are shown in figure 4.11. Plots A,B,C and D show the transverse velocity distributions of the atoms, exhibiting how many atoms are present within each velocity class. Plots E,F,G and H show the normalized distributions, thus representing the probability of finding an atom within each velocity class.

The MA acts as a velocity selector. Due to its geometry, the escape probability of an atom is larger for atoms having a small transverse velocity $v_{x,y}$

Figure 4.11: Effect of the use of an exhaust hole (EH) and a microchannel array (MA) on the transverse velocity profile of an atomic beam. Plots A, B, C and D are a direct representation of the amount of atoms within each velocity class. The distributions on plot E, F, G and H have their areas normalized to 1 and thus represent the probability of finding an atom within a certain velocity class. The plots in the left-most column (A, E) show the transverse velocity distribution of the atoms right out of the MA (in red) and EH (in blue). In this case, the TP is calculated as the ratio of atoms entering the MA and EH to the amount of atoms injected into them. The amount of atoms injected into the EH and MA was scaled accordingly due to their differing input areas for optimal comparison. Plots B and F represent the distribution at the selection tube when no laser beams are used on the atoms. Plots C and G represent the distribution at the selection-tube input when optical molasses with laser beams of uniform intensity profile are used. For plots B, C, F and G, the transmission probability was computed as the ratio of atoms collected at the selection tube to the amount of atoms leaving the MA and EH. Plot D and H show the velocity distribution at the selection-tube output. Here the transmission probability is computed as the ratio of amount of atoms entering the selection-tube to the amount leaving its output.



and a large v_z . The requirement on the atomic escape velocity becomes less stringent as the atoms bounce closer to the channel output. The probability for atoms to bounce on a channel-wall is high near the entrance and lower near the output. As a result, the overwhelming majority of atoms return to the oven and never make it through the microchannels. The atoms that manage to get out, however, will most likely have a large v_z component and a low transverse velocity component $v_{x,y}$. The EH sets less stringent requirements on the escape velocities of atoms as the channel is short and wide enough to allow most atoms to go through without hitting any walls, resulting in a large transmission probability and a wider atomic transverse velocity distribution. This is illustrated in the plots A and E of figure 4.11, showing the transverse velocity distributions of the atoms at the output of the MA (in red) and EH (in blue). The normalized distribution of plot E shows that the MA produces a narrower distribution if the same amount of atoms were to output the MA and the EH. Plot A shows that the distribution produced by the EH results in approximately 40 times as many atoms effusing from the oven as its TP is much higher.

The plots B and F of figure 4.11 show the transverse distribution of the atoms at the selection-tube input when no optical molasses beams are used. Plot F shows that atoms reaching the selection-tube are slightly colder when effusing from the MA. The larger tails of the red distribution are attributed to the larger dimensions of the cylinder containing the microchannels, allowing for atoms with large v_z and transverse velocities too large to be affected by the optical molasses to reach the selection-tube nonetheless. From plot F and from the transmission probability, we can see that the use of the MA results in a smaller atomic loss, out of the atoms effusing from the oven. However, as shown in plot B, the large amount of atoms effusing from the EH still results in a greater amount of cold atoms within the selection-tube, despite the greater atomic losses as seen from the transmission probability.

Plots C and G show the transverse velocity distributions of the atoms at the selection-tube input area when optical molasses are used on the atomic beam. The normalized distributions of plot G shows that the atoms are colder when the EH is used. This is attributed to the, on average, lower v_z components of the atoms produced by the EH, increasing the atom-light interaction time. The v_z velocity distribution produced by the MA and EH are shown in figure 4.12. The shown distribution only include the atoms with a relatively low transverse velocity of $v_{x,y} \leq 50m/s$ as faster atoms are considered lost between the oven and selection-tube. The diameter of the MA, being larger than the selection-tube diameter, also leads to a reduced amount of atoms within the selection-tube. It is clear from plot C of figure 4.11 that the use of the EH results in a larger amount of cold atoms within the selection-tube.

Even though the higher average v_z component of the atoms produced by the MA are less affected by the optical molasses, it might result in a larger amount of atoms propagating through the selection-tube. The atomic transverse velocity distribution at the selection-tube output is shown in plot D and H of figure 4.11. Plot H shows that the disparity between the atoms produced by the EH and MA increases even more as the atoms propagate through the selection-tube due to the EH's overall lower v_x/v_z ratio and smaller dimensions.

The larger tails of the red distribution of plot H is attributed to the atoms with exceedingly larger v_z , almost unaffected by the optical molasses, that manage to propagate through the tube nonetheless. It is clear from plot D that the amount of atoms effusing from the selection-tube greatly benefits from the use of the EH.

To conclude, the stringent velocity requirements set by the microchannel array makes it less efficient than the exhaust hole as it produces atoms with higher v_z components, reducing atom-light interaction time and the optical molasses efficiency. In addition, despite the broader transverse velocity profile of the atoms produced by the exhaust hole, it's high transmission probability ensures the abundant presence of atoms within the velocity class of interest. Furthermore, the diameter of the microchannel array, being larger than the selection-tube diameter, is detrimental as atoms effusing near its edge with low transverse velocities will be lost. The flux of atoms further down the beamline would thus greatly benefit from the use of the exhaust hole and optimizing the intensity profile of the optical molasses beam would result in a yet larger amount of cold atoms exiting the selection tube.

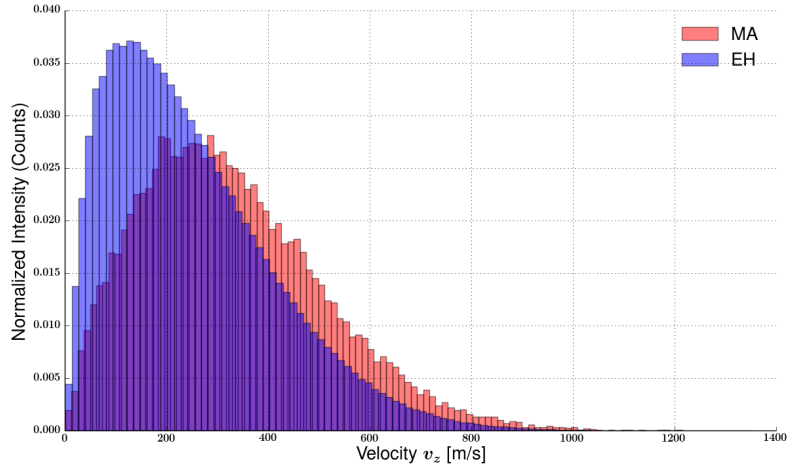


Figure 4.12: Atomic v_z velocity distribution of slow atoms effusing out of the microchannel array (MA) and exhaust hole (EH). Only the atoms with $v_{x,y} \leq 50\text{m/s}$ are used in this distribution as atoms with large transverse components are considered lost.

5 Conclusion

The work presented has been concerned with work towards the realization of a narrow linewidth laser through continuous direct spectroscopy on an ultra-narrow optical transition, thereby circumventing the fundamental limitation on the stability caused by thermal noise in a pre-stabilization.

During this project, the characterization and realization of the lasers providing the cooling light for the different cooling stages present in the final experiment have been conducted. A temperature controller was built to stabilize both the master ECDL and Slave laser mounts but, due to its under-performance under simultaneous stabilization conditions, was focused on the temperature stabilization of the master laser mount. Millidegree Celcius accuracy on the ECDL mount temperature was achieved. The ECDL was injected and awaits ultimate frequency stabilization by realization of an error signal to a reference strontium oven. The injected and frequency stabilized ECDL is expected to output over 30 mW of power, enough for injection locking of the Slave laser, realization of an error signal with the reference and for Zeeman and MOT cooling.

The oven containing an exhaust hole oven was replaced with an oven containing a microchannel array. Before the oven replacement, measurements on the transverse velocity of the atoms effusing from the old oven were performed and analyzed for future performance comparison with the new oven.

A Monte-Carlo simulation of the atomic propagation through the first few components of the beamline was developed and has provided insights into the efficiency of 2D optical molasses cooling at the oven output through the laser beam shape, detuning and power. In light of the simulation, satisfying laser cooling of the atomic beam can be attained using the totality of the expected 120 mW of light produced by the Slave laser. The simulation was also used to compare the efficiency of an exhaust hole as effusion medium from the oven present in an earlier version of the experiment, to the microchannel array, as present in the newly replaced oven. The results instructs us of the greater efficiency of the use of the exhaust hole, leading to a greater atomic collimation.

Hopefully, this project has helped narrow the bridge towards the realization of continuous direct ultra-narrow spectroscopy on cold strontium within the current beamline.

A Temperature Controller Circuitry

In this section, technical drawings of the Mount Temperature Control Circuitry are shown. This includes the Wheatstone bridge circuit and layout and the totality of the circuits present on the breadboard.

A TEMPERATURE
CONTROLLER CIRCUITRY

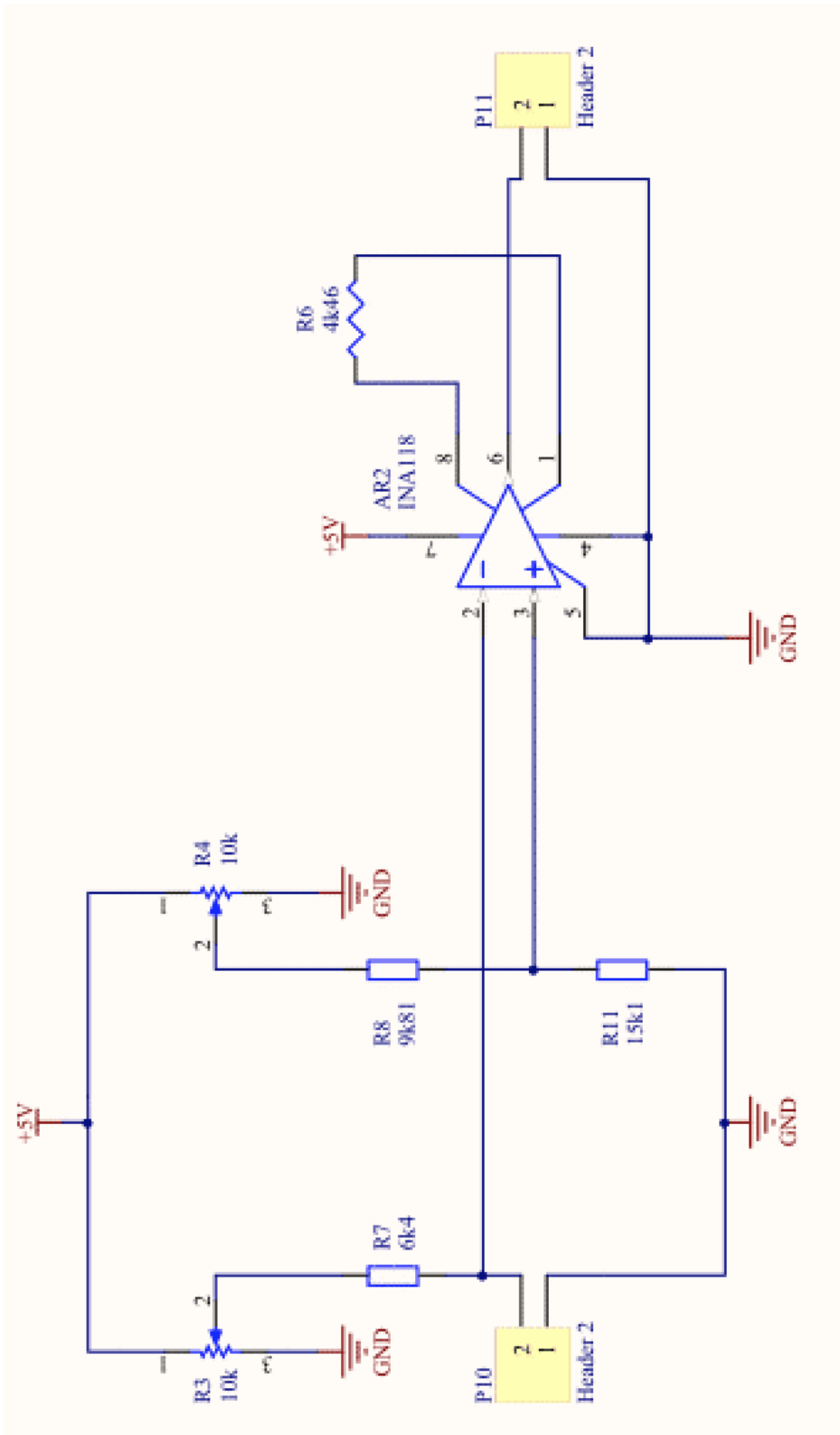


Figure A.1: Technical drawing of Wheatstonebridge circuit.

A TEMPERATURE
CONTROLLER CIRCUITRY

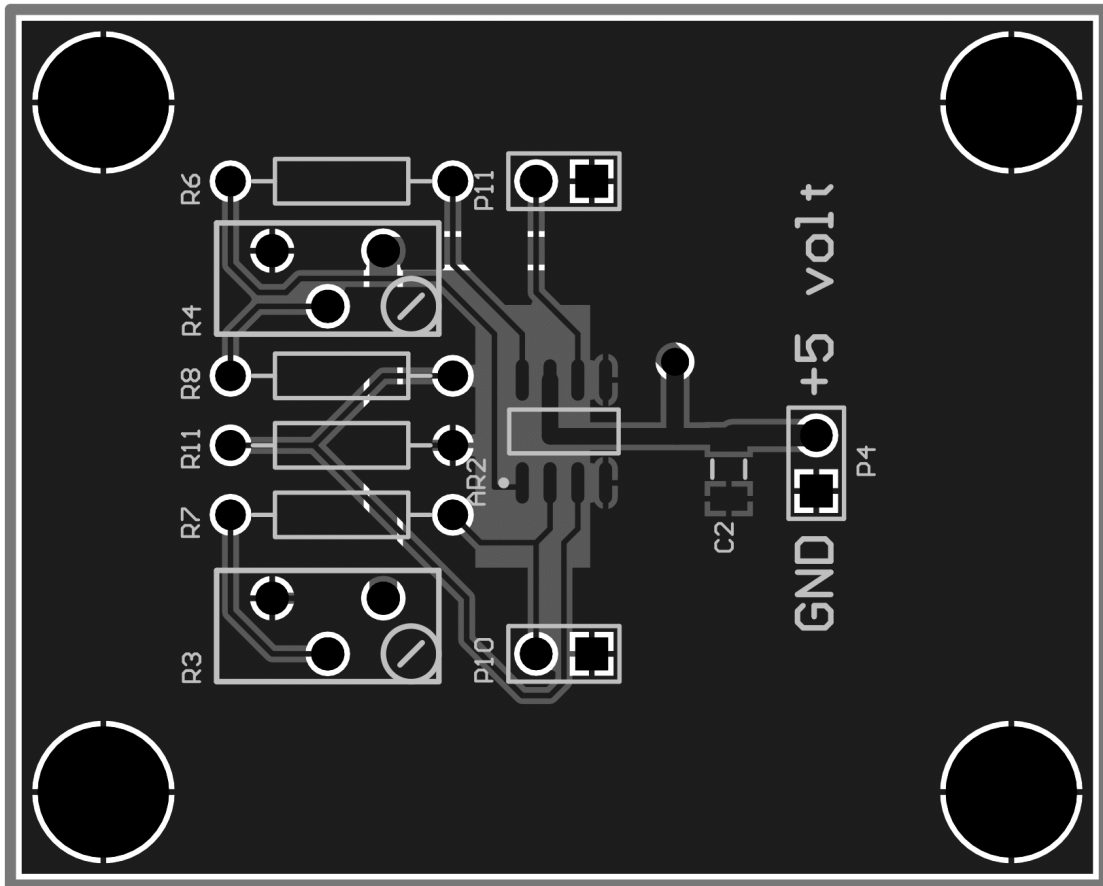


Figure A.2: Schematic drawing of Wheatstonebridge circuit.

A TEMPERATURE CONTROLLER CIRCUITRY

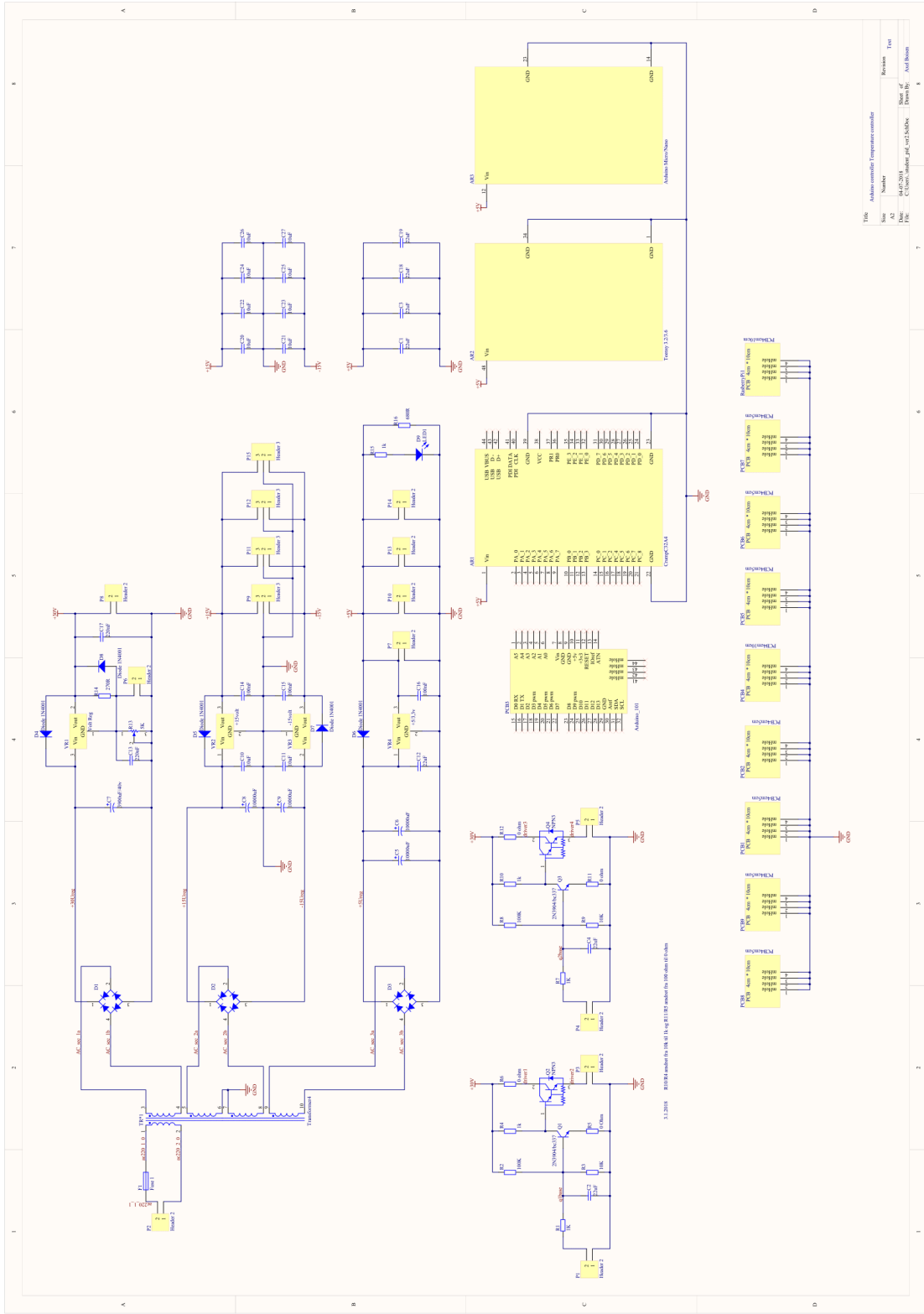


Figure A.3: Technical drawing of the breadboard circuitry. The Actuator circuit are the two identical circuits on the bottom left.

A TEMPERATURE CONTROLLER CIRCUITRY

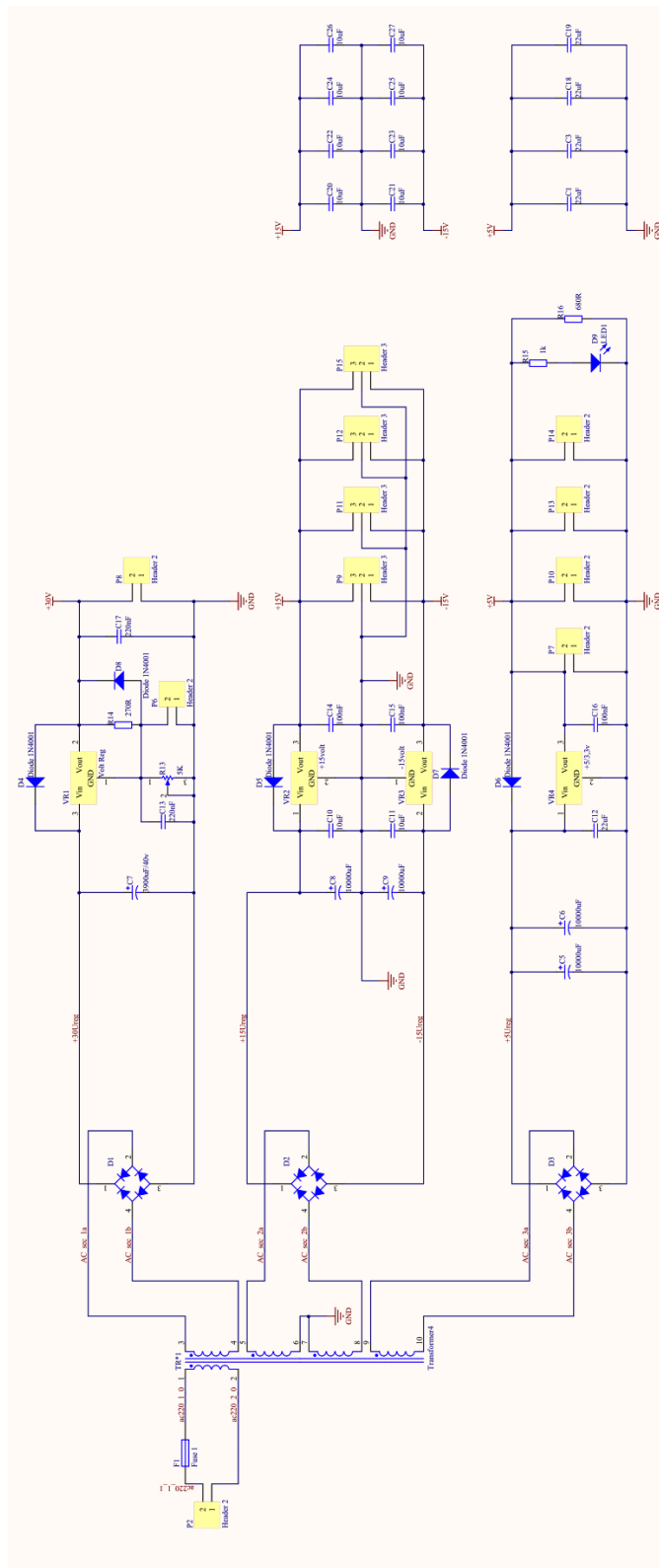


Figure A.4: Voltage supply circuitry on breadboard. The whole breadboard circuitry is shown in figure A.3.

A TEMPERATURE CONTROLLER CIRCUITRY

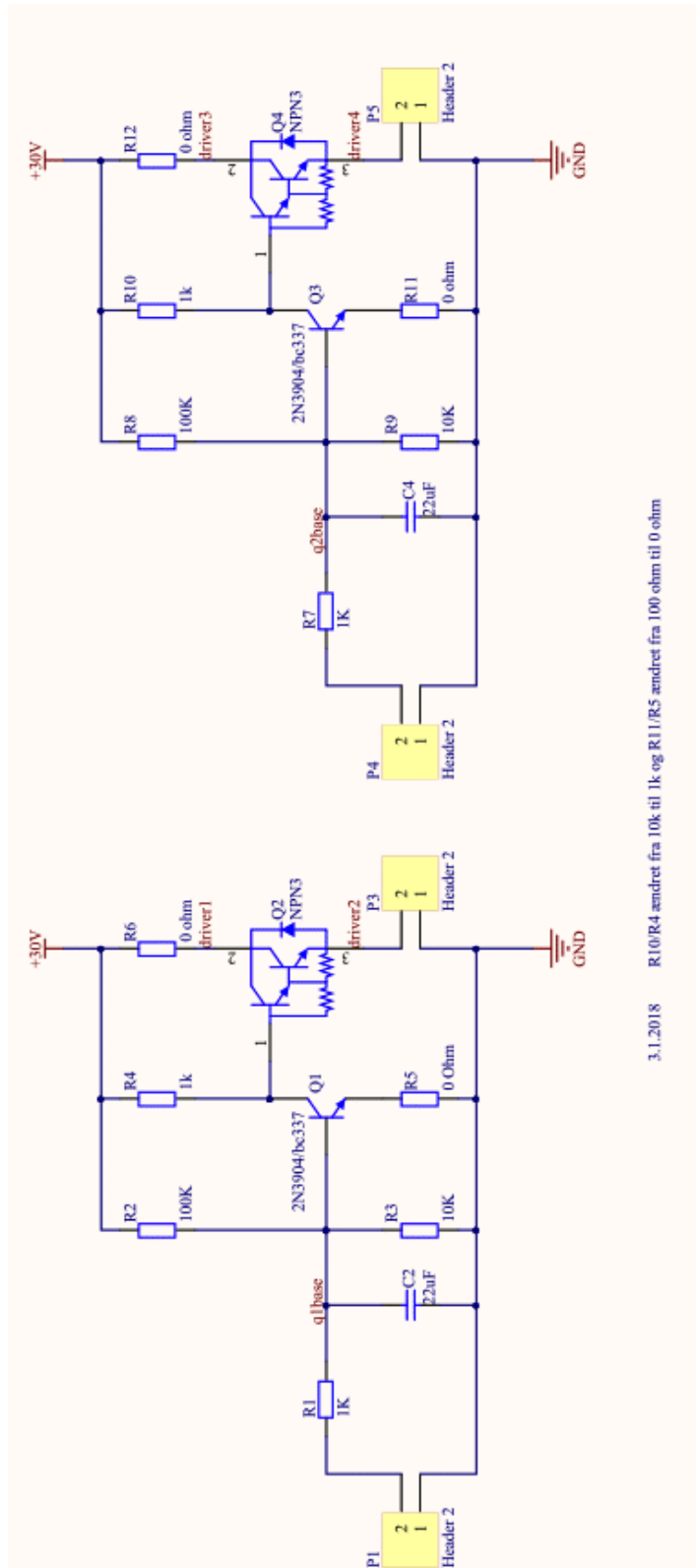


Figure A.5: Actuator circuitry on breadboard including the Low pass filter and Darlington pair. The whole breadboard circuitry is shown in figure A.3.

B Arduino

This section presents the wiring and layout of the Arduino in hope to facilitate the use of the built mount temperature controller in the future. A description of communication means with the Arduino board is also presented. The full script uploaded onto the Arduino is also presented.

B.1 Arduino Layout

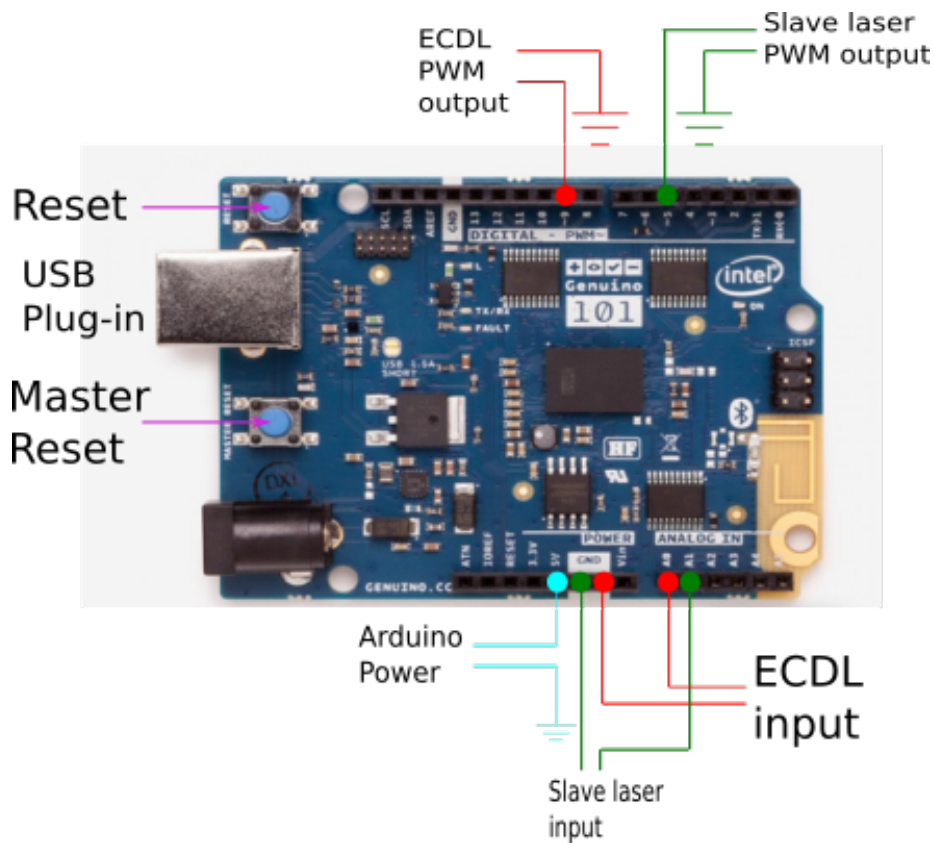


Figure B.1: Layout and wiring of the Arduino. The A0 and A1 pins are used as input pins for the ECDL (red) and Slave laser (green) Wheatstone bridge signal, measuring the temperatures of the mounts. PWM pins 9 and 5 are used as output for the software processed signal. The Arduino is powered by the power supply, with which it is mounted onto the fretboard, through its 5V pin. The reset button resets the code, while the master reset button is used to clear the board so that a new code can be uploaded onto it. The USB plug-in is used to make a serial connection with the laptop. The Arduino program can be used to write and upload a code into an Arduino board easily.

B.2 Arduino Communication

Communication with the Arduino board is effectuated by serial connection at 9600 baud through the Arduino's USB port. The open-source Integrated Development Environment (IDE) Arduino software is used for uploading code onto the board. The reset button is used to re-start the code, eliminating all computed values and variables. The Master reset button is used to clear the board from code so that new code can be uploaded. The layout of the Arduino board and locations of the Reset and Master Reset buttons is shown in figure B.1.

Multiple commands were implemented, allowing for control over the different parameters managing the Arduino and code. *ON* and *OFF* commands were implemented to separately turn the mount temperature stabilization of the ECDL and Slave laser on and off separately. A *PING* command to test the responsiveness of the code by responding *PONG*. The user is allowed control over the values of the K_P and K_I parameters and the set-point value. A command altering the delay time between each Arduino input reading was also implemented. A *SHOW* command can be used to display the different values relevant for monitoring the mount temperature stabilization. The *SHOW* command displays: *input, output, outputvalue, error, integral, delay* for the ECDL and Slave laser separated by a 'slash' symbol '/'. The *delay* is common for the ECDL and Slave laser and stands for the increased sampling rate mentioned in section 3.3.3. *input* is the Arduino input as read by the 10-bit resolution ADC. *error* is the computed value of the error as $error = \text{set-point} - \text{input}$. The *output* is the numerical value of the PI formula $output = K_P * error + K_I * (integral)$ which is then translated to an 8-bit voltage value as *outputvalue*, the Arduino output. *integral* is the numerical value of the integral part of the PI mechanism which increases with 1 each iteration $integral = integral + 1$. A list of the various commands and their effect is presented in table B.1. The parameter $\alpha = 0, 1$ refers to the communication of the part of the code controlling the temperature of the ECDL by taking the value 1 and Slave laser by taking the value 0.

Command	Effect
$\alpha ON/\alpha OFF$	Disables the part the adequate part of the code (ECDL or slave)
<i>SHOW</i>	Displays input1,output1,outputvalue1,error1,integral1,delay /input2,output2,outputvalue2,error2,integral2,delay where 1 refers to the ECDL and 2 to the Slave laser.
$\alpha SETPval$	Changes the K_P parameter of α to <i>val</i> .
$\alpha SETIval$	Changes the K_I parameter of α to <i>val</i> .
$\alpha SETDval$	Changes the delay parameter of α to <i>val</i> .
$\alpha SETSval$	Changes the set-point of α to <i>val</i> .
$\alpha PING$	Outputs <i>PONG</i> α if the code is responsive.

Table B.1: List of commands of the Arduino temperature control code. $\alpha = 1, 2$ refers to respectively the ECDL or the slave laser. *val* is an integer number with maximum 4 digits of the form 0000. After serial connection has been established, communication with the Arduino board is effectuated through these commands. By writing `ser.write('command'.encode())`. The response can be read by printing the serial line `ser.readline()`. Where *ser* is the name of the serial that has been connected.

The full script uploaded onto the Arduino is shown in the appendix. As a safeguard, the code disables the ECDL or Slave laser mount temperature control if the respective Arduino input value is higher than $3.3V$, corresponding to a mount temperature above $1^{\circ}C$ above set-point. A red Light Emitting Diode (LED) was mounted onto the front panel of the MTC box. It is set to light up when the mount temperature of the ECDL lies within approximately $1^{\circ}C$ of the set-point temperature, confirming a temperature stabilized mount.

B.3 Arduino Script

```
#define PIN_INPUT1 A0
#define PIN_INPUT2 A3
#include <string>
#include <sstream>
#include <stdlib.h>

int Setpoint1 = 504; // (1023/3.3V) * 1.62V = 504
int Setpoint2 = 508; // (1023/3.3V) * 1.64V = 508
int delayval = 10; // delay value
int input1, input2, Output1, Output2, Error1, Error2;

int Kp1=3000, Ki1=30, Kd1=0;
int Kp2=100, Ki2=100, Kd2=0;
int Ki = 0;
int previous_error1 = 0, integral1 = 0, derivative1;
int previous_error2 = 0, integral2 = 0, derivative2;
int integral_count1 = 0, integral_count2 = 0;
int integral_count_reset_val1 = 150000, integral_count_reset_val2 = 350000;

int outputPin1 = 9;
int outputPin2 = 3;
int LEDpin = 4;

int OutputValue1;
int OutputValue2;

bool ON1 = true; // run the loop (ON/OFF) parram
bool ON2 = false;

String inistr;
String teststr;
String testval;
String num;

void setup() {

    // initialize serial communication at 9600 bits per second:
    Serial.begin(9600);

    pinMode(A0, INPUT);
    pinMode(A3, INPUT);

    digitalWrite(A0, HIGH);
    digitalWrite(A3, HIGH);

    pinMode(outputPin1, OUTPUT);
    pinMode(outputPin2, OUTPUT);
    pinMode(LEDpin, OUTPUT);
```

```

}

void loop() {
  /* Serial */
  /* COMMANDS
   * SHOW - displays
   input/output/OutputValue/Error/integral/integral_count for both diode
   *
   * Specify the diode to be controlled with a number (1 for ECDL and 2
   for slave) in front
   * of each command (e.g 10N for turning on the ECDL temperature
   control)
   *
   * List of diode sensitive commands:
   * ON/OFF starts or puts and end to the script
   *
   * SETP0000, SETI0000, SETD0000, SETS0000, SETC0000
   * sets new value for P,I,Delay - parameter, the setpoint S
   * or the integral_count_reset_val C, respectively, to 0000, the
   number entered (max 9999).
   * In the case of SETC0000, the value 0000 is automatically multiplied
   by 1000 in the code.
   * (e.g 1SETP1000 sets the P-parammeter value of the ECDL to 1000).
   *
   * PING - arduino answers PONG
   */

  if (Serial.available() > 0) {

    inistr = Serial.readString();
    num = inistr[0];
    teststr = inistr[1];
    teststr.concat(inistr[2]);

    if (teststr == "ON") { //Turn PID code On
      if (num == "1") {
        ON1 = true;
        Serial.println("script1 started");
        //integral_count1 = 0;
        //integral1 = 0;
      }
      else if (num == "2") {
        ON2 = true;
        Serial.println("script2 started");
        //integral_count2 = 0;d
        //integral2 = 0;
      }
    }
  }
}

```

```

}
else if (num == "S") {

    Serial.print(input1); Serial.print(" , ");
    Serial.print(Output1); Serial.print(" , ");
    Serial.print(OutputValue1); Serial.print(" , ");
    Serial.print(Error1); Serial.print(" , ");
    Serial.print(integral1); Serial.print(" , ");
    Serial.print(delayval); Serial.print(" / ");

    Serial.print(input2); Serial.print(" , ");
    Serial.print(Output2); Serial.print(" , ");
    Serial.print(OutputValue2); Serial.print(" , ");
    Serial.print(Error2); Serial.print(" , ");
    Serial.print(integral2); Serial.print(" , ");
    Serial.println(delayval);
}
else if (teststr == "OF") { //Turn PID code Off

    if (num == "1") {
        ON1 = false;
        Serial.println("script1 terminated");
        //integral_count1 = 0;
        //integral1 = 0;
    }
    else if (num == "2") {
        ON2 = false;
        Serial.println("script2 terminated");
        //integral_count2 = 0;
        //integral2 = 0;
    }
}
else if (teststr == "SE") {
teststr = inistr[4];
testval = inistr[5];
testval.concat(inistr[6]);
testval.concat(inistr[7]);
testval.concat(inistr[8]);

    if (teststr == "P") {

        if (num == "1") {
            Kp1 = atoi(testval.c_str()); // string to int
            Serial.print("P1 value changed to ");
            Serial.println(Kp1);
        }

        else if (num == "2") {

```

```
        Kp2 = atoi(testval.c_str()); // string to int
        Serial.print("P2 value changed to ");
        Serial.println(Kp2);
    }
}
else if (teststr == "I") {

    if (num == "1") {
        Ki1 = atoi(testval.c_str()); // string to int
        Serial.print("I1 value changed to ");
        Serial.println(Ki1);
    }
    else if (num == "2") {
        Ki2 = atoi(testval.c_str()); // string to int
        Serial.print("I2 value changed to ");
        Serial.println(Ki2);
    }
}
else if (teststr == "D") {

    if (num == "1") {
        delayval = atoi(testval.c_str()); // string to int
        Serial.print("Delay value changed to ");
        Serial.println(delayval);
    }
    else if (num == "2") {
        Kd2 = atoi(testval.c_str()); // string to int
        Serial.print("D2 value changed to ");
        Serial.println(Kd2);
    }
}
else if (teststr == "C") {

    if (num == "1") {
        integral_count_reset_val1 = atoi(testval.c_str())*1000;
        Serial.print("integral_count_reset_val1 changed to ");
        Serial.println(integral_count_reset_val1);
    }
    else if (num == "2") {
        integral_count_reset_val2 = atoi(testval.c_str())*1000;
        Serial.print("integral_count_reset_val2 changed to ");
        Serial.println(integral_count_reset_val2);
    }
}
}
else if (teststr == "S"){

    if (num == "1") {
```

```

        Setpoint1 = atoi(testval.c_str());
        Serial.print("Setpoint1 value changed to ");
        Serial.println(Setpoint1);
    }
    else if (num == "2") {
        Setpoint2 = atoi(testval.c_str());
        Serial.print("Setpoint2 value changed to ");
        Serial.println(Setpoint2);
    }

    }
    else {
        Serial.println("Did not recognize command");
    }
}
else if (teststr == "PI") { // PING - answers PONG
    if (num == "1") {
        Serial.println("PONG1");
    }
    else if (num == "2") {
        Serial.println("PONG2");
    }
}
else {
    Serial.println("did not recognize command");
}
}

if (ON1 || ON2) { // ON1 || ON2
    Update_PID();
}
else {
    analogWrite(outputPin2,255);
    analogWrite(outputPin1,255);
}
}

void Update_PID() {
    // Convert the analog reading (which goes from 0 - 1023) 10bit to a voltage
    (0 - 3.3V):
    //float input = analogRead(PIN_INPUT) * (3.3 / 1023.0) ; //convert analog
    input read
    input1 = analogRead(PIN_INPUT1); // input in bits
    //delay(5); //10ms
    //input1 = analogRead(PIN_INPUT1);
}

```

```

//input2 = analogRead(PIN_INPUT2); // input in bits
input2 = 0;
//***** PID CODE 1 ECDL *****//
Error1 = (Setpoint1 - input1); // Dividing the error reduces the resolution

/*
// integral count reset val method
if (integral_count1 > integral_count_reset_val1) {
integral1 = integral1 + Error1;
integral_count1 = 0;
}
*/
// minimum integrator stacking method

//Minimum stacking method
if (Error1 > 1) {integral1 = integral1 + 1;}
else {integral1 = integral1 -1;}
if (input1<490) {integral1=0;} // when hte integral starts counting to avoid
huge values and oscillations
// input < 490

/*
// Normal Stacking method
if (input1>490) {integral1 = integral1 + Error1;}
*/

Output1 = (Kp1 * Error1)/100 + (Ki1 * integral1)/100;

// ***** PID CODE 2 SLAVE *****//
Error2 = (Setpoint2 - input2);

if (integral_count2 > integral_count_reset_val2) { // reset
integral_count_reset val and update integral2
integral2 = integral2 + Error2;
integral_count2 = 0;
}

// integral2 = integral2 + Error2; //delay method
derivative2 = (Error2 - previous_error2);
Output2 = (Kp2 * Error2)/100 + (Ki2 * integral2)/100 + Kd2 * derivative2;

// ***** SETTING OUTPUTVALUES FOR ARDUINO *****//
// integral_count doesn't count if OutputValue = 0
// ***** ECDL
if (ON1) {
if (Output1 <= 0) { // input Voltage too high, need to "cool down"

```

```

        OutputValue1 = 255;
        //integral_count1++; // counting the integral_count
    }
    else if (Output1 >= 255) { // input Voltage too low, maxing out heating
        OutputValue1 = 0;
        //integral1 = 0; // for the delay implementation method
    }
    else {
        OutputValue1 = 255 - Output1;
        //integral_count1++;
    }
}

// ***** SLAVE
if (ON2) {
    if (Output2 <= 0) { // input Voltage too high, need to "cool down"
        OutputValue2 = 255;
        //integral_count2++;
    }
    else if (Output2 >= 255) { // input Voltage too low, maxing out heating
        OutputValue2 = 0;
        //integral2 = 0; // for the delay implementation method
    }
    else {
        OutputValue2 = 255 - Output2;
        //integral_count2++;
    }
}

// ***** SAFEGUARD IN CASE OF HIGH INPUT VALUE
// *****//
if (input1 >= 1000) { // Safety precaution
    ON1 = false;
    OutputValue1 = 255;
}

if (input2 >= 1000) {
    ON2 = false;
    OutputValue2 = 255;
}

// ***** WRITING TO ARDUINO AND UPDATING VALUES
// *****//
if (ON1) {
    analogWrite(outputPin1,OutputValue1);
    //analogWrite(outputPin1,0);
    //digitalWrite(LEDpin,HIGH);} // test out that LED lights up

```

```
    if (input1 < Setpoint1+6 && input1 > Setpoint1-6) { // if input1 within
range of setpoint
        digitalWrite(LEDpin,HIGH); // write to LED pin with certain value
    }
    else {
        digitalWrite(LEDpin,LOW);
    }
}
else {
    analogWrite(outputPin1, 255);
}

if (ON2) {
    //analogWrite(outputPin2,OutputValue2);
    analogWrite(outputPin2,40);
}
else {
    analogWrite(outputPin2, 255);
}

previous_error1 = Error1;
previous_error2 = Error2;

delay(delayval);
}
```

C Technical Drawings

This section contains technical drawings of the ECDL mount used in this project.

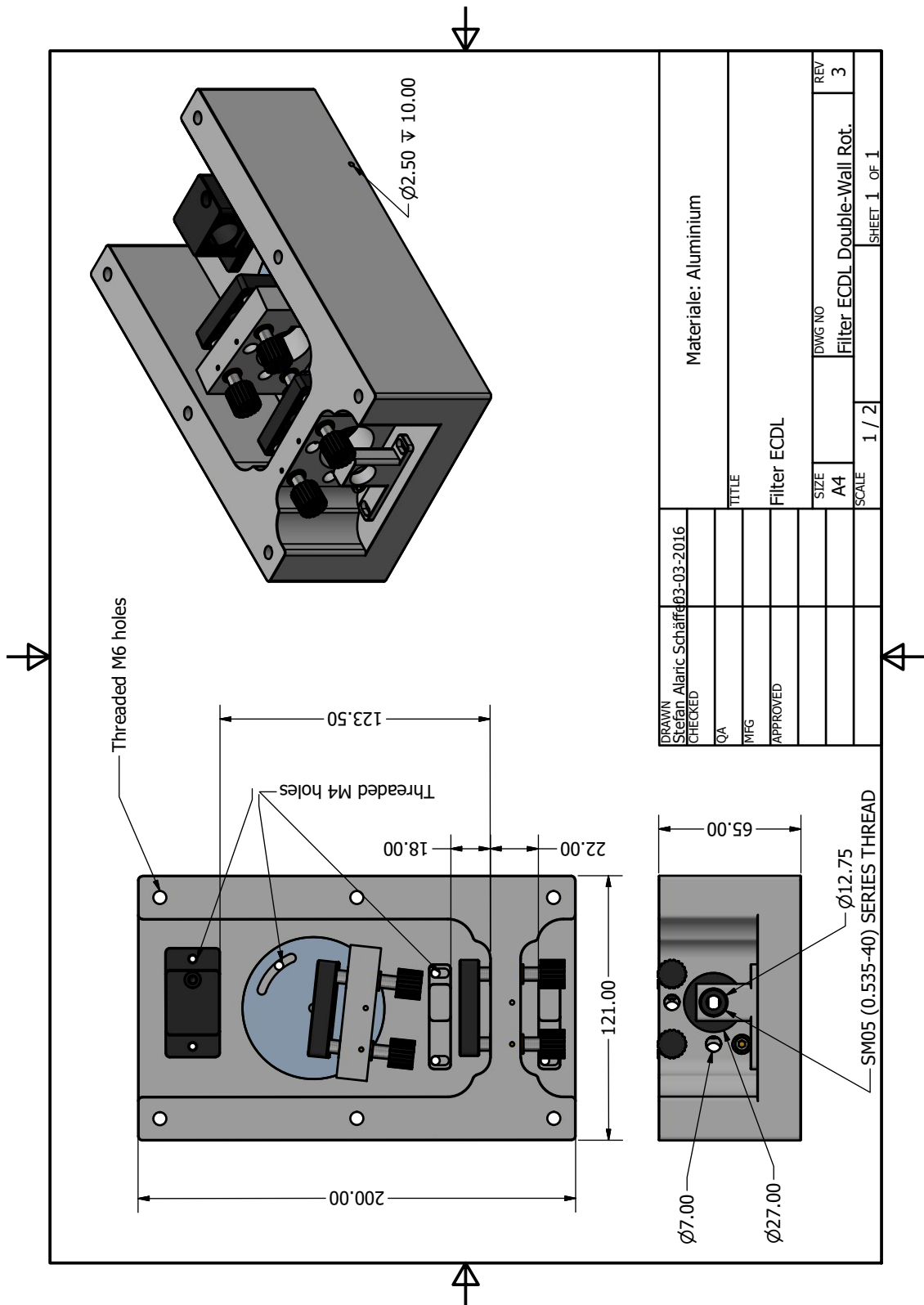


Figure C.1: Technical drawing of the ECDL copper block. All the optical elements are mounted on the block and it is also used as heating element.

Bibliography

- [1] Fritz Riehle, *Frequency Standards: Basics and Applications*, Wiley-VCH, 2004.
- [2] BIPM, *Resolution 1 of the 13th Conférence Générale des Poids et Mesures*, CGPM, 1967.
- [3] G.A. Kazakov, T. Schumm, *Active optical frequency standards using cold atoms: perspectives and challenges*, Institute of Atomic and Subatomic Physics, Vienna University of Technology, 13 march 2015.
- [4] A.D. Ludlow, X. Huang, M. Notcutt, T. Zanon-Willette, S.M. Foreman, M.M. Boyd, S. Blatt and J. Ye, *Compact Thermal-Noise-Limited Optical Cavity for Diode Laser Stabilization at 1×10^{-15}* , Opt. Lett. **32** 6, (2007), 641-643.
- [5] G.D. Cole, Z. Zhang, M.J. Martin, J. Ye and M. Aspelmeyer, *Tenfold reduction of Brownian noise in high-reflectivity optical coatings.*, Nature Photonics, DOI:10.1038/NPHOTON.2013.174, 21 July 2013.
- [6] W.M. Itano, J.C. Bergquist, J.J. Bollinger, J.M. Gilligan, D.J. Heinzen, F.L. Moore, M.G. Raizen and D.J. Wineland, *Quantum projection noise: Population fluctuations in two-level systems*, Physical Review A, vol. 47, no. 5, pp. 3554-3570, May 1993. ONLINE: <http://www.nature.com/doi/finder/10.1038/nphoton.2012.217>
- [7] G. Santarelli, P. Laurent, P. Lemonde, A. Clairon, A.G. Mann, S. Chang, A.N. Luiten and C. Salomon, *Quantum Projection Noise in an Atomic Fountain: A High Stability Cesium Frequency Standard*, Phys. Rev. Lett. **82** (1999), 4619-4622.
- [8] Courtillot, Irene (2003), *Première observation de la transition fortement interdite $1S0-2P0$ du strontium, pour une horloge optique à atomes piégés*, Université Pierre et Marie Curie, Paris.
- [9] T.L. Nicholson, M.J. Martin, J.R. Williams, B.J. Bloom, M. Bishof, M. Swallows, S. Campbell and J. Ye, *Comparison of Two Independent Sr Optical Clocks with 1×10^{-17} Stability at 10^3 s*, Phys. Rev. Lett. **109** (2012) 230801.
- [10] https://www.colorado.edu/physics/phys4510/phys4510_fa05/Chapter5.pdf
- [11] Matthew A. Norcia, Matthew N. Winchester, Julia R. K. Cline and James K. Thompson, *Superradiance on the millihertz linewidth strontium clock transition.*, October 14, 2016, Sci Adv 2016.
- [12] J. E. Sansonetti, G. Nave, *Wavelengths, transition probabilities, and energy levels for the spectrum of neutral strontium (SrI)*, Journal of Physical and Chemical Reference Data, vol. 39, no. 3, 2010.
- [13] Warren Nagourney, *Quantum Electronics for Atomic Physics and Telecommunication.*, Second Edition, Oxford University Press.
- [14] INA118 data sheet, ONLINE: <http://www.ti.com/lit/ds/symlink/ina118.pdf>
- [15] P.C.D Hobbs, *Building Electro-Optical Systems: Making It All Work*, John Wiley & Sons New York (2000), Chapter 20.
- [16] GIACINTO S.(1988). *Atomic and Molecular Beam Methods*. New York, New York Oxford University Press, Chapter 4
- [17] http://atomoptics-nas.uoregon.edu/~tbrown/files/strontium_vacuum_system/Research%20Papers/Livesey_mod.pdf

- [18] S.I PAI, *Radiation Gas Dynamics*, Springer, New York (1966)
- [19] GREENWOOD J., *The correct and incorrect generation of a cosine distribution of scattered particles for Monte-Carlo modelling of vacuum systems*, National Physical Laboratory, Centre for Mechanical and Acoustical Metrology, Queens Road, Teddington TW11 0LW, UK
- [20] SHANGYAN LI, MIN ZHOU & XINYE XU, *Analysis of atomic beam collimation by laser cooling*. Nature 2018, DOI:10.1038/s41598-018-28218-y
- [21] H. C. W. BEIJERINCK, M. P. J. M. STEVENS and N. F. VERSTER, *MONTE-CARLO CALCULATION OF MOLECULAR FLOW THROUGH A CYLINDRICAL CHANNEL*, November 1975, Physica 83C(1976) 209-219
- [22] H. C. W. Beijerinck, and N. F. Verster, *Velocity distribution and angular distribution of molecular beams from multichannel arrays*, November 1974, Journal of Applied Physics 46, 2083 (1975); doi: 10.1063/1.321845
- [23] KNUDSEN, *The Cosine Law in the kinetic theory of gases*, Translation of "Das Cosinusetz in der kinetischen Gastheorie." Annalen der Physik, Vol. 48, pp. 1113-1121, 1915.
- [24] J. FOOT, *Atomic Physics*, Oxford University Press, New York(2005)
- [25] J. BECHHOEFER, *Feedback for physicists: A tutorial essay on control*, Department of Physics, Simon Fraser University, Burnaby Canada, 31 August 2005.
- [26] S.A.Schaffer, *Studies of Collective Effects in Atomic Strontium*. M.Sc. Thesis: Niels Bohr Institute, University of Copenhagen 2015
- [27] R.Martin, *Towards Continuous Cavity-Enhanced Nonlinear Spectroscopy in Strontium*. M.Sc. Thesis: Niels Bohr Institute, University of Copenhagen 2013.
- [28] M.R. Henriksen, *Cavity Enhanced Spectroscopy on Ultra Cold Atoms*, M.Sc. Thesis: Niels Bohr Institute, University of Copenhagen 2014.
- [29] HUANG, X. YUNG, Y. LING (2003): *A Common Misunderstanding about the Voigt Line Profile*, Journal of the Atmospheric Sciences, Vol. 61, pp. 1630- 1632
- [30] ONLINE: <https://www.thorlabs.com/drawings/81c96f8b49bac4d3-108FB6C4-C8A4-BODA-C2707123D886837F/TH10K-SpecSheet.pdf>
- [31] ONLINE:<https://www.arduino.cc/en/Tutorial/PWM>
- [32] H.J. Metcalf and P. Van der Straten, *Laser Cooling and Trapping 1*. Springer, 1999.
- [33] X. Xu, T.H. Loftus, J.L. Hall, A. Gallagher, J. Ye, 'Cooling and trapping of atomic strontium', *Journal of the Optical Society of America B*, vol. 20, n0.5, p968,2003.
- [34] R. Paschotta, article on 'beam radius' in the Encyclopedia of Laser Physics and Technology, 1. edition October 2008, Wiley-VCH, ISBN 978-3-527-40828-3. ONLINE: https://www.rp-photonics.com/beam_radius.html.
- [35] Stable 32 Manual ONLINE: <http://www.stable32.com/Manual154.pdf>.
- [36] R. Drozdowski, M. Ignaciuk, J. Kwela, and J. Heldt, 'Radiative lifetimes of the lowest $3P1$ metastable states of Ca and Sr', *Zeitschrift fur Physik D Atoms, Molecules and Clusters*, vol. 41, no. 2, pp.125-131, Jul. 1997.
- [37] M.J. Martin, D. Meiser, J.W. Thomsen, Jun Ye and M.J. Holland, *Extreme nonlinear response of ultranarrow optical transitions in cavity QED for laser stabilization*, PHYSICAL REVIEW A84, 063813 (2011).
- [38] P. Clausing, *The Flow of Highly Rarefied Gases through Tubes of Arbitrary Length*, Journal of Vacuum Science and Technology 8, 636 (1971) doi: 10.1116/1.1316379, ONLINE <https://doi.org/10.1116/1.1316379>